ΕΛΛΗΝΙΚΗ ΔΗΜΟΚΡΑΤΙΑ

ΠΑΝΕΠΙΣΤΗΜΙΟ ΙΩΑΝΝΙΝΩΝ

ΠΟΛΥΤΕΧΝΙΚΗ ΣΧΟΛΗ

ΤΜΗΜΑ ΜΗΧΑΝΙΚΩΝ ΕΠΙΣΤΗΜΗΣ ΥΛΙΚΩΝ

ΜΕΤΑΠΤΥΧΙΑΚΟ ΠΡΟΓΡΑΜΜΑ

«ΠΡΟΗΓΜΕΝΑ ΥΛΙΚΑ»

ΥΠΟΛΟΓΙΣΤΙΚΗ ΜΕΛΕΤΗ ΜΙΚΡΟΡΡΟΪΚΩΝ ΔΙΑΤΑΞΕΩΝ ΚΑΙ ΜΗΧΑΝΙΚΩΝ ΒΙΟΑΙΣΘΗΤΗΡΩΝ

ΜΕΤΑΠΤΥΧΙΑΚΗ ΕΡΓΑΣΙΑ

ΙΑΚΩΒΟΣ ΓΑΒΑΛΑΣ

ΙΩΑΝΝΙΝΑ 2018

HELLENIC REPUBLIC

UNIVERSITY OF IOANNINA

POLYTECHNICAL SCHOOL

DEPARTMENT OF MATERIALS SCIENCE AND ENGINEERING

MASTER PROGRAM

«ADVANCED MATERIALS»

COMPUTATIONAL STUDY OF MICROFLUIDICS AND MECHANICAL BIOSENSORS (SUSPENDED MICROCANTILEVERS)

MASTER THESIS

IAKOVOS GAVALAS

IOANNINA 2018

Η παρούσα Μεταπτυχιακή Διατριβή εκπονήθηκε στο πλαίσιο των σπουδών μου για την απόκτηση του Μεταπτυχιακού Διπλώματος Ειδίκευσης στην εξειδίκευση:

Βιοϋλικά και Βιοϊατρική Τεχνολογία

που απονέμει το Τμήμα Μηχανικών Επιστήμης Υλικών του Πανεπιστημίου Ιωαννίνων.

Εγκρίθηκε την ……..από την εξεταστική επιτροπή:

1. Δημήτριος Ι. Φωτιάδης, Καθηγητής του ΤΜΕΥ της Πολυτεχνικής Σχολής του Παν/μίου Ιωαννίνων, **Επιβλέπων**

2. Συμεών Αγαθόπουλος, Αναπληρωτής Καθηγητής του ΤΜΕΥ της Πολυτεχνικής Σχολής του Παν/μίου Ιωαννίνων

3. Λεωνίδας Γεργίδης, Επίκουρος Καθηγητής του ΤΜΕΥ της Πολυτεχνικής Σχολής του Παν/μίου Ιωαννίνων

ΥΠΕΥΘΥΝΗ ΔΗΛΩΣΗ

"Δηλώνω υπεύθυνα ότι η παρούσα διατριβή εκπονήθηκε κάτω από τους διεθνείς ηθικούς και ακαδημαϊκούς κανόνες δεοντολογίας και προστασίας της πνευματικής ιδιοκτησίας. Σύμφωνα με τους κανόνες αυτούς, δεν έχω προβεί σε ιδιοποίηση ξένου επιστημονικού έργου και έχω πλήρως αναφέρει τις πηγές που χρησιμοποίησα στην εργασία αυτή."

***«Τὰ πάντα ῥεῖ* καὶ οὐδὲν μένει»**

Ἡράκλειτος ὁ Ἐφέσιος 544 ~ 484 π.Χ

ACKNOWLEDGMENTS

I would like to thank my supervisor Prof. D.I. Fotiadis for the opportunity he gave me to work in his team and collaborate with so many excellent scientists. Without his guidance and support it would not be possible to conduct this thesis. I appreciate a lot his trust in me and his consideration for my concerns during the completion of my master thesis. His help was encouraging through this challenging year.

I also want to thank all of my fellow labmates in the MEDLAB, IMBB, FORTH, for their help, support and guidance during my MasterThesis. I place on record, my sincere thanks to Dr. Nikolaos Tachos, Dr Antonios Sakellarios and Dr. Evanthia Tripoliti for sharing their time and knowledge in their scientific fields. Their support and guidance was valuable to me.

I would also want to thanks the rest of the MEDLAB colleagues for their support and inspiring ideas "*Dimitris Pleouras, Dr. Panagiotis Siogkas, Ioannis Pappas, Vaso Kigka, Ioannis Andrikos and Georgia Karanasiou"*

Last but not least, I would like to thank my family for trusting me and supporting my dreams, giving me the opportunity to pursue my passion for science.

ΠΕΡΙΛΗΨΗ

Η παρούσα εργασία, εστιάζεται στην υπολογιστική μελέτη μικρορροϊκών διατάξεων και μηχανικών βιοαισθητήρων με την Μέθοδο των Πεπερασμένων Στοιχείων. Σκοπός, είναι η ενσωμάτωσή τους σε συσκευές Lab-on-a-Chip (LoC) και Point-of-Care (PoC) που θα μετράνε το δυναμικό ιξώδες Νευτωνικών και Μη-Νευτωνικών υγρών. Ο συγκεκριμένος τύπος βιοαισθητήρων παρουσιάζει πολλά υποσχόμενα αποτελέσματα και ποικίλες εφαρμογές στον χώρο των βιοαισθητήρων.

Η εργασία χωρίζεται σε 8 Κεφάλαια. Στο Πρώτο Κεφάλαιο, γίνεται μια σύντομη εισαγωγή της εργασίας, εισάγοντας τους σημαντικότερους και χρησιμότερους ορισμούς. Στο Δεύτερο Κεφάλαιο, αναλύονται οι σημαντικότεροι τύποι βιοαισθητήρων καθώς και ο τρόπος λειτουργίας τους. Στο Τρίτο Κεφάλαιο, θα αναλυθεί μια ειδική κατηγορία των μηχανικών βιοαισθητήρων αυτή των ροηφόρων μηχανικών μικρο-βιοαισθητήρων (suspended microcantilevers). Το Τέταρτο Κεφάλαιο, εστιάζει στην έως τώρα εξέλιξη αυτών των βιοαισθητήρων καθώς και στην θεωρητική μοντελοποίησή τους με την Μέθοδο των Πεπερασμένων Στοιχείων. Στο Πέμπτο Κεφάλαιο, εισάγοται οι διαφορετικές γεωμετρίες του μηχανικού βιοαισθητήρα προς μελέτη, οι απαραίτητες υποθέσεις, οι εξισώσεις και οι συνοριακές συνθήκες που εξυπηρετούν την επίλυση του προβλήματος. Το Κεφάλαιο Έξι, εστιάζει στην αριθμητική επιλύση του προβλήματος με την Μέθοδο των Πεπερασμένων Στοιχείων εξετάζοναταις την συμπεριφορά των βιοαισθητήρων. Το Έβδομο Κεφάλαιο, φιλοξενεί τα αποτέλεσματα της εργασίας όπως αυτά καθορίζονται από την φύση του προβλήματος. Τέλος, στο Όγδοο Κεφάλαιο, παρατίθενται τα συμπεράσματα των αριθμητικών μοντελοποιήσεων.

Τα αποτελέσματα των προσομοιώσεων συγκλίνουν προς έναν εξαιρετικά ευαίσθητο βιοαισθητήρα και αντιπαραβάλλονται με αυτών της βιβλιογραφίας. Ακόμη, αντικείμενο μελέτης των επιδόσεων του προτεινόμενου βιοαισθητήρα, αποτέλεσαν δείγματα από Νευτωνικά και μη- Νευτωνικά ρευστά. Τα αποτελέσματα που εξήχθησαν υποδηλώνουν εναν εξεραιτικά ευαίσθητο και μεγάλης ακρίβειας βιοαισθητήρα. Τέλος, εξ' αιτίας του μικρού μεγέθους της εν λόγω διάταξης καθίσταται δυνατή η εφαρμογή της σε LoC και PoC συσκευές.

ABSTRACT

In this work, a computational study of microfluidics and mechanical biosensors (suspended microcantilevers) is employed using the Finite Elements Method. The aim of this work is to fabricate a Lab-on-a-Chip (LoC) and a Point-of-Care (PoC) device to measure the dynamic viscosity of the Newtonian and Non-Newtonian fluids. This type of biosensors has shown extremely promising results and applications in the field of the biosensors.

The current thesis is divided into 8 Chapters. In Chapter 1, a brief introduction to microfluidics is presented. The most important and useful for this work definitions are introduced. In Chapter 2, the origin, the types and the functionality of the biosensors are presented. In Chapter 3, a specific type of mechanical biosensors, the suspended microcantilever, is analyzed. In Chapter 4, the evolution in the field of the suspended microcantilevers, as well as the Finite Elements Method (FEM) simulation of them, is introduced. In Chapter 5, the different mechanical biosensors' geometries that are used, the hypothesis, the equations and the boundary conditions of the problem are introduced. Chapter 6, is dedicated to the numerical solution of the current problem by employing FEM. In Chapter 7, the results of our experiments are presented. Finally, Chapter 8, summarizes the conclusions of the current work.

The results of the simulations predict a highly sensitive biosensor comparing to previous published works. The proposed microcantilever was tested using Newtonian and Non-Newtonian fluids showing promising results. Finally, its small size is crucial for its integration into LoC and PoC devices.

Contents

CHAPTER 1. INTRODUCTION 1

CHAPTER 2. BIOSENSORS 3

2. Biosensors 3

2.1 Basic Concepts 3

2.2 Applications 7

2.3 Biosensors' Materials 12

2.4 There is Plenty of Room at the Bottom 16

2.4.1 Microfabrication Methods 16

2.4.2 Photolithography 16

2.4.3 Microcontact Printing 17

2.4.4 Micromachining 18

2.4.5 Non- Linear Lithography 22

2.4.6 Laser Ablation 23

CHAPTER 3. MICROCANTILEVERS AND SUSPENDED MICROCANTILEVERS . 24

3.1 Microcantilevers 24

3.1.1 Sensing Methods 26

3.1.2 Describing the tip's deflection 27

3.2 Suspended Microcantilevers 34

CHAPTER 4. STATE-OF-THE-ART FEM MODELING OF MICROCANTILEVERS 38

CHAPTER 5. BIOSENSOR'S MODELING 42

5.1 Introduction 42

5.2 Materials and Methods 43

5.3 Assumptions and Boundary Conditions 46

5.4 Microfluidics and Biosensor Geometries and Meshing 48

5.4.1 Geometries 48

5.4.2 Meshing....49
5.4.3 Meshing Quality....53
CHAPTER 6. FINITE ELEMENTS METHOD....58
6.1 Finite Elements Method....58
6.1.2 History....58
6.1.3 Basic Concept....58
6.1.4 Finite Element Analysis....59
6.1.5 Fluid Structure Interaction....61
6.2 Fluid flow....62
6.2.1 Governing equations of fluid flow....62
6.2.2 Arbitrary Lagrangian- Eulerian....65
CHAPTER 7. NUMERICAL SOLUTION....68
7.1 Simulations and Results....68
CHAPTER 8. DISCUSSION, RESULTS & FUTURE WORK....93
References....96

Nomenclature	***S.I Units***
Symbols	Name
F	*Output signal*
C	*Analytes Concentration*
s	*Biosensor's Sensitivity*
ρ	*Material's Density*
Γ	*Cross-Section of the beam*
$\hat{E}$	*Young's Modulus*
I_z	*Moment of Inertia*
ω	*Frequency*
n	*Modal Number*
t	*Time*
L	*Length of the Microcantilever*
w	*Width of the Microcantilever*
h	*Thickness of the Microcantilever*
k_{eff}	*Effective Spring Constant*
m_{eff}	*Effective Mass*
S	*Cantilever's Sensitivity*
$\Delta\omega_o$	*Change on Resonant Frequency*
Q	*Quality Factor (Q-factor)*
E	*Energy*
χ	*Position*
R	*Curvature Radius*
$\boldsymbol{\sigma}$	*Stress*
ν	*Poisson's Ratio*

Nomenclature	***S.I Units***
Symbols	Name
δ	*Cantilever's Deflection*
A	*Microchannel's Area*
f	*Resonant Frequency*
$\boldsymbol{\varepsilon}$	*Strain*
B	*Displacement Differentiation Matrix*
$\boldsymbol{u}$	*Nodal Displacement Vector*
N	*Shape Functions*
$\boldsymbol{U}$	*Displacement Vector at a Point Inside a Finite Element*
$\vec{u}$	*Fluid's Velocity Vector*
P	*Pressure*
μ	*Dynamic Viscosity*
f_{ext}	*External Forces*
$\boldsymbol{K}$	*Stiffness Matrix*
$\boldsymbol{F}$	*External Loads Matrix*
$D\{*\}$	*Material Derivative*
$\boldsymbol{\tau_{ij}}$	*Viscous Stress*
δ_{ij}	*Kronecker Delta Symbol*
$\vec{V}$	*Velocity Field*
g	*Earth's Gravity*
$\dot{\gamma}$	*Shear Rate*
M_v	*Mass Matrix of the Fluid Domain*
M_u	*Mass Matrix of the Solid Domain*

Nomenclature	***S.I Units***
Symbols	Name
K_v	*Tangent Coefficient Matrix of the Fluid Domain*
K_u	*Tangent Coefficient Matrix of the Solid Domain*
$\widehat{M_v}$	*Linearized Mass Matrix*
$\widehat{K_v}$	*Linearized Coefficient Matrix*
$\overline{R_v}$	*Vectors of Discretized External Applied Forces on the Fluid Domain*
$\overline{R_u}$	*Vectors of Discretized External Applied Forces on the Solid Domain*
$\overline{u^F}$	*Vectors of the Internal Fluid Particle Displacements*
H_c	*Hematocrit*

CHAPTER 1. INTRODUCTION

In this work, the type of the biosensor which is studied is the suspended microcantilever. This biosensor is a microstructure of a microfluidic channel inside a microcantilever biosensor (Figure I). This type of biosensors have attracted the interest of the scientific and engineering community since they are very sensitive, they produce minimum background electrical noise [1] and they can be integrated into small Lab-on-a-Chip (LoC) devices. Several studies have been conducted to examine the suspended microcantilevers. In 2007 Burg, Thomas P., et al. [2] using a suspended microcantilever resonator managed to weigh biomolecules, single cells and single nanoparticles by recording the frequency shifts from the cantilever's initial resonant frequency. One of the most common sensing methods for microcantilevers is the optical. It is simple and it can be easily used at any type of microcantilevers. However, it is not versatile and is not suitable for LoC solutions. To overcome this problem, other methods have been introduced. In 2011 Boisen et al. the capacitive methods in a nanocantilever for read-out is referred [3]. In 2013 Faegh et al. proposed a piezoelectric cantilever to solve the sensing issue. The sensor could sense and actuate at the same time [4, 5]. In the same year, this idea was improved and new materials were introduced using polymers instead of silicon [6]. In 2015 W.M Zhang et al. investigated experimentally the Fluid Structure Interaction (FSI) between the microfluidic channel and an oscillated microcantilever beam. They have also added flowing particles [7]. In 2017 a suspended microcantilever with an orthogonal flow to the bending plate of the structure, was fabricated in order to measure the kinematic viscosity of Newtonian (water – salt) and non-Newtonian (milk – fat) fluids with different concentrations [8]. In the same year a simulation study of a suspended microchannel resonator nano-sensor was conducted [9]. The Finite Element Method (FEM) was initially introduced for microcantilever biosensors in 2006 [10]. In 2018 Packirisamy et al. used two parallel, perpendicular to microcantilever deflection direction, microfluidic channels made from polydimethylsiloxane (PDMS), to investigate the 2D and the 3D behavior of the suspended polymeric microfluidics using FSI employing FEM [11].

In this work, a suspended microcantilever biosensor is simulated for the determination of the fluid's dynamic viscosity. Starting with the Computational Fluid Dynamics (CFD) simulations, the Reynolds Number, R_e, the entrance length, l_e (when the fluid flows inside the bigger channels), the velocity, the pressure drop, the wall shear stress will be calculated for each fluid case and the velocity profile in YZ and YX planes will be determined. After the CFD simulations, the generated loads from each fluid flow case were transferred to the Mechanical Analysis in order to perform the FSI. One and two way FSI simulations were compared. Two biosensor geometries were tested in order to examine which biosensor type would give the maximum tip deflection. Both biosensor geometries were tested as if they were fabricated with PDMS. After the geometry evaluation, polymethyl methacrylate (PMMA) was tested as an alternative material. Moreover, three different lengths for the microcantilever were simulated to test their maximum deflection. Moving forward, the tip's maximum deflection and the von Mises equivalent stress were calculated. A correlation between the fluids' velocity, the fluids' dynamic viscosity and the maximum deflection of the microcantilever's tip were performed. Last but not least, the FSI results were used to predict the maximum tip deflection for a fluid. The current work is a complete study of the behavior of a suspended microcantilever biosensor.

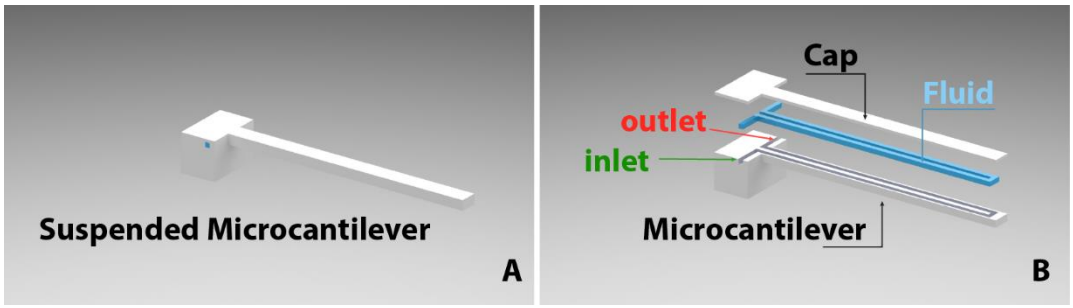

Figure I. Schematic representation of a suspended microcantilever biosensor. A) The biosensor assembly and B) the biosensor's components. Details in (Chapter 5).

CHAPTER 2. BIOSENSORS

2. Biosensors

The biosensors are devices that are used to detect, analyze and monitor biological or chemical materials with physiochemical detectors [12]. The term biosensor was first introduced in the scientific literature in the late 1970s [13]. The first biosensor was created by Clark in 1956. He presented a novel electrochemical sensor by adding "enzyme transducers as membrane enclosed sandwiches". In his paper, the entrapping of the enzyme glycose oxidase in a dialysis membrane over an oxygen probe was described. The aim of his work was to continuously monitor the oxygen tension of venous and arterial blood circulating in heart - lung machines [14].

2.1 Basic Concepts

A biosensor is a device that can convert physical, mechanical and chemical inputs to electrical signals for measurement and analysis. The electrical signal might be analog or digital and in most of the cases the measurement is indirect, meaning that manipulation of the data is required in order to extract meaningful information.

A biosensor consists of the biological recognition elements, the bioreceptors, the electrical interfaces and the electronic systems. The biological elements are biological or chemical fluids. The bioreceptors are the materials derived for the biological recognition elements or biomimetic components. Enzymes, antibodies, cells, bacteria, DNA, RNA, etc. can be considered as bioreceptors. The electrical interfaces are the detector elements based on different technologies that can detect, analyze and monitoring the bioreceptors. Such interfaces are the electrochemical or pH electrodes, thermistors, Photodetectors, Piezoelectric parts etc. The electronic systems are the amplifiers, the signal processors and the display devices (Figure 2.1).

To properly operate, a biosensor must be in close proximity to the signal transduction element. The biosensitive element is usually bound to the transducer by one of the four following mechanisms.

Membrane Entrapment: Semipermeable membrane traps the bioreceptors against the sensor's surface.

Physical Adsorption: Bioreceptors are bound to sensor surface by combination of Van der Walls forces, hydrophobic forces, hydrogen bonds and ionic forces.

Matrix Entrapment: Porous encapsulation matrix traps the bioreceptors against sensor surface.

Covalent Bonding: Sensor surface contains reactive groups for covalent binding of bioreceptors [15].

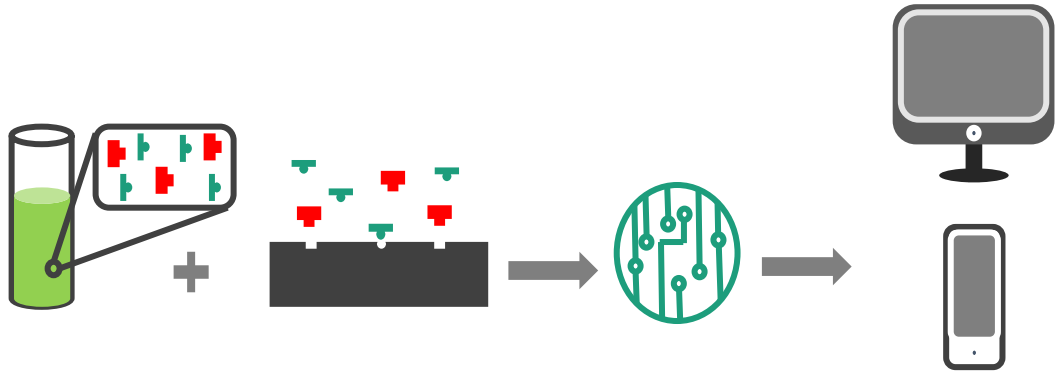

Figure 2.1 Schematic representation of a biosensor.

There are a lot of different types of biosensors available on the market and they can be distinguished from each other by their operating characteristics. The key operating characteristics of a biosensor are the selectivity, sensitivity, reproducibility, stability and linearity [16]. However, these are not the only key characteristics that a biosensor has. In Table 2.1 the important sensor performance characteristics are listed.

Selectivity, refers to the ability of the specific analysis of a sample inside a chemical or biochemical solution. The antigen-antibody interaction is the most convenient example of this. Immobised antibodies on the surface of the transducer, acting as bioreceptors, are exposed to a biochemical solution and specifically bind with the containing antigens and not with other molecules.

Sensitivity, is the ability of the biosensor to detect the possible minimum amount of an analyte. A biosensor is usually designed in such way to detect low

concentrations in the order of ng/ml or even fg/ml to confirm the presence of traces of analytes in a sample.

Reproducibility, refers to the ability of the generation of identical results for a duplicated experimental set-up. The reproducibility of a biosensor can be usually compromised by the precision and the accuracy of the transducer and the electronic compounds. The biosensor's ability to provide identical responses every time a sample is measured, is called precision. Furthermore, the ability of a biosensor to provide a mean value in close proximity to the true value, every time a sample is measured, is known as accuracy.

Stability, is the biosensor's ability to remain unaffected to ambient disturbances either from inside or outside the biosensing system. These disturbances can lead to false output signals, they compromise the biosensor's measurements and affect the precision and the accuracy of the device. Thus, stability is a vital issue in the biosensor designing process.

Linearity, indicates the measurement's accuracy comparing to a straight line, described as

$$F = s \cdot C, \tag{2.1}$$

where, C is the analytes' concentration, F is the output signal, and s is the sensitivity of the biosensor. Linearity can be related to the resolution of the biosensor. One can define the biosensor's resolution as the smallest required change in the analyte's concentration to induce a change in the output signal of the biosensor.

A convenient way to understand and compare the differences among the biosensor is by applying a classification scheme based on the sensed phenomena and detection mode (Table 2.1). The biosensors bellow are analyzed in **Paragraph 2.2**. Only the mechanical biosensors will be left to be analyzed in detail in **Chapter 3**. However, the functionality of the biosensor can be limited by taking into account the fabrication cost, the final size of the device and its availability. A comparison between the ideal and (in most cases) real characteristics of the biosensors, can provide a better understanding of what properties, a good biosensor has to fulfill (Table 2.2) [15].

Table 2.1 Sensors Classifications [15].

Biosensor Types	How they function
Acoustic	Wave amplitude, phase, polarization, spectrum, velocity etc.
Biological	Concentration, State, etc.
Chemical	Humidity, pH, Concentration, State, etc.
Electrical	Charge, Current, Voltage, Electric Field, resistance, conductance, dielectric permittivity, capacitance, inductance, etc.
Magnetic	Magnetic Field, Flux, Magnetic moment, Magnetization, Magnetic Permeability, etc.
Mechanical	Piezoelectricity, Position, Displacement, Velocity, Acceleration, Force, Torque, Moment, Stress, Pressure, Strain, Mass, Density, Flow, Shape, Texture, Stiffness, Compliance, Viscosity, Structure, etc.
Optical	Amplitude/Intensity, Phase, Polarization, Spectrum, etc.
Thermal	Temperature, Heat, Flux, Entropy, Specific Heat, etc.

Table 2.2 A comparison between the Desirable and Undesirable biosensor's features [15].

Desirable Features	Undesirable Features
Linear and noise-free response	Nonlinear response with undesirable random noise signals
Zero baseline offset	Unwanted baseline offset because of the systematic error in output.
No baseline drift	Baseline drift where there is output variation over time.
Zero response Time	Long response time for the output signal to reach a steady-state value.
Infinite frequency bandwidth for instantaneous response	Often appeared limited or even narrow frequency bandwidth for best response.

2.2 Applications

Acoustic Biosensors

An acoustic biosensor uses mechanical or acoustic waves as a detection mechanism. The acoustic waves can propagate inside a solid material by deforming the crystal structure and force the atoms to oscillate around their equilibrium position. The most common acoustic waves are the *surface acoustic waves (SAWs), bulk waves* and the *surface generated bulk waves* [17]. Such biosensors can detect changes in mass, elasticity, conductivity and dielectric properties from mechanical or electrical variations. A SAWs based biosensor is composed of electronics and it is integrated into a sample flow carrying the analyte. Using interdigital transducers on the surface of a piezoelectric crystal, these devices can generate and detect the surface acoustic waves [18]. The biological recognition elements (antibodies), are immobilized on the surface of the piezoelectric crystal to capture the floating bioreceptors (antigens). These molecules are interfering with the SAWs and influence their velocity and as a result the output generated signal (Figure 2.2).

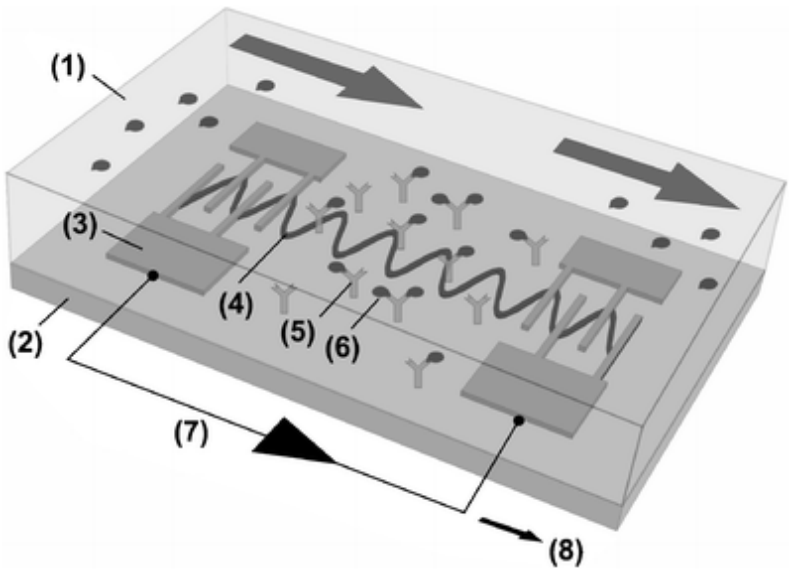

Figure 2.2 A surface wave acoustic biosensor. 1) The medium in which the biosensor is immersed. (2) The piezoelectric crystal. (3) Interdigital transducers. (4) Surface waves. (5) Immobilized biological recognition elements. (6) Bioreceptors. (7) Driving electronics. (8) Output signal [19].

Magnetic Biosensors

The magnetic biosensors transform the magnetic moment of the magnetic particles into an electric signal and then into a concentration value. A magnetic biosensor can detect the biomolecules using radioisotopes, enzymes, fluorescent or charged molecules. The magnetic particles can easily penetrate the porous media without interference with optical probes producing negligible optical and magnetic background noise signal. This type of biosensor is characterized by high sensitivity since the magnetic particles do not interfere with the biological solution. Furthermore are chemically stable and are not affected by chemical reagents. Figure 2.3 shows a magnetic biosensor. A typical magnetic biosensor is fabricated on the surface of a chip. Each magnetic field sensor is covered with a specific recognition element. The sample covers the sensing area and the recognition elements are binding with the specific receptors. Then, specifically modified microbeads are inserted into the solution and are binding with the specific receptors [20].

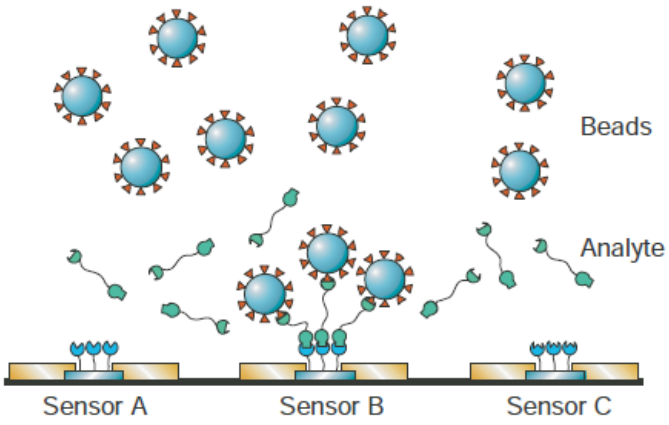

Figure 2.3 A typical scheme of a magnetic biosensor [20].

Optical Biosensors

One of the oldest types of biosensors are the optical biosensors which manipulate the electromagnetic irradiation to detect and analyze chemical and biochemical samples. The optical biosensors function very well in aqueous solutions and the detection is performed in a nondestructive manner. Furthermore, they are extremely sensitive and surface specific meaning that they only respond to absorbed

species at or close to the transducer surface such as the interference from the bulk solution is minimized [20]. A typical optical biosensor utilizing surface plasmons is shown in (Figure 2.4). On the surface of a microchannel, a slide with a thin film of gold is placed and above this, a prism is mounded. A polarized light passes through the prism and the slide hitting on the surface of the gold film. As a result, a plasmonic surface wave is generated. The reflected light is then collected by a detector. The reflectivity changes, versus the incident's light angle, or the wavelength, provides a signal that is proportional to the volume of the biopolymer bound on the surface [21].

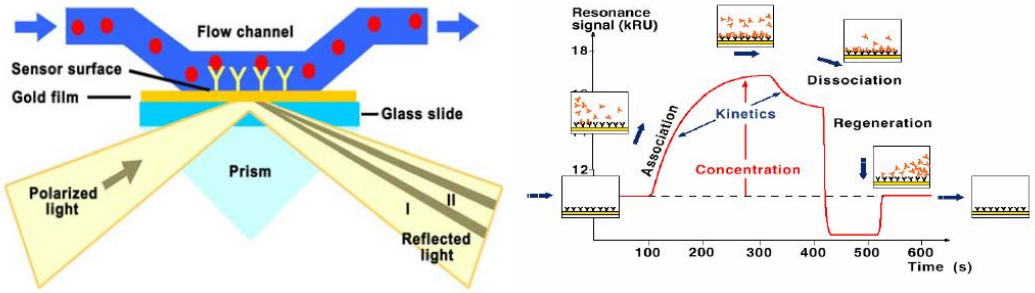

Figure 2.4 Surface Plasmon optical biosensor [21].

Thermal Biosensors

The thermal energy used by this class of sensors comes almost invariably from the Joule effect when a current flows through a resistive element. A thermal Biosensor detects the elements in question measuring the enthalpy changes. The produced thermal signal is proportional to the concentration of the substrate [20]. A typical optical biosensor utilizing surface plasmons is shown in (Figure 2.5). A single microchannel column is serially partitioned into several discrete detection regions. Each region has one enzyme preparation corresponding to the specific analyte and pair of film thermistors. One of them is placed after and one before the enzyme matrix. On injection of substrate mixture, multiple thermal signals generated since exothermal reactions occur. Each reaction emits a characteristic thermal signal [20].

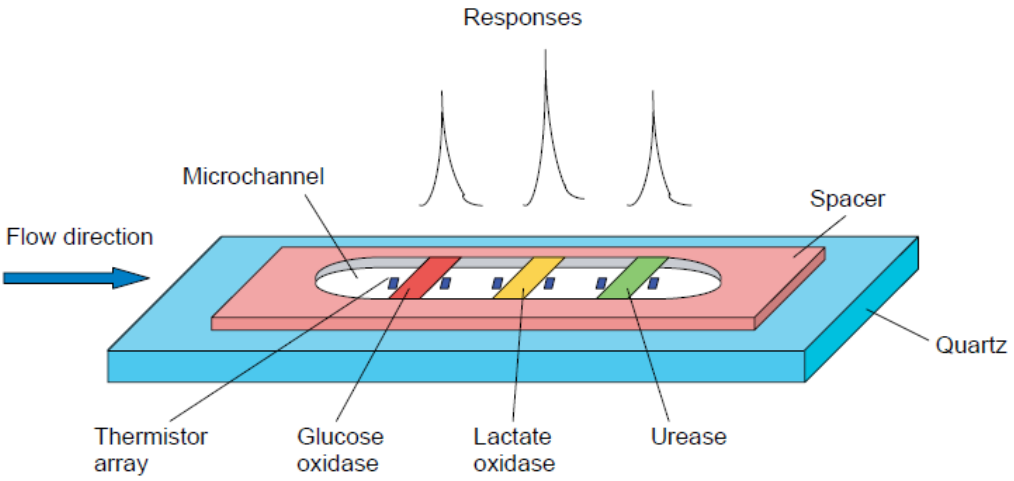

Figure 2.5 A typical thermal biosensor [20].

Electrochemical Biosensors

Such biosensors use electrochemical techniques such as amperometry, coulometry, potentiometry, etc. to determine the concentration of the sample. Amperometric biosensors use the oxidation and the reduction of certain electroactive chemical species at constant applied potential. A coulometric biosensors functions by the amount of charge which passes between two electrodes. This is directly analogous to the oxidation or reduction of the electroactive species at the electrode. Potentiometric biosensors measure the difference in electrical potential between two electrodes. This kind of biosensor is the most common and the most frequently cited in the literature. A biosensor with three electrode configuration for the detection and measurement of IL-10 (HF biomarker) based on Cyclic Voltammetry and Electrochemical Impendence Spectroscopy is shown in (Figure 2.6) [22].

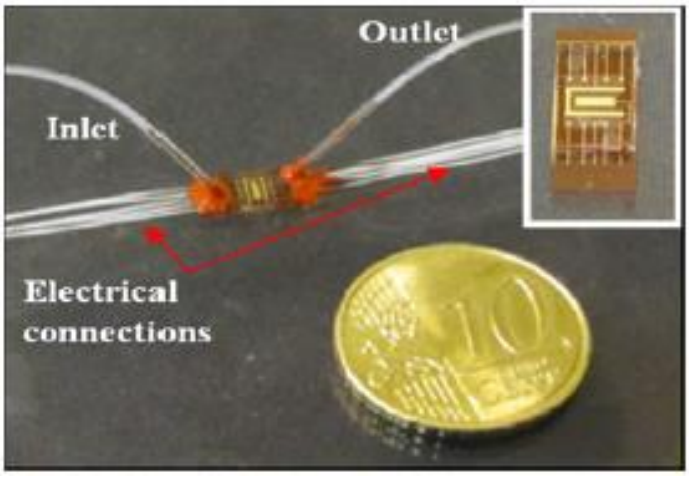

Figure 2.6 An electrochemical biosensor [21].

Chemical Biosensors

Chemical biosensors are one of the most common biosensors on the market, combining different sensing technologies to detect, analyze and measure the desired chemical or biochemical samples. Chemical biosensors are often combined with microfluidics devices in order to lead the sample in the sensing area. Sensing may occur with different ways such as using a fluorescent immunoassay [23], chemoluminescence [24] or electrochemical techniques such as amperometry, coulometry, potentiometry (as mentioned above). They can also detect the variation of the pH using electrodes [25] (Figure 2.7).

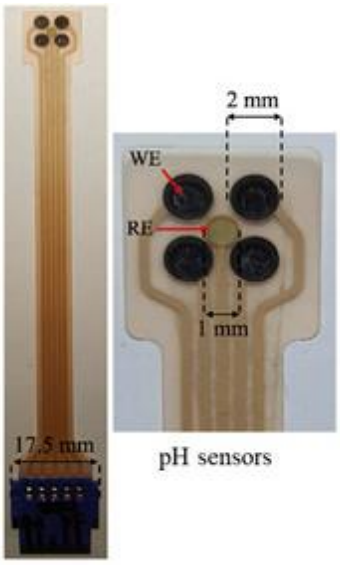

Figure 2.7 A pH screen-printed sensor of real time wound monitoring [25]

2.3 Biosensors' Materials

The majority of materials used in the field of microelectromechanical systems (MEMS) originated form the semiconductor industry. The electrical properties are the number one priority for integrated electrical circuits. The fabrication of MEMS take place on a flat substrate called the "wafer". The wafer is a thin slice of a bigger single crystal ingot and its thickness ranges between 300 and 700 μm. The selection of MEMS materials requires the knowledge of their mechanical, optical, electrical, chemical and or biological (for bioMEMS) properties [15].

Silicon

Silicon is the most used material in MEMS fabrication and it is also the second most abundant material on earth. It is not found a pure form and thus, it needs to be purified before microfabrication process. Silicon always found in nature as *silica* (SiO_2) or *silicates* ($Si + O +$ other elements). The purification process of silicon starts by the separation of the silicon from the other compounds. The clean form of the silicon called *metallurgical grade silicon.* Then, using the chlorination process, liquid form of trichlorosilane ($SiHCl_3$) is formed. Trichlorosilane is then separated from the impurities. By chemical reduction in the presence of hydrogen, the liquid turned into solid. Finally, the silicon takes its purified form after the "Czochralski" method [26].

Thin Films

Apart from solid silicon, thin films are also very popular in MEMS microfabrication. It is very common in MEMS industry, to use silicon as the primary substrate for other materials to be deposited on its surface forming a thin layer of films. The thin films have usually different properties form the bulk forms. In contrast to the bulk material, a thin film has smaller grain size, lower density due to porosity, are not crystalline but they can either take an amorphous or a polycrystalline form. Forming a polycrystalline form, the thin films can take a preferred orientation or a fiber texture. Analyzing the adhesion, the stress and the resistivity properties of the thin films, one can notice their importance in MEMS industry [15].

One of the most important properties of the thin films is the adhesion. Good adhesion is a necessity in a clean room environment to prevent contamination. There are some cases in which it is necessary the usage of an intermediate layer to strengthen the adhesion.

Thin films are always under a constant stress which is either tensile or compressive. The tensile stress leads the film to shrink, causing a concave bending, while the compressive tends to expand it causing a convex bending.

Due to the high amount of grain boundaries and defects, the thin film metals are always more resistive than the bulk materials [26].

Polymers

Aside from Silicon, polymeric materials are also very popular in MEMS industry. Polymers are commonly used in bioMEMS since many of them are categorized as biomaterials. They can be used as substrates, coatings, structural or sacrificial layers. Polymers have a relative low cost production, they increase the fracture strength and the have lower Young's module compared to silicon and other MEMS materials. A large amount of polymers are biological friendly, biodegradable and nontoxic, make them the best candidates for biological applications. Some of the most common polymeric materials used in MEMS are the Polydimethylsiloxane (PDMS), Polyimide, SU-8, Parylene and Polymethylmethacrylate (PMMA) [15].

PDMS is known as *silicon rubber* and it has been widely used as a rapid prototyping material for inexpensive microfabricated devices. PDMS is the most popular *silicon-based organic polymer.* Its chemical structure is presented in (Figure 2.8). PDMS exhibits low glass transition temperature, high elasticity, low stiffness and has high resistance to oxidation. Furthermore, it is optically transparent, non-toxic and non-flammable [15].

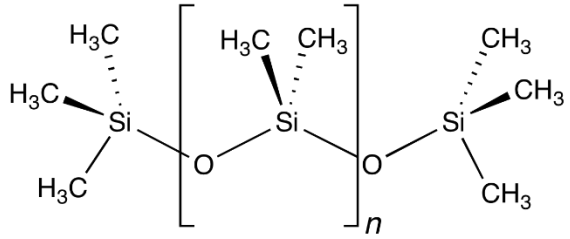

Figure 2.8 PDMS chemical structure.

Polyimides are on market since 1955. Their use is on high temperature fuel cells, displays and in aerospace/ aeronautical industry. A well-known polyimide is Kapton firstly produced by DuPont in 1960s. The general form of polyimides is presented in (Figure 2.9). Polyimides were firstly introduced to MEMS industry as flexible substrates used for sensors and multielectrodes [15]. They can be characterized as highly thermal and chemical stable, they have high glass transition temperature, they are mechanically strong, they do not absorb a lot of moisture and they are solvent resistant. Furthermore, their inertness, low cytotoxicity and biocompatibility make them a strong candidate for biomedical applications.

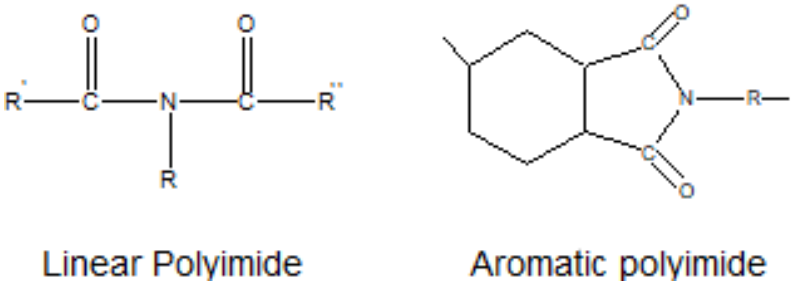

Figure 2.9 General structure of polyamides

SU-8 is another widely used polymer synthesized by IBM in 1989. Was firstly designed for the microelectronics industry as a photoresist to provide higher resolution negative masks for semiconductors microfabrication. Its popularity will be increased in the late 1990s as an alternative to the expensive X-ray lithography method. SU-8 is versatile enough and its properties can altered through the mixing with other materials to the prepolymer liquid [15].

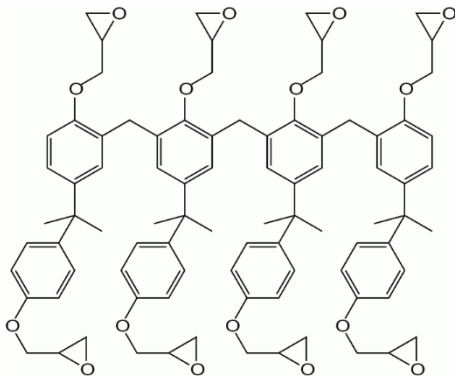

Figure 2.10 SU-8 formula

Parylene was used in microelectronics as well as in medical industries a long time before it used in MEMS area. Parylene N and C were primarily used as protective coating for stents, cardiac assist devices, catheters, etc. These type of parylenes have been categorized in Class VI from the USP (United States Pharmacopeia) achieving the highest biocompatibility level for a polymer (https://vsiparylene.com/parylene-biocompatibility/). Parylene used in MEMS, is deposited as a thin film on the surface of a substrate using CVD process (chemical vapor deposition).

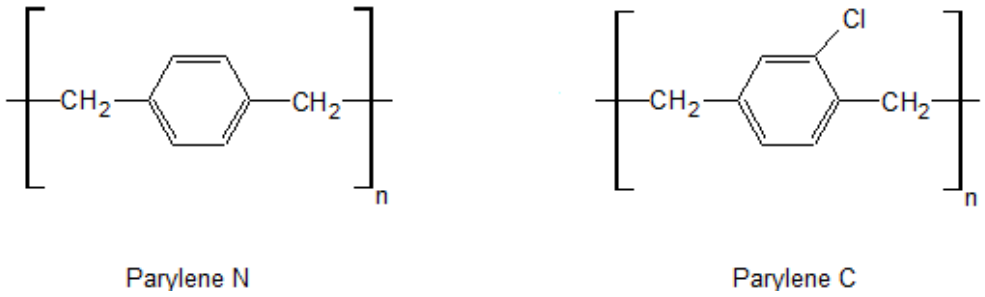

Parylene N Parylene C

Figure 2.11 Parylene structures

Biomaterials

Biomaterials are materials used in medical devices, implants, extracorporeal devices and in disposable systems. As the National Institutes of Health (NIH) determines them " Any substance (other than drug) or combination of substances, synthetic or natural in origin, which can be used for any period of time, as a whole or as a part of a system which treats, augments or replaces any tissue, organ, or function of the body" [27]. Biomaterials are widely applicable in bioMEMS and must be fulfill certain criteria such as biocompatibility, cytotoxicity and sterilization. Common biomaterials are metallic, ceramic and polymeric. Apart from their nature, all biomaterials used in bioMEMS are typically thin films or substrates having different properties of their bulk analogous.

For a biosensor and in general for a medical device, FDA approval (Food and Drug Administration, USA) or CE marking (Conformité Européenne) must be gained.

2.4 There is Plenty of Room at the Bottom

Scientists and Engineers are now able to design and fabricate microelectronics, microfluidics and microelectromechanical systems (MEMS) that were impossible until 1960s when the microfabrication based on silicon, spread from Texas and California to the rest of the world. The potential advantages of smaller machines were recognized years before their existence. In 1959, **Richard Feynman** in one of the most famous lectures in science's history, recognized the benefits of micro and nanotechnology. The lecture passed in history with the title "**There is Plenty of Room at the Bottom"**.

2.4.1 Microfabrication Methods

There are a lot of microfabrication methods for a microfluidic or for a MEMS (or bioMEMS) device. In this chapter, only a part of them will be analyzed and will be divided into two groups. The first group consists of the **Photolithography**, **Micro Contact Printing** and **Micromachining** while in the second group **Non-Linear Lithography** and **Laser Ablation** are presented.

MEMS and microfluidics devices usually undergo the same procedure. They start as a concept that later on is designed in a computer aided design software (CAD), a simulation is performed for behavior prediction and then is fabricated for experimental results and validation.

2.4.2 Photolithography

Photolithography is a process used in microfabrication to pattern geometries on the surface of the substrates. Using a CAD program, a 2D pattern is designed and is printed into a photomask. The photomask is usually made of transparent fused silica and is covered with chrome (as an ink) in specific areas. It contains clear and opaque areas. The photomask is later used to transfer the pattern onto a substrate while is exposed to an electromagnetic radiation. Once the pattern has been transferred, several chemical processes are taking place in order to produce the final result (Figure 3.1) [28].

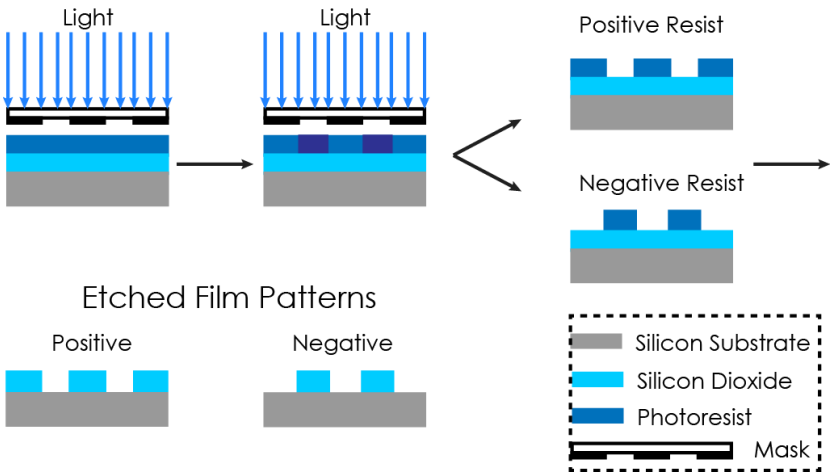

Figure 3.1 Photolithography process. Positive and Negative resist. The substrate is exposed to the UV light, then is developed and etched.

2.4.3 Microcontact Printing

In microcontact printing, an elastomeric pattern, used as a stamp, transfers an "inked" material onto the surface of a substrate. Usually the elastomeric stamp is the PDMS (polydimethylsiloxane) that transfers the "inked" material to form the self-assembled monolayers (SAMs) on the substrate [29]. The method was first addressed for printing organic molecules onto the surface of a substrate [30]. It is also a popular technique for transferring patterns of biological materials [31]. The two most common microcontact printing methods are the **Lift-off** (Figure 3.2) and **Casting** (Figure 3.3)

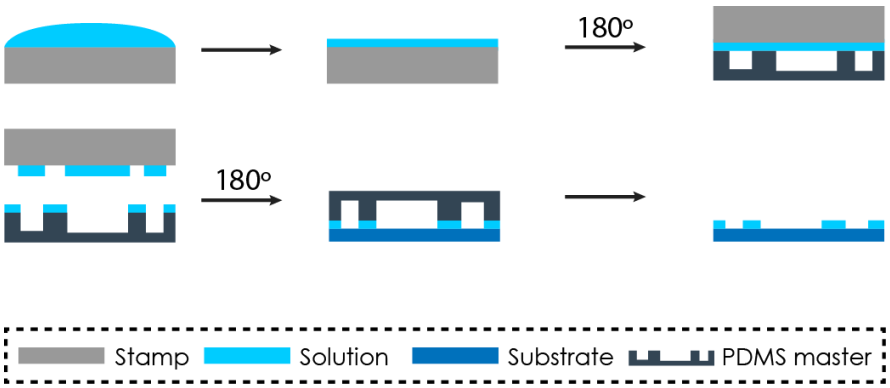

Figure 3.2 Lift-off technique. The sample (solution) covers the surface of the stamp and then, a PDMS master, is placed on it. After that the PDMS master transfers the sample onto a substrate and the final pattern is produced.

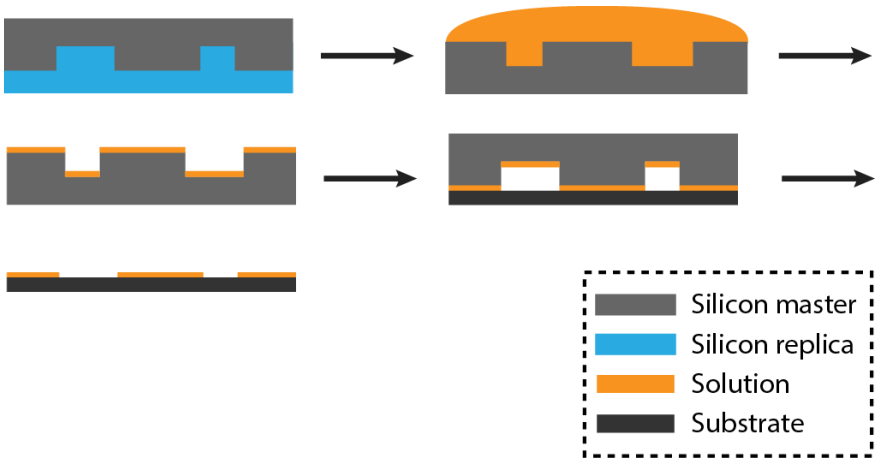

Figure 3.3 Casting method. A silicon replica is used to produce a silicon master. The silicon master is then covered with a solution (even biological). Dries and then is transferred on the surface of a substrate to form the final pattern.

2.4.4 Micromachining

There are a lot of micromachining methods for MEMS (or bioMEMS) fabrication with the main techniques to be the **Surface** and the **Bulk** micromachining. These methods are widely used to produce 2D (or 2.5D) parts that can move, rotate, deflect or even vibrate [32]. Furthermore, to fabricate a 3D structure, newer methods have been introduced with **LIGA** (Lithograhie (Lithography), Galvanoformung (electroforming) and Abformung (molding)) being the most important one.

2.4.4.1 Surface Micromachining

Surface micromachining is a fabrication method that relies on the selective deposition of thin layers to form complex structures on the top of a substrate. The deposited layers are called *structural layers* while the layers that temporarily hold the structure and then they are removed, are called *sacrificial layers* [33]. This method is widely used in CMOS (Complementary Metal Oxide Semiconductor) technology and produces parts that can move and rotate [32]. This requires a small gap among components in order the parts to move freely (Figure 3.4). To fabricate a MEMS device following the surface micromachining method, several steps need to take place. A sacrificial layer is deposited onto the surface of a substrate, then a photoresist material is patterned on the top of it using a photomask and a light source (typically UV light). The photoresist covers the sacrificial layer in specific regions. After that, a chemical

etching process is followed to remove the photoresist and the uncovered sacrificial layer. Then, the preferable material is transferred onto the surface. A new photoresist is deposited onto the preferable material and a second chemical etching takes place. The uncovered photoresist areas are removed and a final chemical etching subtracts the sacrificial layer leaving only the preferable material on the top of the substrate (Figure 3.5) [33]

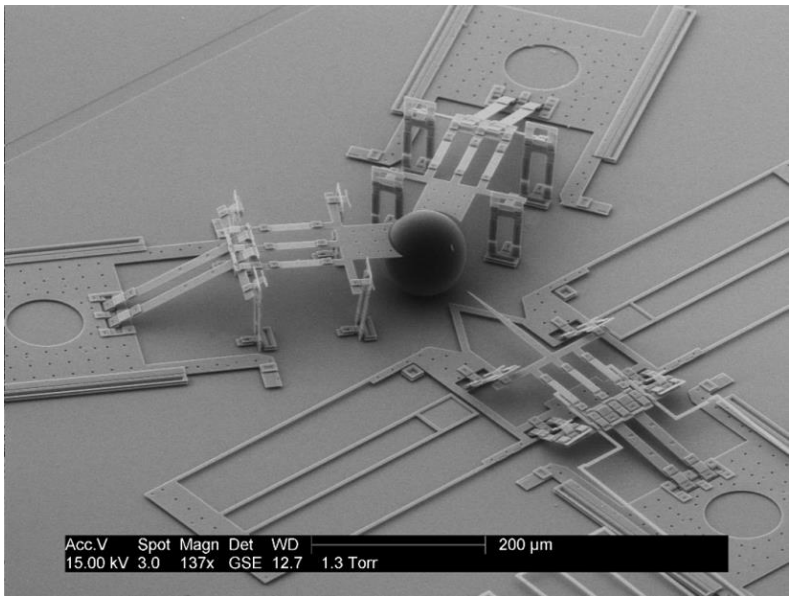

Figure 3.4 SEM image of a self – reconfiguring metamorphic nanoinjector for injection into mouse zygotes *[Aten, Q. T., Jensen, B. D., Burnett, S. H., & Howell, L. L. (2014). A self-reconfiguring metamorphic nanoinjector for injection into mouse zygotes. Review of Scientific Instruments, 85(5), 055005]*.

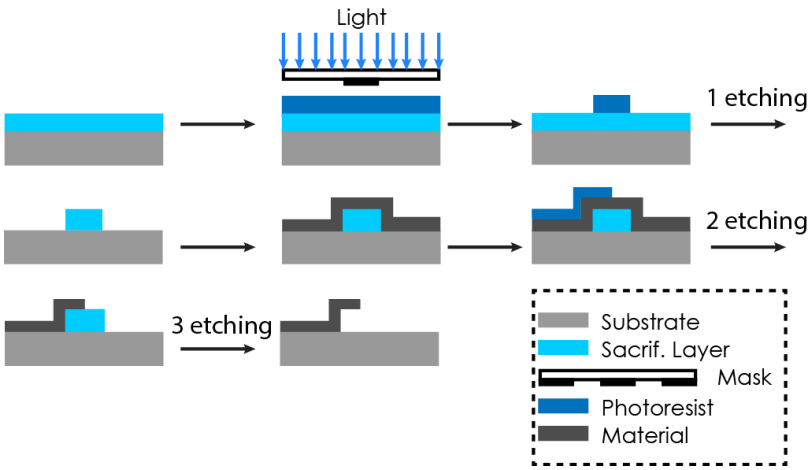

Figure 3.5 Surface micromachining method.

2.4.4.2 Bulk Micromachining

Unlike surface micromachining, bulk micromachining is a subtractive method. Using either dry or wet etching techniques of chemical or physical processes, a bulk material is "sculpted" to form the final MEMS device. There two major bulk micromachining etching techniques, ***isotropic*** and ***anisotropic*** (Figure 3.6).

Isotropic

The isotropic etching technique uses acidic solutions to create cavities from the surface to the bulk of the material. By agitating or not the sample while it is etched, two different profiles can be fabricated. Agitation leads to an ideal isotropic etching

Anisotropic

The anisotropic tends to be slower method than the isotropic due to the high temperatures needed. This technique is orientation specific meaning that some planes are removed faster than others. In a silicon wafer, the denser plane is the [111] while the [100] is the less dense and so is etched faster.

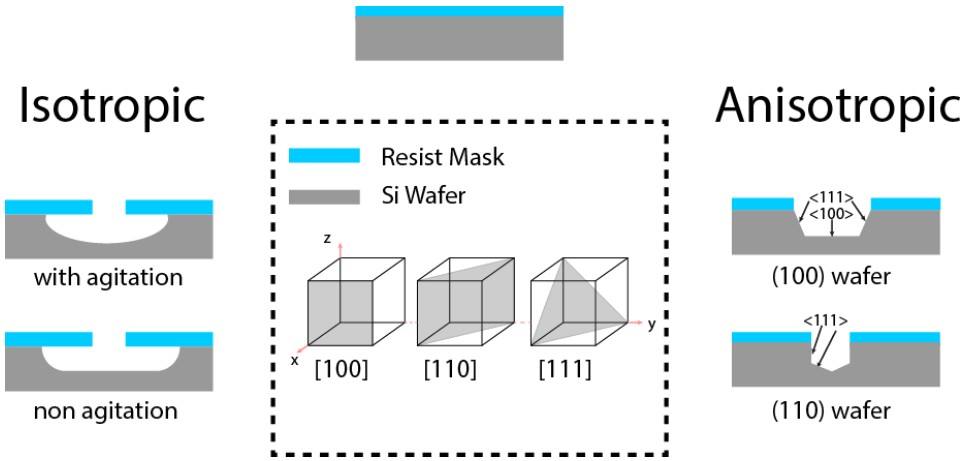

Figure 3.6 Isotropic and Anisotropic process.

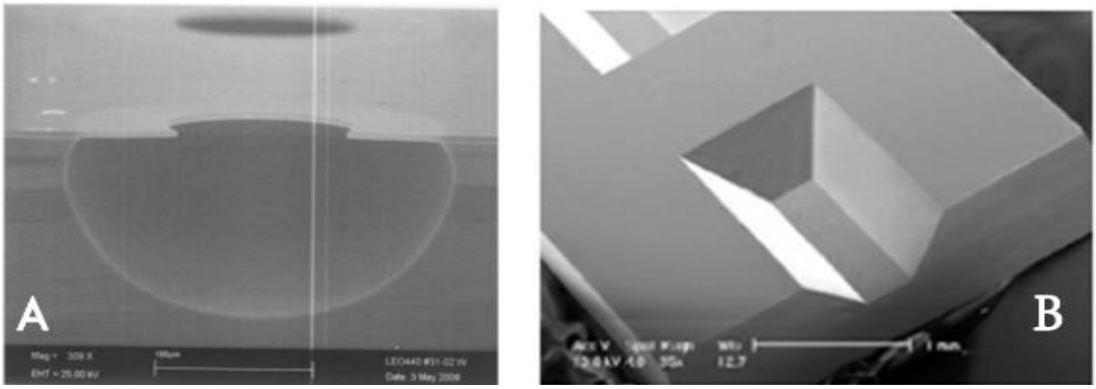

Figure 3.7 SEM image of A) isotropic etching (*https://www.oxford instruments.com/products/etching-deposition-and-growth/processes/etching-processes/silicon/si-(isotropic)-etch*) and B) of bulk etching (*https://www.memsnet.org/about/fabrication.html*)

2.4.4.3 LIGA

The LIGA technique was first introduced to create higher aspect ratios microstructures. While its first use was to fabricate a microfluidic nozzle for uranium enrichment, now it is a method for high aspect ratio 3D complex microstructures. Furthermore while the other techniques are Silicon based technologies and UV is used, LIGA uses polymers such as PMMA (polymethylmethacrylate) as molds, gold or beryllium for mask materials and X-rays as light source. X-rays cannot penetrate the gold while the beryllium is transparent in these wavelengths. Thus, gold and beryllium masks are used depending on the desired outcome. However UV and UV-sensitive polymers such as SU-8 can be used, although this combination lucks of resolution and precision. LIGA process is divided into parts (Figure 3.8). It starts using an X-ray sensitive mask with the desired pattern printed on it and an X-ray source. The patterns is transferred through the mask onto PMMA. The X-rays can easily penetrate into the PMMA and thus, geometries with high depth can be produced. After that, the PMMA undergoes chemical development and a polymeric mold is produced. The PMMA mold is placed into an electroplating bath for metal deposition. Finally, the PMMA is chemically removed and the metallic replica stands alone.

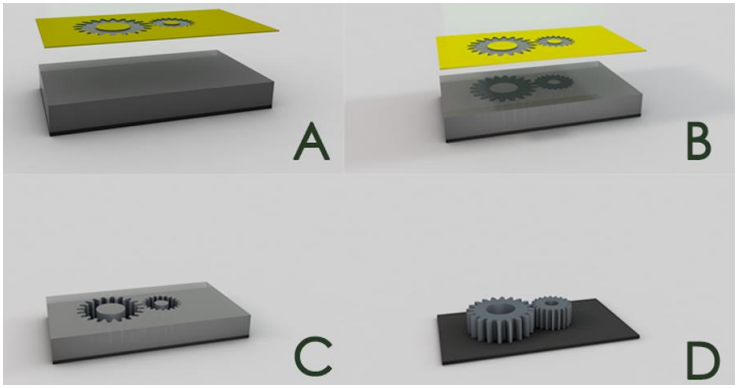

Figure 3.8 Schematic process of LIGA technique. A) The X-ray sensitive mask is placed on the top of the PMMA. B) The pattern is then transferred onto the surface. C) The PMMA mold is produced and D) The mold fills with metal and the PMMA mold is chemically removed leaving only the metallic geometry on the substrate surface.

2.4.5 Non- Linear Lithography

Non-Linear Lithography, as its name indicates, is a non-linear technique uses the two-photon polymerization for complex 3D microfabrication inside the volume of a photosensitive sol-gel material. The method uses the free radical polymerization process and a femtosecond laser at 800nm (IR) wavelength, with 200fs pulse length and 50-80 MHz repetition rate. The unique characteristic of this method is that the laser beam can be tightly focused inside a small volume of a sol-gel material, known as voxel, and only this small volume becomes solid through the polymerization. Then, continuing the polymerization layer by layer a complex geometry is attached on the glass's surface (Figure 3.9) [34].

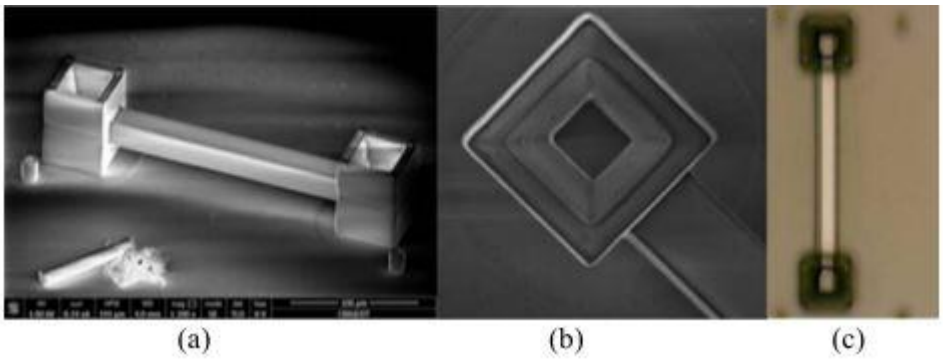

Figure 3.9 (a) SEM image of 3D cantilever biosensor with two fixed ends. (b) Detailed view of the (a) image and (c) a top view optical microscopy image of the sensor [34].

2.4.6 Laser Ablation

A laser beam of a fs laser can induce strong absorption in even transparent materials, due to the non-linear multiphoton absorption. With multiphoton absorption, the surface and bulk modification of a transparent material, such as glass or polymers is possible. The laser beam interacts with the mater at the scale of a duration of the scale of fs and transfers high energy in a tiny, well focused spot. The material absorbs this energy and then is ablated from the surface. Producing a cavity. For microfluidics fabrication, fs laser ablation offers the ability to either fabricate microchannels on the surface of a glass or in the bulk of it, makes this process a promising technique [35].

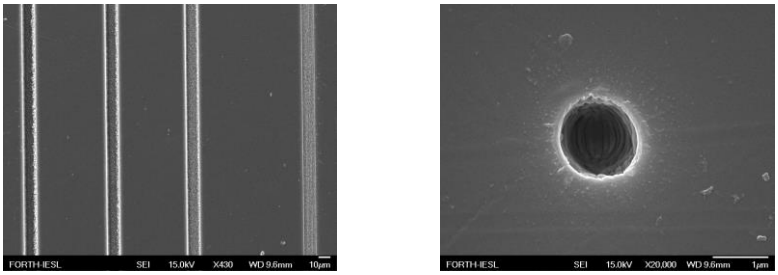

Figure 3.10 SEM images from Laser Ablation Micromachining. From left to right. Straight lines and a laser beam spot on the surface of a Polycarbonate substrate [35].

CHAPTER 3. MICROCANTILEVERS AND SUSPENDED MICROCANTILEVERS

3.1 Microcantilevers

The advances in the field of the biosensors, made the determination of quantities and phenomena that were impossible to be detected with other techniques, possible. The unique property of the biosensors to operate in different ways, makes them the perfect research tool to obtain data in micro and nano scale, such as changes in temperature, mass and surface stress [3].

After the invention of the Atomic Force Microscope (AFM) in 1986, the microcantilevers became available as sensing tool of the material's surface. The AFM working principle is simple and is based on the old phonograph. AFM provides images for the roughness of a material by scanning its surface with a probe. The micrometer dimensions of the probe allow the relative high resonant frequency (in the order of KHz) and provide a low spring constant (about $N \cdot m^{-1}$). These characteristics make the probe less sensitive to external vibrations and improves its sensitivity. Since the dimensions of the probe are in the scale of μm, microfabrication techniques are necessary. Mimicking this technology, in 1990, two groups from the Stanford University [36] and IMB [37] fabricated the first micromachined cantilevers with integrated tips.

This type of biosensors have attracted the interest of the scientific and engineering community since they are very sensitive, label free, portable, cheap and they can be integrated into small Lab-on-a-Chip (LoC) or Point-of-Care (PoC) devices [3]. The most common sensing method for the microcantilevers is the optical. A laser beam is used to measure the cantilevers deflection in the same manner as it is used in the Atomic Force Microscopy. A laser beam hits the surface of the microcantilever's tip and reflects onto a position sensitive detector (PSD). The differences in the laser's beam position, in x-y coordinates, on the surface of the PSD, indicates the deflection,

in the z- axis, of the microcantilever's tip. It is simple and it can be easily used at any type of microcantilevers (Figure 3.1) [38, 39].

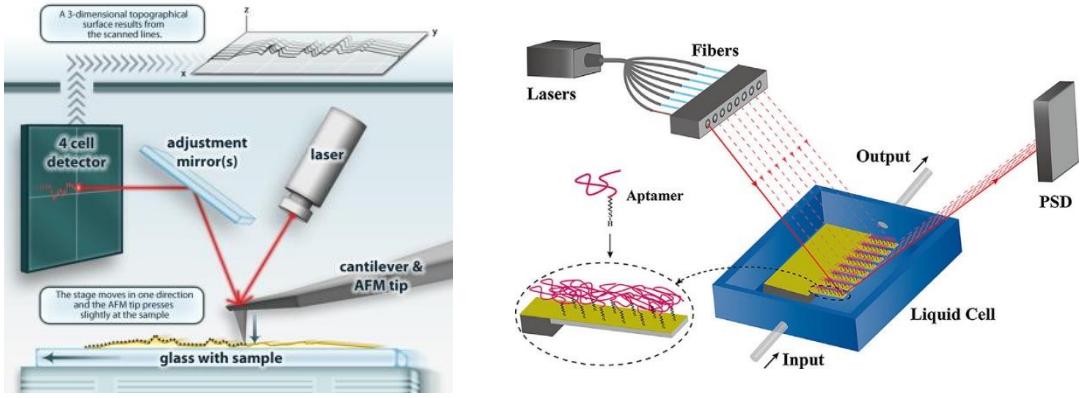

(A) **(B)**

Figure 3.1 (A) Functioning principal of an Atomic Force Microscopy [38] and (B) the optical detection method for measuring the beams' deflection of an array of microcantilevers [39].

In 1997 [40], microcantilever sensors were used for online surface change measurements. This research paper showed that it is possible the real time recording of the self-assembled monolayer (SAM) as well as the changes in the surface-stress due to the length of the alkane chain.

One year later, in 1998, a group of scientists and engineers at IBM, Zurich, developed an array of polymer coated silicon microcantilevers for real time detection of gas and vapor adsorption on the microcantilever's surface causing surface stress changes [41].

Using only one cantilever tip, in the first research experiments, it was extremely difficult to run measurements and at the same time control the reference cantilever. To overcome this problem, an array of microcantilevers started to be used (Figure 3.1B) [41]. In a set-up like this, one cantilever is left out for reference purposes while the rest of them are coated or treated in a specific way for sample determination. The advantage of using an array, instead of a single microcantilever sensor, is that it is possible to perform more accurate measurements. In our days, the majority of the research groups are using microarrays.

In 2000 [42], microcantilever biosensors, were used to detect a single-nucleotide polymorphism, paving the way for the potential diagnostic usage of the microcantilever biosensors.

In the same year, microcantilever biosensors with integrated parts started to appear indicating the need of more compact, versatile devices. Piezoresistive microcantilevers started to appear [43].

3.1.1 Sensing Methods

There are three basic sensing principles for the microcantilevers. In the first one, the microcantilever tip is bending downwards due to the added mass of the sample in questioning. This mode is also known as the static deflection mode (Figure 3.2A) [44]. In the second method, internal stress changes in the bulk of the microcantilever's material, lead the length of the tip to be expanded or contracted (Figure 3.2B) [45]. Finally in the third mode, the changes in the resonant frequency, due to the mass difference of the sample tested on the tip's surface, is recorded (Figure 3.2C) [46].

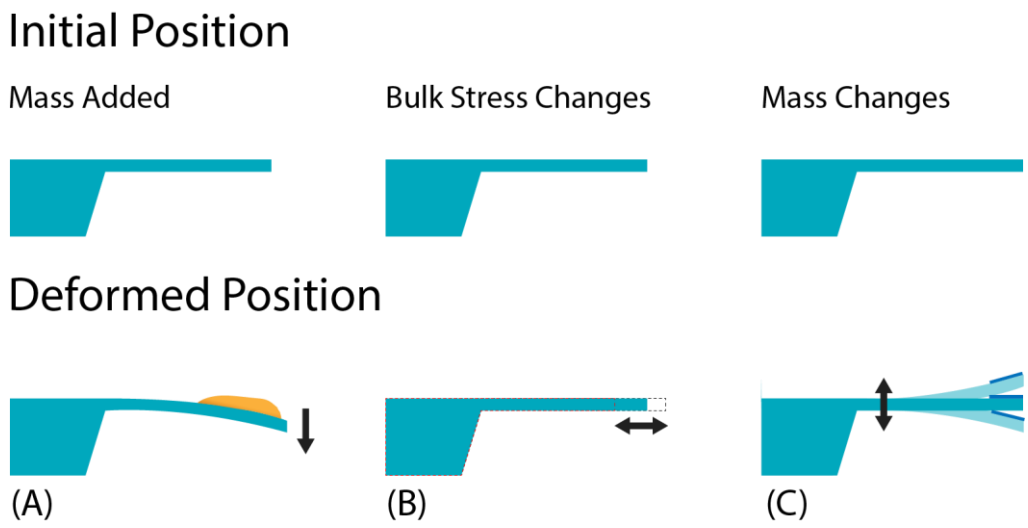

Figure 3.2 Schematic representation of the three basic sensing modes of a microcantilever. (A) The static deflection mode because of the added mass, (B) expansion and contraction of the tip's length caused by material's internal stress changes and (C) resonant frequency changes due to the mass changes

Using the abovementioned working modes, will be possible to fabricate highly sensitive sensors that can measure extremely tiny mass changes in the atto to zepto-gram range [46] or infinitesimal temperature variations in the scale of 10^{-5} K [45]. In 2006, the determination of a single small molecule was achieved by measuring a mass change in the range of 10^{-21} g [47, 48]. Such characteristics, make possible the use of the microcantilevers as mass-spectrometers with high sensitivity [3]. The sensitivity of the microcantilevers increases as their dimensions decrease. For better understanding of the microcantilever's working principle, for mass detection, it is necessary to describe mathematically the deflection of the microcantilever's tip. The damping as well as the Q-factor will be introduced.

3.1.2 Describing the tip's deflection

Assuming the case of a microcantilever biosensor as this illustrated in (Figure 3.3) and that the rotational inertia as well as the shear deformation, can be ignored in this particular example. If the material is linear elastic, and the added mass is evenly distributed on the surface, then the deflection of the cantilever can be expressed using the Euler-Bernoulli beam theory [49].

$$\frac{\partial^2 U(z,t)}{\partial t^2}\rho\Gamma + \frac{\partial^4 U(z,t)}{\partial z^4}\hat{E}I_z = 0, \tag{3.1}$$

where, $U(z,t)$ is the deflection in the x-axis, ρ is the density of the material, Γ is the cross-section of the microcantilever's beam, $\hat{E}$ is the Young's modulus and I_z is the moment of inertia.

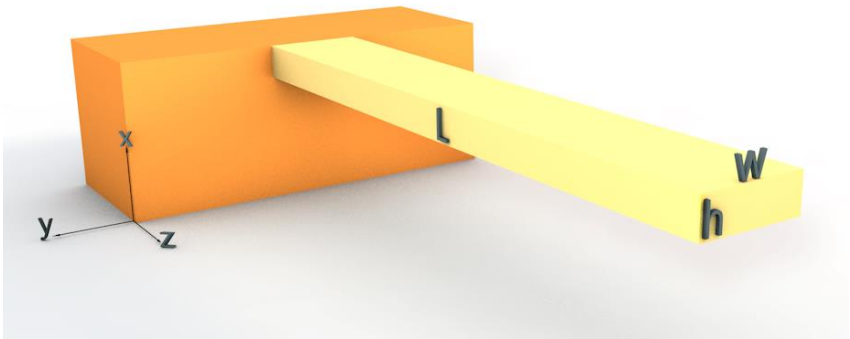

Figure 3.3 A microcantilever geometry. The dimensions are L: length, h: thickness and w: width

Solving the above differential equation eq. (3.1) [3], we ended up with a harmonic solution eq.(3.2) which is consisted by two parts, the position dependent and the time dependent term

$$U(z,t) = U_n(z)\exp(-i\omega_n t), \tag{3.2}$$

where, ω_n is the frequency and n is the modal number.

Inserting the eq. (3.2) into the eq. (3.1), two eigenfunctions come up eq. (3.3) which can be rewritten as in the form [50] eq. (3.4)

$$\frac{\partial^4 U(z,t)}{\partial z^4} = k^4 U(z,t), \quad k^4 = \frac{\omega^2 \rho \Gamma}{\hat{E} I_z}, \tag{3.3}$$

$$U_n(z) = A_n[cos(k_n z) - \cosh(k_n z)] + B_n[\sin(k_n z) - \sinh(k_n z)]. \tag{3.4}$$

Thus, for a microcantilever, the equation of the frequency is given by

$$1 + \cos(k_n L)\cosh(k_n L) = 0. \tag{3.5}$$

According to the values of $n = 1,2,3, n > 3$ the solutions are $\lambda_n = k_n L$=1.8751, 4.6941, 7.8548, $(2n-1)\pi/2$ respectively. As a consequence, the microcantilever beam is capable to vibrate in specific modes with a unique mode shape (Figure 3.4). The frequency in which every single mode shape is formed, is called eigenfrequency. For a rectangular beam cross section, the moment of inertia is given by $I_z = h^3 w/12$ and the formula of the eigenfrequency can be written as

$$\omega_n = \frac{\lambda_n^2}{L^2}\sqrt{\frac{\hat{E} L_z}{\rho \Gamma}} = \frac{\lambda_n^2}{2\sqrt{3}}\frac{h}{L^2}\sqrt{\frac{\hat{E}}{\rho}}. \tag{3.6}$$

In case that the ratio between the width and the height is $(w/h > 5)$, the Young's modulus is replaced by $\hat{E}/(1-v^2)$, where v, is the Poisson's ratio [51]. For simplicity, the model of the harmonic oscillator is usually used to describe the frequency of the microcantilever's beam instead of the individual resonance frequency [52]:

$$\omega_o = \sqrt{\frac{k_{eff}}{m_{eff}}}, \tag{3.7}$$

where, k_{eff}, is the effective spring constant and m_{eff}, is the effective mass. In the case of the first vibrating mode the effective mass as well as the effective constant reduce to:

$$m_{eff} = 0.24m_o, \quad m_o = \rho\Gamma L \quad and \quad k_{eff} = \frac{\hat{E}h^3 w}{4L^3}. \tag{3.8}$$

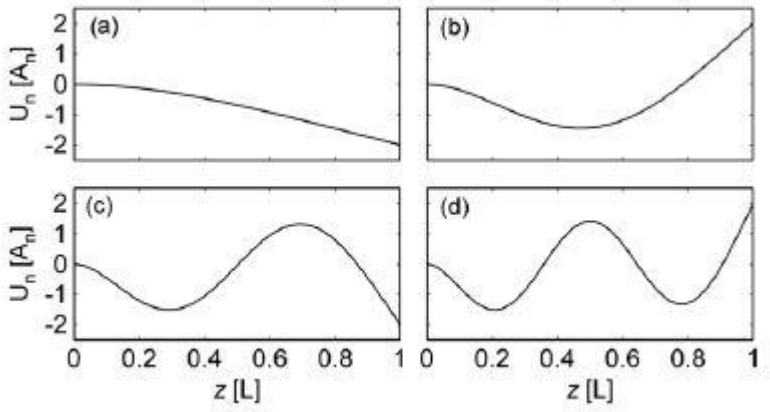

Figure 3.4 The first four vibrating shapes of a microcantilever as it seems from the side. The units of the amplitude is A_n while the length of the beam in in units of the length L. Where $L = 0$ refers to the base while where $L = 1$ refers to the very free edge of the beam [3].

Furthermore, one can observe that the resonant frequency is related with the vibrating mass, as it is depicted in the eq. (3.7). The frequencies changes due to the mass changes is called *Sensitivity.* The microcantilever's sensitivity shows the capability of the sensor to detect the minimum possible mass. The sensitivity can be expressed by differentiation of the eq. (3.7) with the respect to the mass:

$$S = \frac{\partial \omega_o}{\partial m_{eff}} = -\frac{\omega_o}{2m_{eff}} \approx \frac{\Delta\omega_o}{\Delta m}, \tag{3.9}$$

where, $\Delta\omega_o$ indicates the resonant frequency changes due to the added mass, Δm.

The inverse sensitivity multiplied by the minimum resonant frequency is the minimum detectable mass:

$$\Delta m_{min} = S^{-1}\Delta\omega_{min}\,. \tag{3.10}$$

For microcantilever biosensors, the frequency stability is essential. Although it could be compromised by the system's noise due to the electrical set-up or by other internal or external factors. The microcantilevers biosensor as well as every mechanical set-up, are experiencing kinetic energy loss. As it is known, the energy dissipation is defined as the energy lost per cycle to the stored energy. The inverse of the energy dissipation is called quality factor (Q-factor). The Q-factor is a dimensionless number indicating how fast or slow a resonator will die out. The higher the Q-factor is, the slower the resonator will stop to vibrate. The dissipation is the result of several internal (such as thermos-elastic damping) or external processes (such as interaction with the environment) and is expressed as:

$$\frac{1}{Q} = \sum \frac{1}{Q_{int}} + \sum \frac{1}{Q_{ext}}. \tag{3.11}$$

In contrast to the previous problem, if the added mass is not evenly distributed on the surface of the microcantilever's beam and is placed on a single point above it, then a new approach is needed since the abovementioned mathematical description doesn't work (Figure 3.5). The resonant frequency it is not only affected by the added mass but by the position on which it is placed also [53, 54, 55]. This is caused by the vibrational mode shapes.

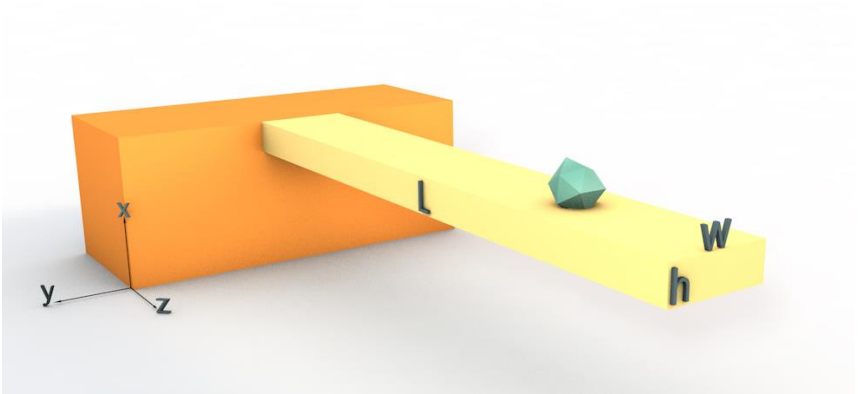

Figure 3.5 An added mass in a random position on the surface of the beam.

Figure 3.5 shows a microcantilever beam with mass m_o and a single particle with an added mass Δm, in a position $z_{particle}$ from the base. In case of $\Delta m \ll m_o$, the change on the resonant shape will be significantly low. Thus, the resonant frequency can be

approached using energy [3]. The particle will cause a small deflection on the microcantilever's beam and as a consequence the generated shear stress will be significantly low. Thus, the strain energy of a bended cantilever will be equal to the energy stored because of the induced strain:

$$E_{strain} = E_{kin} + E_{kin}^{particle}\,, \tag{3.12}$$

with

$$E_{kin} = \frac{1}{2} m_o \omega_{n,\ particle}^2\,, \tag{3.13}$$

and

$$E_{kin}^{particle} = \frac{1}{2} \Delta m \omega_{n,\ particle}^2 U^2\left(z_{particle}\right), \tag{3.14}$$

where, $\omega_{n,\ particle}$ is the frequency with the added mass of the particle and n, is the modal number. Since the generated shear stress is neglected, the change in the mode shape will be no significant. Thus, the strain energy of the cantilever will be assumed to be equal to the kinetic energy without the added particle:

$$E_{strain} \approx \frac{1}{2} m_o \omega_n^2\,. \tag{3.15}$$

By equalizing the kinetic energy and the strain energy, the eq. (3.12) gives the eigenfrequency of the beam with the particle on it.

$$\omega_{n,\ particle}^2 = \omega_n^2 \left(1 + \frac{\Delta m}{m_o} U_n^2\left(z_{particle}\right)\right)^{-1}. \tag{3.16}$$

As before, the sensitivity of the microcantilever is given by eq. (3.9) converted by the new added mass of the particle in a given random position from the base, $z_{particle}$:

$$\begin{aligned} S_{position} &\approx \frac{\Delta \omega_n}{\Delta m} = \frac{\omega_{n,\ particle} - \omega_n}{\Delta m}, \\ S_{position} &\approx \frac{\omega_n}{\Delta m}\left(\sqrt{1 + U_n\left(z_{particle}\right)\frac{\Delta m}{m_o}}^{-1} - 1\right). \end{aligned} \tag{3.17}$$

In the specific case in which the particle lies at the very edge of the cantilever beam ($z_{particle} = L$), the sensitivity of the resonator is equal to that with an evenly distributed mass [55]. In any other case, the sensitivity needs to be calculated in every position and mode. If the sensitivity and the change in resonant frequency are known, then it is possible to determine the mass of the molecules or particles that are bonded on the surface of the beam, forming a thin homogenous layer:

$$\Delta m_{meassured} = S^{-1} \Delta \omega_{meassured} \,. \tag{3.18}$$

Using the Dohn et al [55] approach, the position of an adhered particle and its mass can be calculated. By minimizing the eq. (3.19) with respect to the position, the position of the particle can be found:

$$\chi^2 = \sum_{n=1}^{N} \left(\frac{\omega_{n,\ particle}}{\omega_n} - \frac{1}{\sqrt{1 + \frac{\Delta m}{m_o} U_n^2 (z_{particle})}} \right)^2 , \tag{3.19}$$

where, N, is the total number of measured modes. The above calculation can be extended to the case of multiple particles [56].

The particles or molecules do not only add mass on the surface of the microcantilever but also cause surface stress because of their interaction with the microcantilever's surface (Figure 3.6).

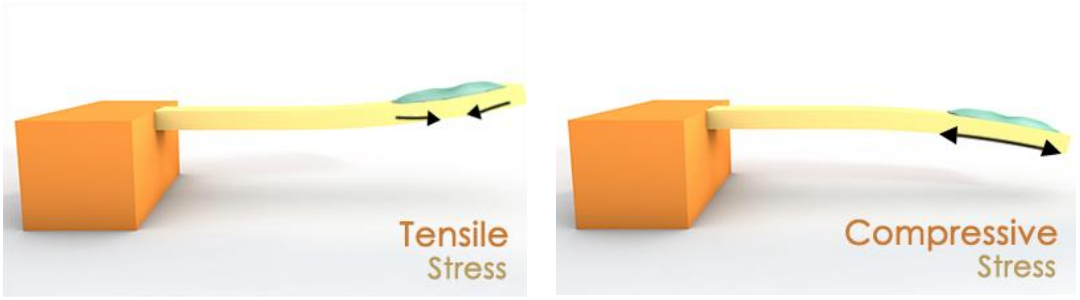

(A) (B)

Figure 3.6 Two ways of stress of a thin film of a material or biomolecules on the surface of the microcantilevers' beam. As the film shrinks, the beam bends upwards. Otherwise, when the film expands the beam bends downwards.

The interaction between thin film and material surface was tested by Stoney in 1909 [57]. Stoney studied the stress or elastic strain of a thin film which was deposited on the surface of a sheet of metal. However, the equation that describes this interaction can be expanded to even molecular or chemical thin films and to any material used for the microcantilever fabrication. The Stoney's equation gives the radius of the curvature of the cantilever's beam eq. (3.20):

$$R = \frac{\hat{E}h^2}{6\sigma(1-\nu)}, \tag{3.20}$$

where, R, is the radius of curvature, h, is the thickens of the sheet, σ, is the surface stress and ν, is the Poisson's ratio of the sheet. The Stoney's formula doesn't give the deflection of the cantilevers. This, changed in 1966 when the Jaccodine and Schliegel [58], used the Stoney's equation to make it applicable to cantilevers, eq. (3.21):

$$\delta = \frac{3(1-\nu)L^2}{\hat{E}h^2}\sigma\,. \tag{3.21}$$

From the eq. (3.21), it is clear that the beam bends more when the thickness decreases and the length increases. The above equation works very well when the material used for the microfabrication is simple. In case of a more complex or composite material, the eq. (3.21) can lead to a major error [59]. To overcome this issue FEM offers an excellent alternative. The FEM analysis will be discussed in **Chapter 4**.

There are few requirements the microcantilevers should have in order to function in the most effective way:

a) For better sensitivity, the microcantilever beam has to be as thin and long as possible.
b) A material with low internal damping and a microcantilever geometry with high Q-factor should be chosen.
c) Precise control for the geometry of the entire microcantilever array reduces the error of the measurements.
d) For microcantilevers with optical sensing method, the surface of the beam has to be coated with highly reflected material.
e) The microcantilever should not have initial bending.

3.2 Suspended Microcantilevers

The above mentioned mechanical biosensor is inside of a micro-container in which the solution in questioning is placed (Figure 3.1B). In this way, large volumes of solutions are used, the external noise due to the presence of the liquid is significant while damping and viscous drag compromise the measurements [60]. To overcome this issue, in 2003, Burg, T. P., & Manalis, S. R., proposed a new microcantilever geometry that combines the microchannel with the microcantilever biosensor. They introduced the *Suspended microchannel Resonator (SMR)* or *Suspended Microcantilever Resonator* (both names have been used in the bibliography) (Figure 3.7). A SMR is microcantilever set-up that has its upper surface been engraved and forming a cavity that it is sealed. The cavity forms a microfluidics channel inside of which the solution under study flows. This set-up ensures the use of very small liquid volumes, prevents unwanted damping and viscous drag and minimizes the external noise [60].

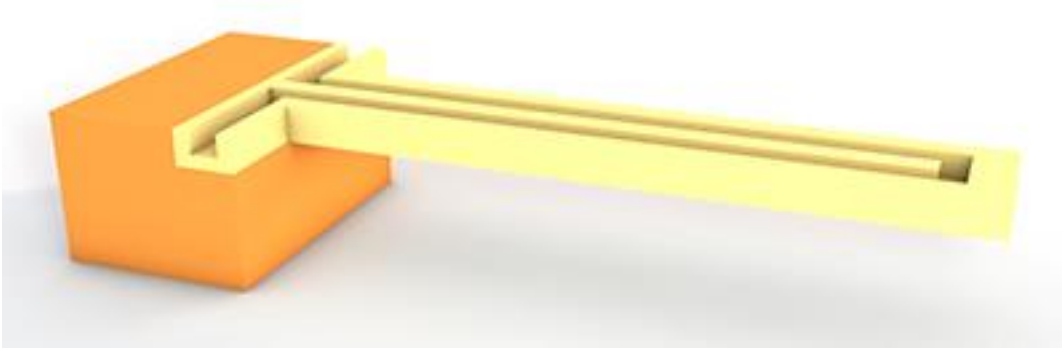

(A)

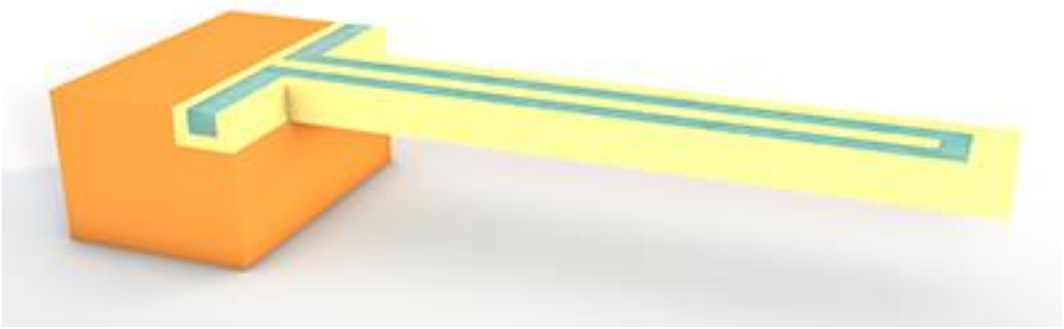

(B)

(C)

Figure 3.7 A SMR biosensor. (A) the forming cavity on the surface of the SMR, (B) filling the cavity with the liquid under study and (C) The actual SMR assembly.

In 2003, Burg, T. P., & Manalis, S. R., demonstrated the capability for biomolecular determination using a SMR devise. They used real-time measurements of the intramolecular binding between avidin and biotinylated bovine serum albumin. The devise they fabricated was actuated electrostatically while the measurement of the deflection was performed using the optical cantilever method. They achieved a surface mass resolution of 10^{-19} g/μm^2 which corresponds approximately to one protein pre square micrometer. Such devise with microchannel's area, A, can be described using the harmonic oscillator model with an effective mass, m, and a resonant frequency f. To measure the relative frequency shift $\Delta f/f$ due to the small added surface mass $\Delta\sigma = \frac{\Delta m}{A}$ we apply the eq. (3.22)

$$\frac{\Delta f}{f} = -\frac{1}{2}\left(\frac{A}{m}\right)\cdot \Delta\sigma \,. \tag{3.22}$$

Eq. (3.22) implies that the frequency shift and resonant frequency ratio is related to the ratio of the surface area over mass and it can be improved by thickening the fluid layer and the channel walls. Furthermore, the SMRs have to be under continuous fluid flow for real-time data collection.

In 2007, Burg, Thomas P., et al. [61], demonstrated a SMR that could weigh single nanoparticles, single bacterial cells and sub-monolayers of proteins with a resolution bellow to sub-femtogram (Figure3.8). A SMR device transforms the mass difference into changes in resonant frequency. The fluid flows inside the microchannels

delivering biomolecules, cells and any other particle. The particles bind on the surface and thus they increase the mass of the channel (Figure 3.8b). In case of no particle binding, the particles flow inside the microchannels and the detected signal refers to the particles' position. The peak frequency shift induced at the apex can quantify the mass of each particle inside the SMR device (Figure 3.8c).

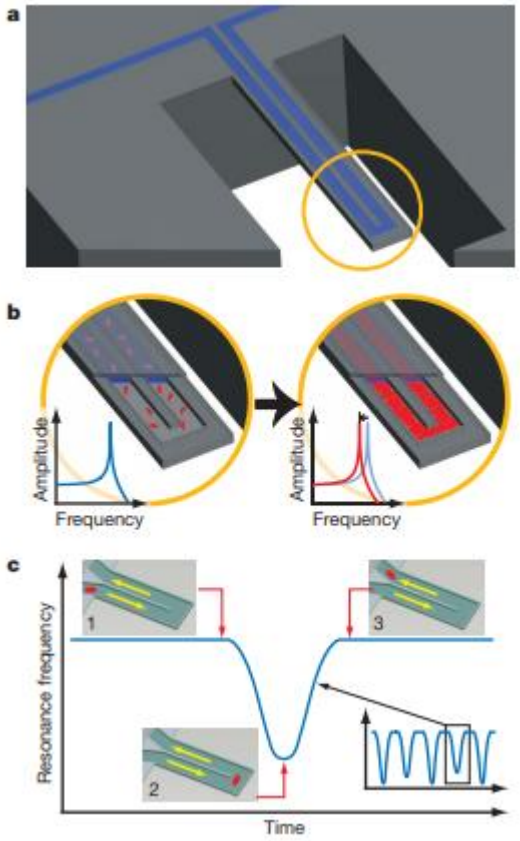

Figure 3.8 A SMR device employing two mass measurement modes [61].

Three years later, in 2010, Lee, J., et al. [62], demonstrated the first SMR device with Piezoresistive sensor for read-out. The SMR device was fabricated to measure micron-sized particles and cells with a mass sensitivity ~3.4 fg in 1 KHz bandwidth. This result is highly comparable to the conventional optical method. This work, paved the way for versatile, more compact and reliable SMR devises. In 2012 [63], Patel, Ankit R. et al. demonstrated a new characterization method to distinguish submicrometer, subvisible particles by measuring the difference of the buoyant mass of the particles in aqueous solution. Furthermore, they managed to apply the current method to high-concentration monoclonal antibody solution. In the same year 2012 [64], a SMR device for density

and viscosity is demonstrated. In 2015 [65], Olcum et al. presented a new method which takes the advantages of the four flexural modes of the SMR devise to determine the position as well as the mass of the tested particles with a resolution of 150 nm and 40 attograms at high speed. In 2018, De Pastina, A. et al. [66], fabricated a transparent arrays of SMR with a piezoelectric transducer achieving a mass responsivity of 1125 ± 0.06 mHz/pg. They also demonstrated for the first time independent actuators of each resonator (Figure 3.9).

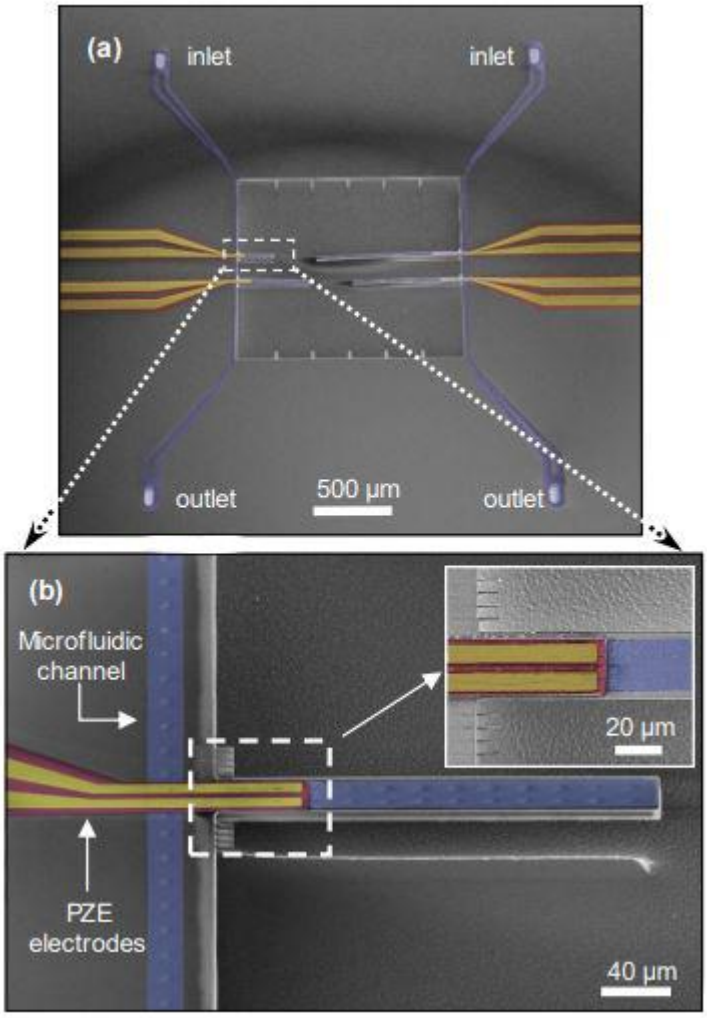

Figure 3.9 A SEM image of the SMR arrays with the independent Piezoelectric actuators. The colors have been added later in the PC. The microfluidics channel are indicated with cyan color while the piezoelectric electrodes with yellow.

CHAPTER 4. STATE-OF-THE-ART FEM MODELING OF MICROCANTILEVERS

Finite Elements Method offer the opportunity to study with high accuracy complex and difficult scientific and engineering problems that could be very expensive, time consuming and difficult to elaborate in real life. Furthermore, many experiments need to be repeated more than twice for well-accepted results. This, increases more the difficulty for a real life complex experiment. With the advances in computer science and hardware developing, the simulations' results are getting closer to the reality and can be employed within a reasonable time frame.

In the field of microcantilevers, FEM simulations were used to predict or to confirm the experimental data. To our knowledge, the Finite Element Method (FEM) was initially introduced for microcantilever biosensors in 2006 [10]. In that paper, the residual stress distributions inside the micro-fabricated bimorph cantilevers of different thickness was modeled. A contact model was introduced to calculate the influence of contact on the residual stress following a heat treatment process. The characterization of the bimorph cantilevers composed of thin Au films deposited on thick poly-silicon or silicon-dioxide beams was performed using an analytical modeling approach. Using FEM, a thermal elastic–plastic model was utilized to estimate the residual stress distribution across the cantilever cross-section and to determine the beam's deflection following heat treatment. Furthermore, they investigated the influences of the beam material and thickness on the residual stress distribution and tip. Since then, a lot of work has been done for the microcantilever and SMRs improvement. In 2018 Packirisamy et al. used two parallel, perpendicular to microcantilever deflection direction, microfluidic channels made from polydimethylsiloxane (PDMS), to investigate the 2D and the 3D behavior of the suspended polymeric microfluidics using FSI employing FEM [11] (Figure 4.1).

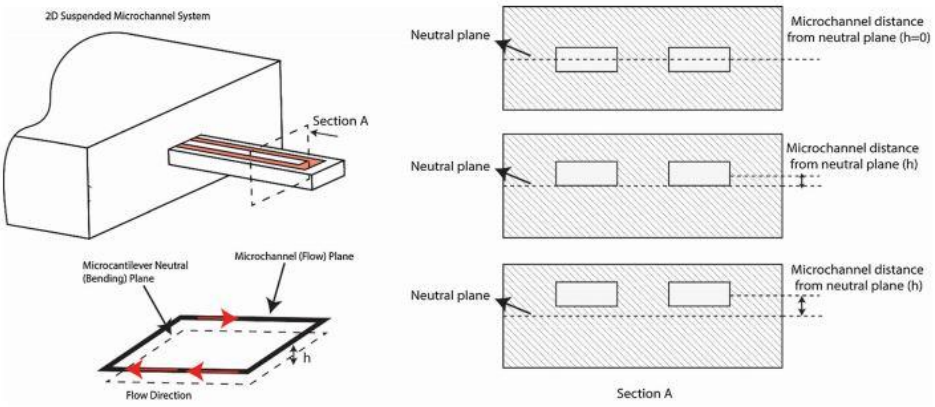

(A)

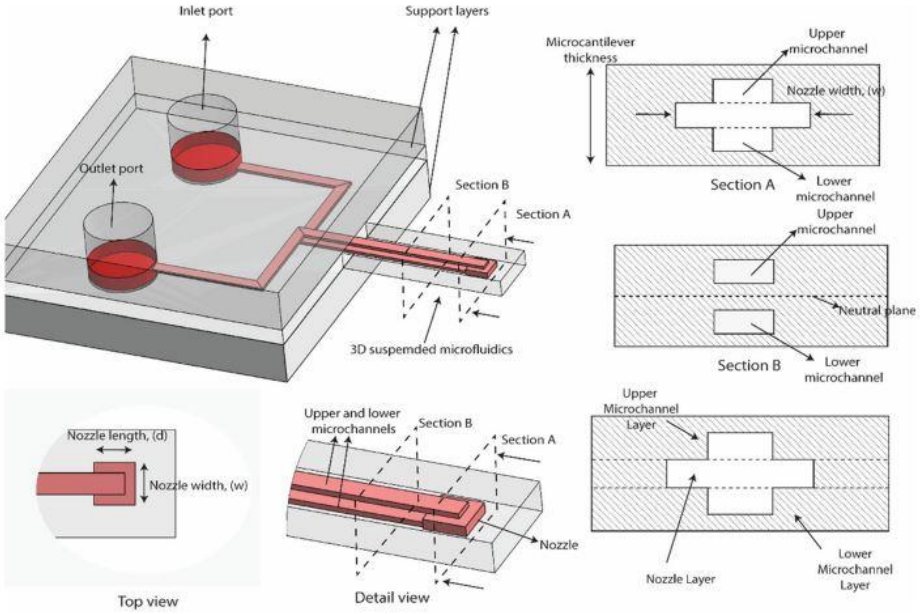

(B)

Figure 4.1 (A) 2D and (B) 3D SMR designs with different microfluidics positions and designs.

The 2D design (Figure 4.1 A), had a microchannel size of 200x100 μm, microcantilever size 6000x1000x600 μm, the fluid tested was the water with initial constant velocity 30 mm/s and PDMS as the solid material. The fluid flow inside the microchannel is shown below (Figure 4.2).

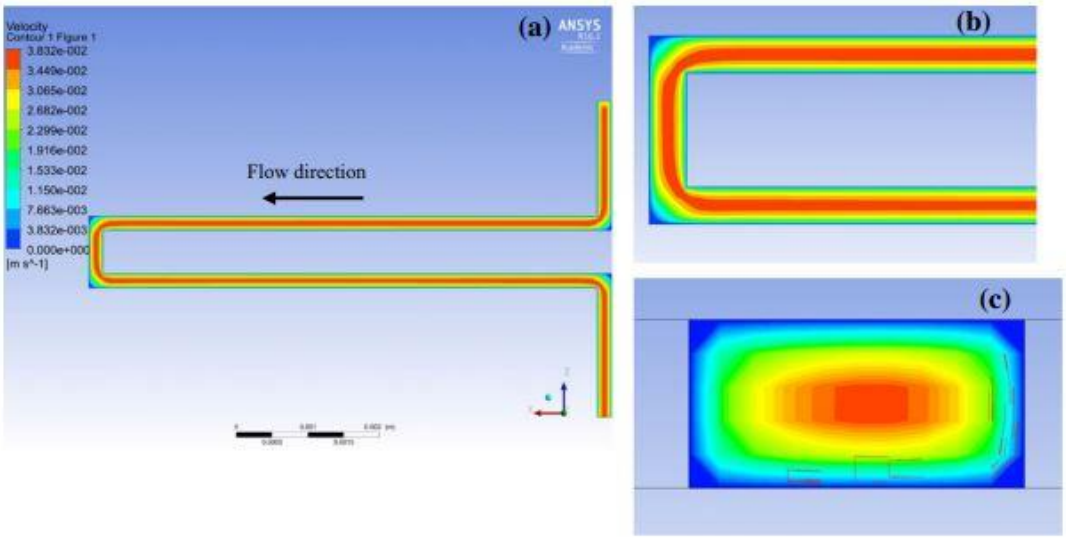

Figure 4.2 (a) Top view of the fluid velocity contours, (b) detailed view of the fluid flow and (c) a fluid flow cross section contour.

They show that a suspended microcantilever with microfluidics channel above the beam's natural plane, is more sensitive than the one in which the microfluidics channel is on the natural plane (Figure 4.3).

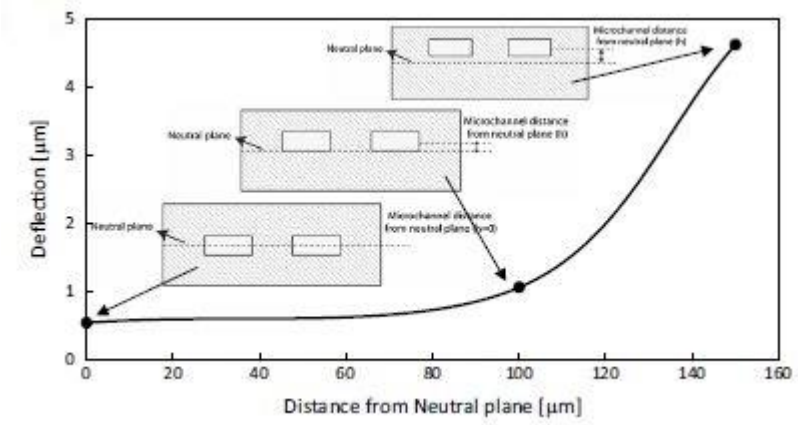

Figure 4.3 Microcantilever's vertical deflection against the microchannel's distance of the natural plane.

The 3D design (Figure 4.1 B), had a microchannel size of 200x100 µm, microcantilever size 6000x2000x600 µm, the fluid tested was the water with initial constant velocity 30 mm/s and PDMS as the solid material. The fluid flow inside the microchannel is shown in (Figure 4.4).

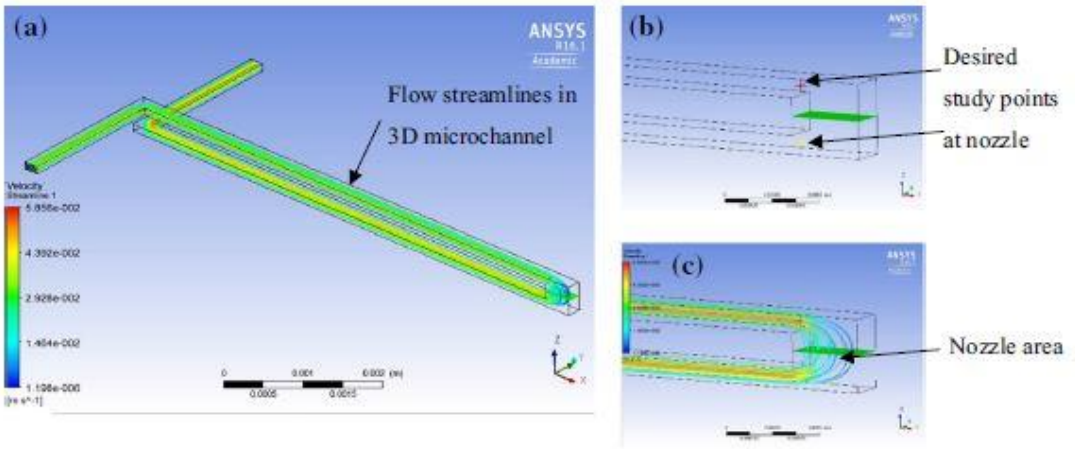

Figure 4.4 (a) Top view of the fluid velocity streamlines, (b) detailed view of the end part of the suspended microchannel (c) detailed view of the fluid flow going from the upper to the bottom channel through the nozzle area.

They also show that the design that deflects the most is that with a pyramid like nozzle design (Figure 4.5).

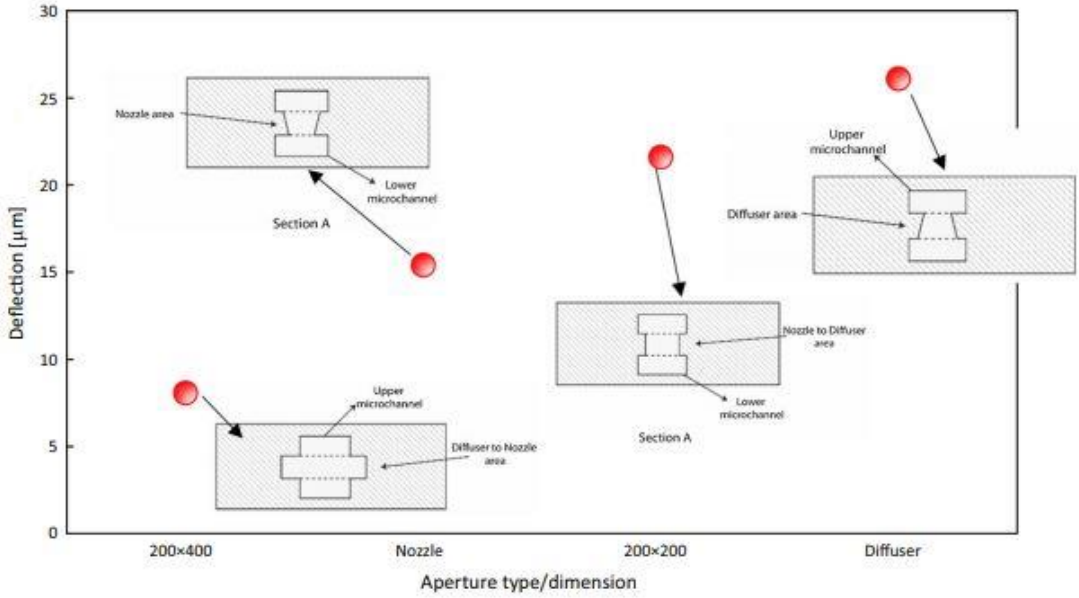

Figure 4.5 Beam's deflection against the nozzle design.

CHAPTER 5. BIOSENSOR'S MODELING

5.1 Introduction

In this part, the proposed geometries of the suspended microcantilevers used in the present master thesis will be presented as well as the hypothesis made to solve the problem, the boundary conditions and their properties.

In this work, a suspended microcantilever biosensor is simulated for a LoC and a PoC device fabrication for the determination of the dynamic viscosity of the Newtonian and Non-Newtonian fluids. In a suspended microcantilever biosensor, a microfluidic channel is combined with a micromechanical biosensor, forming a well-integrated microelectromechanical system (Figure 5.1). The working principal of this kind of biosensor is simple. A fluid enters inside the microfluidics channel and its viscosity and velocity forces the microcantilever to bend downwards. The sensitivity of the biosensor is analogous to the deflection of the microcantilever's tip. For the purposes of this work, Newtonian and non-Newtonian fluids were taken into account. The fluids' behavior inside the microchannel, as well as, the tip deflection due to their viscosity and velocity, was studied. Two different biosensor's materials were used to examine the perfect candidate for the microfabrication. Moreover, five different biosensors' geometries was designed and simulated. Furthermore, a comparison between *one-way* and *two-way* FSI. The current work is a complete study of the behavior of a suspended microcantilever biosensor.

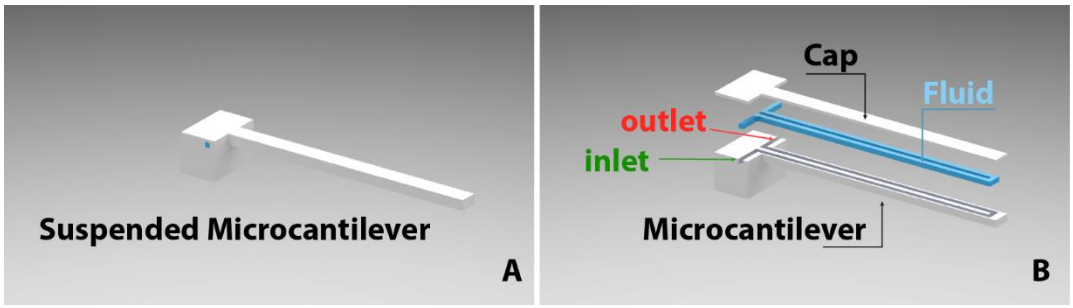

Figure 5.1 Schematic representation of a suspended microcantilever biosensor. A) The biosensor assembly and B) the biosensor's components.

5.2 Materials and Methods

Two commercial softwares, one for the design and one for the simulation experiments were used. The geometries were designed using the CAD software Solidworks®, while the simulations were performed using ANSYS.

Solid Materials

Two polymer materials used for the biosensor examination, PMMA and PDMS. The materials' properties are presented in Table 5.1. Both polymers are widely used in microfluidics and biosensor technologies. PMMA and PDMS are considered to be as thermoplastic polymers meaning that their mechanical properties change with respect to the temperature. In this study, the materials were treated as isotropic and linear elastic.

Linear Elastic Isotropic Model

To describe mathematically the linear elastic model, it would be convenient to introduce the matrix form of the strain eq. (5.1) and stress eq. (5.2).

$$[\boldsymbol{\varepsilon}]^T = [\varepsilon_{11}\ \varepsilon_{22}\ \varepsilon_{33}\ \gamma_{12}\ \gamma_{23}\ \gamma_{13}]\,, \tag{5.1}$$

where, $\gamma_{ik} = 2\varepsilon_{ik}$, is the engineering shear strain and

$$[\boldsymbol{\sigma}]^T = [\sigma_{11}\ \sigma_{22}\ \sigma_{33}\ \sigma_{12}\ \sigma_{23}\ \sigma_{13}]\,. \tag{5.2}$$

For a linear elastic material, Hooke's law is applied, eq. (5.3)

$$\boldsymbol{\sigma} = \boldsymbol{C\varepsilon}, \qquad or \quad \sigma_i = C_{ik}\varepsilon_k, \quad i,k = 1,2,\dots,6 \tag{5.3}$$

where, C_{ik} , are the elastic constants of the material and can be expressed in two possible ways. It can either be the *Elastic Modulus or Young's Modulus,* $\hat{E}$, or the *Poisson's Ratio, v*. The inverse formula of the eq. (5.3) is given by

$$\boldsymbol{\varepsilon} = \boldsymbol{C^{-1}\sigma}, \qquad or\ \varepsilon_i = C_{ik}^{-1}\sigma_k, \quad i,k = 1,2,\dots,6 \tag{5.4}$$

or using the matrix form

$$\boldsymbol{\varepsilon} = \begin{Bmatrix} \varepsilon_{11} \\ \varepsilon_{22} \\ \varepsilon_{33} \\ \gamma_{12} \\ \gamma_{23} \\ \gamma_{13} \end{Bmatrix} = \frac{\mathbf{1}}{\hat{E}} \begin{bmatrix} 1 & -v & -v & 0 & 0 & 0 \\ -v & 1 & -v & 0 & 0 & 0 \\ -v & -v & 1 & 0 & 0 & 0 \\ 0 & 0 & 0 & 1+v & 0 & 0 \\ 0 & 0 & 0 & 0 & 1+v & 0 \\ 0 & 0 & 0 & 0 & 0 & 1+v \end{bmatrix} \begin{Bmatrix} \sigma_{11} \\ \sigma_{22} \\ \sigma_{33} \\ \sigma_{12} \\ \sigma_{23} \\ \sigma_{13} \end{Bmatrix}. \tag{5.5}$$

Table 5.1 Materials' Properties

Properties	PDMS[1]	PMMA[2]
Density (Kg/m^3)	970	1180
Young's Modulus (Pa)	3.6x10^5	2.45x10^9
Poisson's Ratio	0.49	0.35

1. http://www.mit.edu/~6.777/matprops/pdms.htm
2. http://www.mit.edu/~6.777/matprops/pmma.htm

Strains and nodal displacements can be related as,

$$\{\boldsymbol{\varepsilon}\} = [B]\{\boldsymbol{u}\}, \tag{5.6}$$

where [*B*], is the displacement differentiation matrix, eq. (5.7), that combines the nodal displacements {**u**}, eq. (5.8) inside an abstract three- dimensional finite element with the shape functions [N], eq. (5.9).

$$[B] = \begin{bmatrix} \frac{\partial N_i}{\partial x} & 0 & 0 \\ 0 & \frac{\partial N_i}{\partial y} & 0 \\ 0 & 0 & \frac{\partial N_i}{\partial z} \\ \frac{\partial N_i}{\partial y} & \frac{\partial N_i}{\partial x} & 0 \\ 0 & \frac{\partial N_i}{\partial z} & \frac{\partial N_i}{\partial y} \\ \frac{\partial N_i}{\partial z} & 0 & \frac{\partial N_i}{\partial x} \end{bmatrix}, \tag{5.7}$$

$$\{\boldsymbol{u}\} = \{u_1\ v_1\ w_1\ u_2\ v_2\ w_2\ \ldots\}, \tag{5.8}$$

$$[N] = \begin{bmatrix} N_1 & 0 & 0 & N_2 & 0 & \ldots \\ 0 & N_1 & 0 & 0 & N_2 & \ldots \\ 0 & 0 & N_1 & 0 & 0 & \ldots \end{bmatrix}. \tag{5.9}$$

The displacement {**U**} at some point inside a finite element can be given as

$$\{\boldsymbol{U}\} = [N]\{\boldsymbol{u}\}\,. \tag{5.10}$$

Fluids

Apart from the biosensor's materials, different Newtonians and Non-Newtonians fluids were used and they are presented in Table 5.2. Fluids can be mathematically described using the Navier-Stokes equation, eq. (5.11).

$$\rho\left[\frac{\partial\vec{u}}{\partial t} + \vec{u}\nabla\vec{u}\right] = -\nabla P + \mu\nabla^2\vec{u} + \overrightarrow{f_{ext}}\,, \tag{5.11}$$

where ρ is the fluid's density, u is the velocity field, P is the pressure, μ, is the dynamic viscosity of the fluid and $\overrightarrow{f_{ext}}$ is the external forces acting on the fluid flow.

Table 5.2 Fluids' Properties

Fluids	Density (kg/m^3)	Dynamic Viscosity (Kg/ms)	
Blood*	1050	$3.5\text{x}10^{-3}$	
Water	997	$8.9\text{x}10^{-4}$	
Acetone	784	$3.16\text{x}10^{-4}$	
Propanol	803	$1.92\text{x}10^{-3}$	
Acetic Acid	1050	$1.15\text{x}10^{-3}$	
		High Shear Viscosity	Low Shear Viscosity
Blood 35%H**	1050	0.00313	0.056
Blood 40%H**	1050	0.0035	0.056
Blood 48%H**	1050	0.005	0.056

* As Newtonian

** As Non-Newtonian (Bird-Carreau Model) "Siebert, M. W., & Fodor, P. S. (2009). Newtonian and non-Newtonian blood flow over a backward-facing step–a case study. In *Proceedings of the COMSOL Conference, Boston*."

5.3 Assumptions and Boundary Conditions

In order to study the suspended microcantilever biosensor, few necessary assumptions must be taken into account. First of all, we consider a steady state, laminar, incompressible flow. The fluids tested were Newtonian and non-Newtonian. The fluid walls are adiabatic, the acting forces on the microchannel's walls have an impact to the structure and thus the microcantilever's beam is forced to bend downwards. Also, the beam's length is much bigger than its width and thickness. The gravitational force is taken into account in both CFX and in Static Structural.

Boundary Conditions

One of the most important step to solve a Finite Element Simulation, is the setting of the boundary conditions of the problem. The applied boundary conditions for the fluid domain, F1 is presented in (Figure 5.2). Constant fluid velocities applied at the inlets of the fluids 'domains examining two values 0.1 and 1 μm/s. At the outlet of the domains, 0 Pa pressure was applied generating a pressure driven flow. Finally, all the wall's velocity components set to be zero (no slip condition). For the solid domain, B1, the above and the front side of the biosensor, as well as the whole beam area, is set to be deformable along the y-axis as it is depicted in (Figure 5.3 B). On the contrary, the back and the bottom side were considered as fixed areas (Figure 5.3 C). In order to examine the beam's deformation due to the fluid's effect, a fluid solid interface boundary condition is used for transferring the generated loads from the CFD analysis to the mechanical one. Gravitational forces were also taken into account. The same boundary conditions were applied in F2 and B2 domains also.

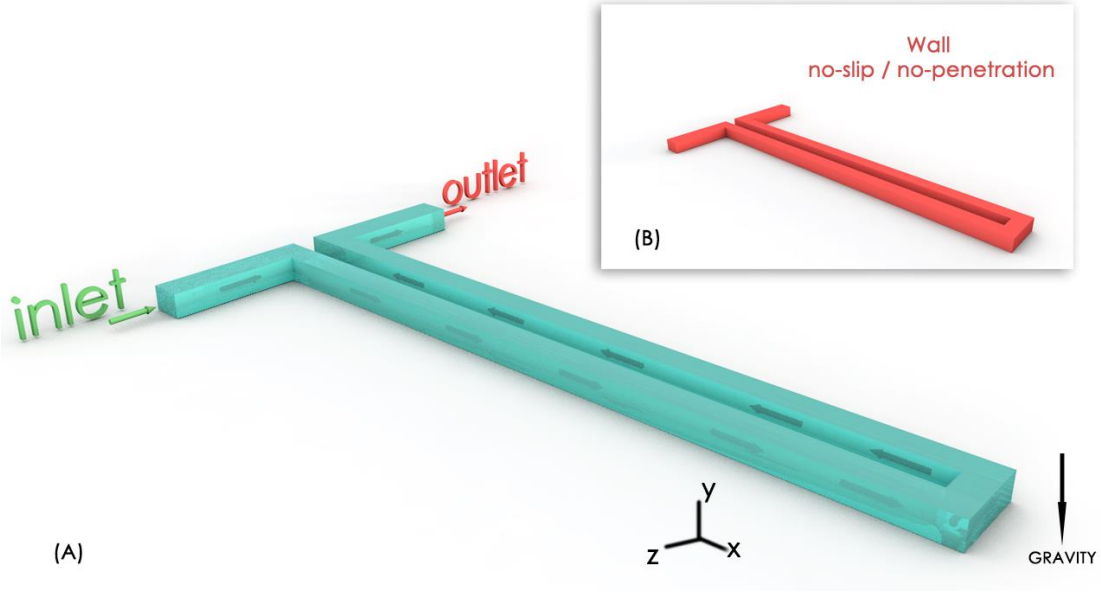

Figure 5.2 The boundary conditions of the fluid domain (A). The fluid enters the microchannel with a constant velocity (μm/s) and exists with a pressure 0 Pa. The boundary conditions on fluid wall were set as no-slip / no-penetration and it is shown with red color (B)

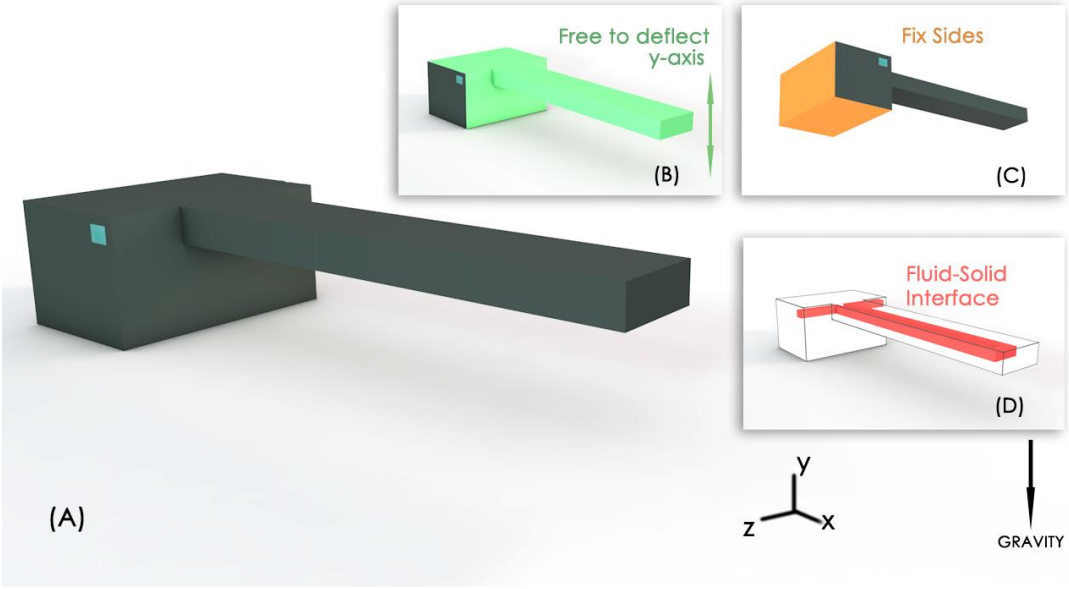

Figure 5.3 The boundary conditions of the solid domain (A). With green color are depicted the sides that are free to deflect (B), while with orange color the fix sides (C) and with the red color is the fluid-solid interface (D).

5.4 Microfluidics and Biosensor Geometries and Meshing

5.4.1 Geometries

Fluid Domains

Two microchannel geometries have been tested in this work. The first microchannel was a Π-like shape with the flow parallel to the xz-axis (Fluid 1, F1) (Figure 5.4), while in the second one (Figure 5.5), the fluid flows vertically to the xz-axis, having a square nozzle to connect the upper with the lower channel (Fluid 2, F2).

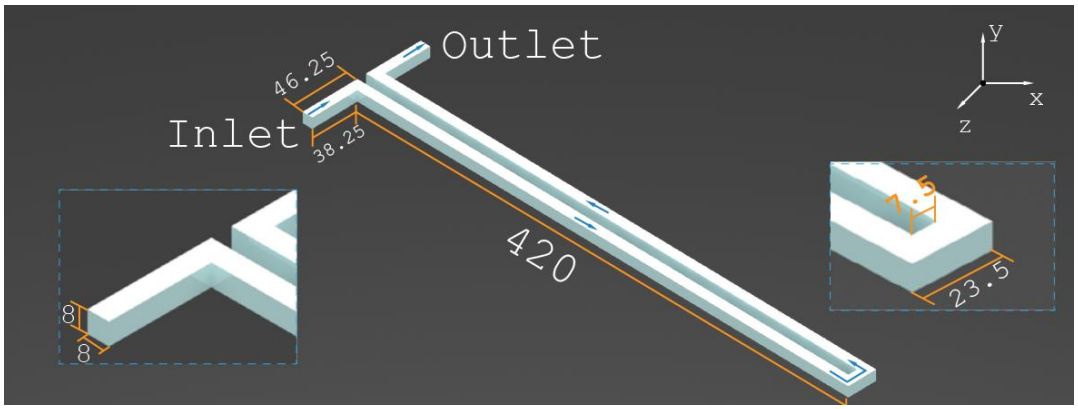

Figure 5.4 The geometry F1, with the fluid flow parallel to the xz-axis. Scale in micrometers.

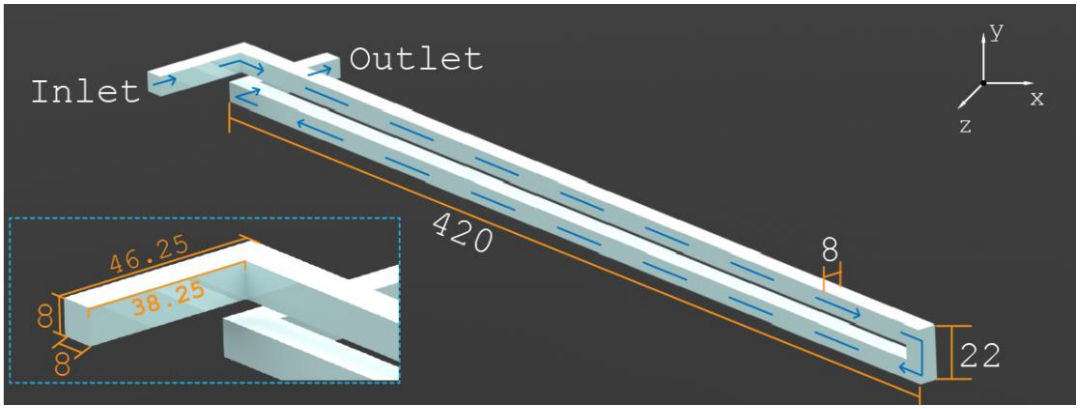

Figure 5.5 The geometry F2, with the fluid flow vertically to the xz-axis. Scale in micrometers.

Solid Domains

Two different biosensor geometries (Biosensor 1, B1 and Biosensor 2, B2) designed to enclose the fluid domain one for the F1 (Figure 5.6) and one for the F2 (Figure 5.7) geometry, respectively. Both the biosensors have a solid base in one end and a hollow free cantilever tip in the other end.

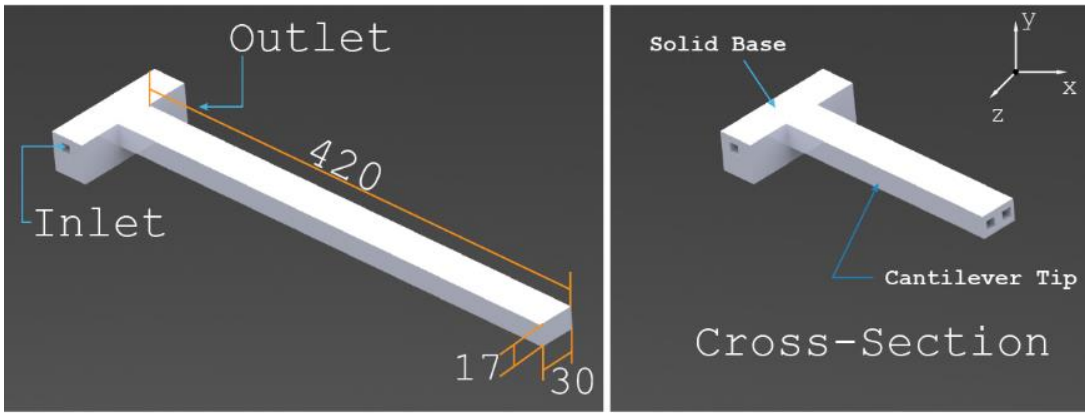

Figure 5.6 The geometry B1, with the fluid flow parallel to the xz-axis. Scale in micrometers.

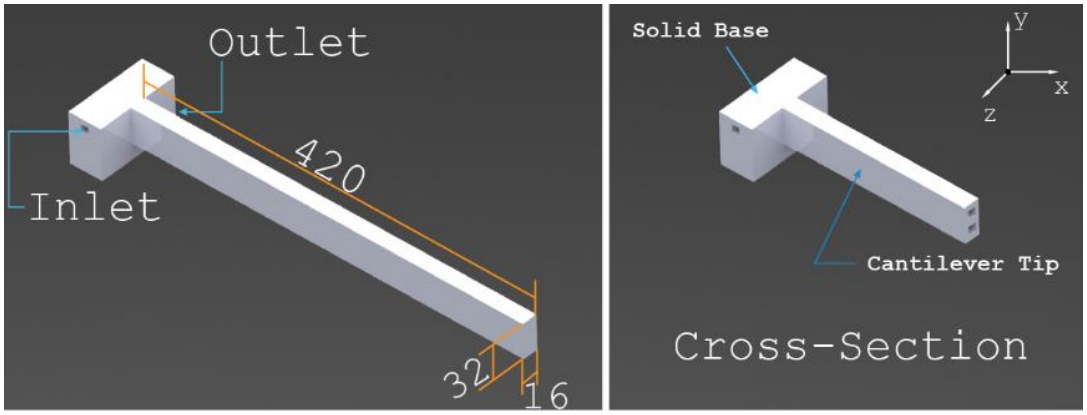

Figure 5.7 The geometry B2, with the fluid flow vertically to the xz-axis. Scale in micrometers.

5.4.2 Meshing

Fluid Domains

In order to mesh properly the fluid domains, it was necessary to divide them into smaller subdomains (Figure 5.8). Then, the following meshing settings were applied (Table 5.3). The meshed geometries are presented below in the (Figures 5.9-5.10).

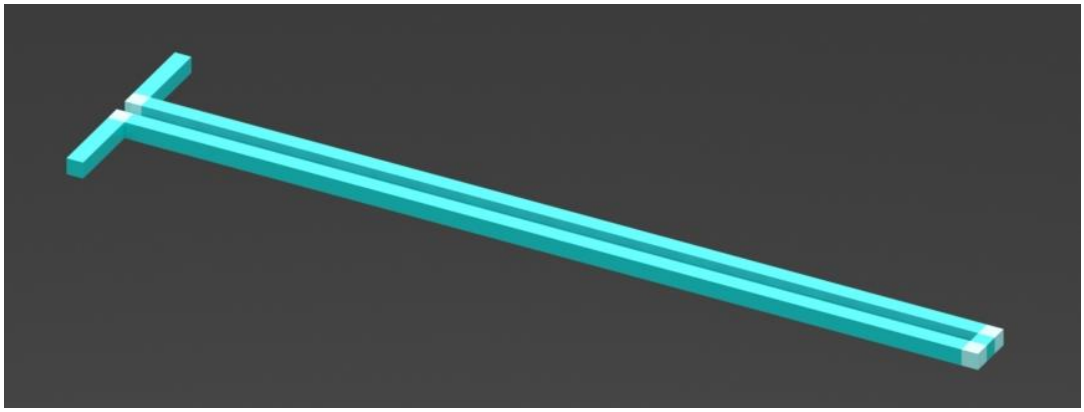

(A)

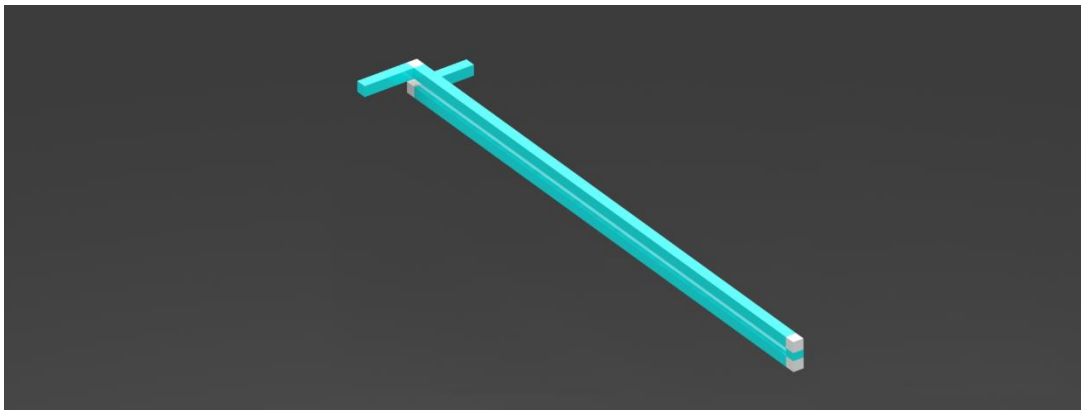

(B)

Figure 5.8 The fluid geometries divided into smaller subdomains for better meshing handling. (A) The F1 and (B) the F2 microchannel design.

Table 5.3 Meshing properties for the fluid domains

Properties	Values	
	Geometry F1	Geometry F2
Relevance	100	100
Element Order	Linear	Linear
Size Function	Curvature	Curvature
Relevance	Fine	Fine
Span Angle Center	Fine	Fine
Element Size	0.6 μm	0.6 μm
Nodes	305564	303996
Element	261950	261950

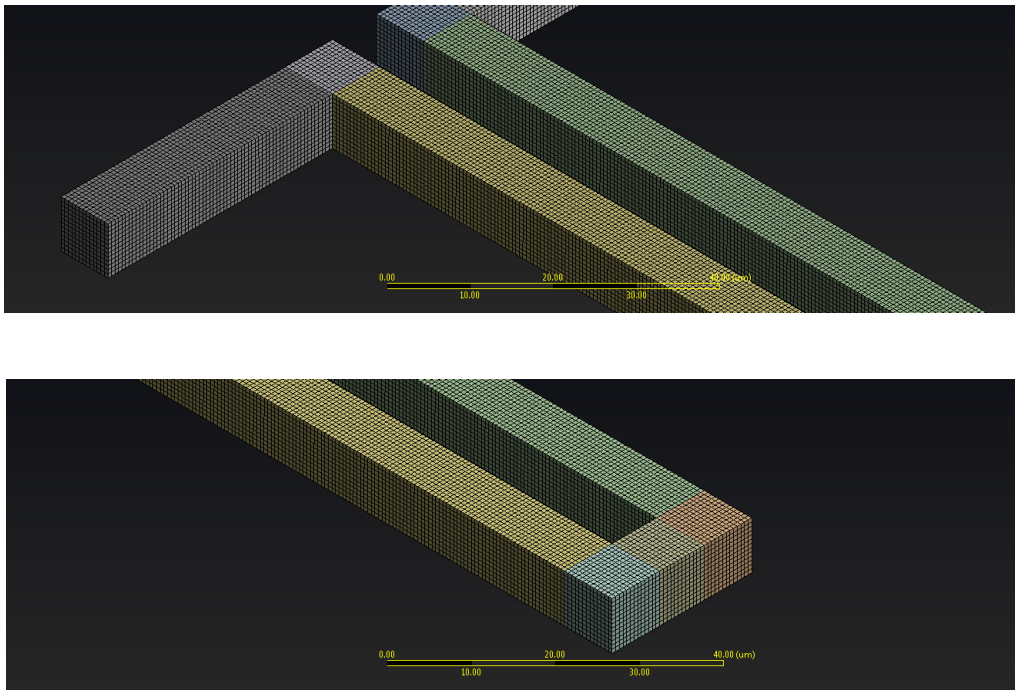

Figure 5.9 Meshing detail of the geometry F1.

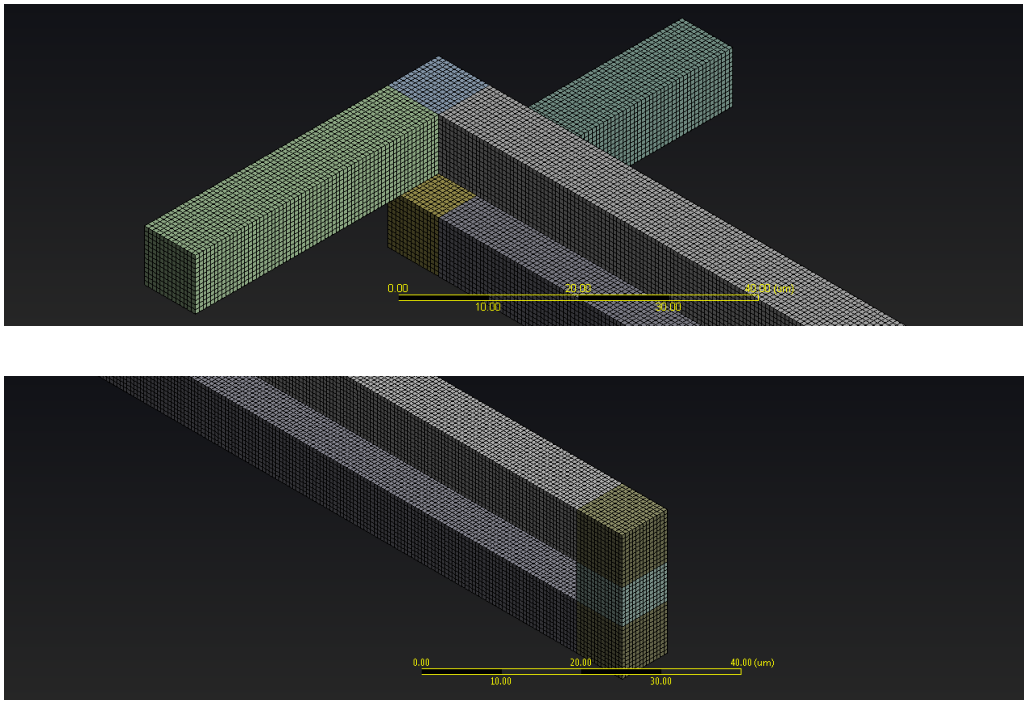

Figure 5.10 Meshing detail of the geometry F2.

Solid Domains

The biosensor geometries were meshed using the same meshing properties with the fluid domains generating hexahedrons elements as it is shown in (Table 5.4). Figure 5.11.B1 and Figure 5.11.B2 show the meshing results.

Table 5.4 Meshing Properties using the ANSYS Static Structural Module

Properties	Values	
	Geometry B1	Geometry B2
Relevance	100	100
Element Order	Linear	Linear
Size Function	Adaptive	Curvature
Relevance	Fine	Fine
Span Angle Center	Fine	Fine
Sizing: Element Size	0.6 μm	0.6 μm
Nodes	1533645	1535329
Element	1336553	1423587

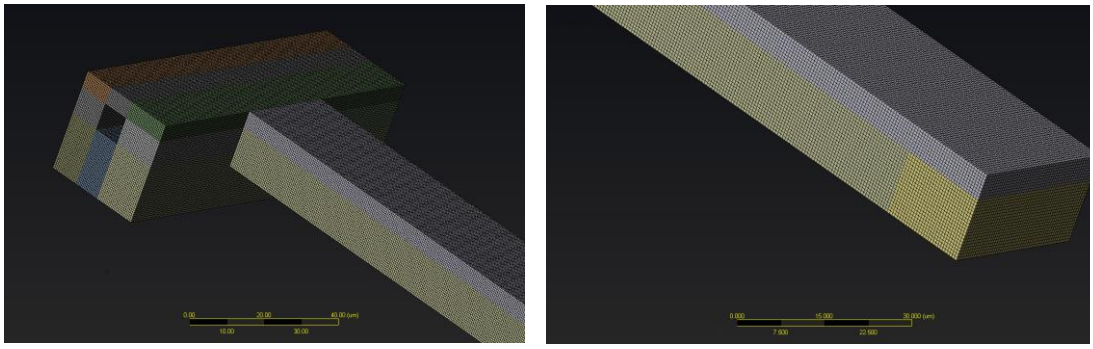

Figure 5.11.B1 Meshing detail from the B1 geometry, with the fluid flow parallel to the xz-axis

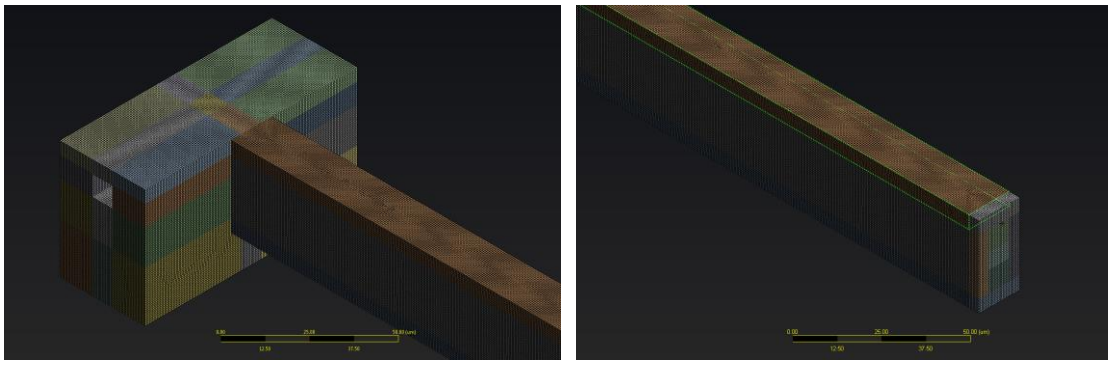

Figure 5.11.B2 Meshing detail from the B2 geometry, with the fluid flow vertically to the xz-axis

5.4.3 Meshing Quality

Fluid Domains

The mesh validation was tested using the Element Quality and the Skewness diagnostic tools. The Element Quality diagnostic tool, ranges between 0 and 1, with a mesh value equal to 1 to indicate a perfect cube. The 0 value shows an ill mesh or a negative volume (Figure 5.12.F1 and 5.12.F2). The Skewness diagnostic tool, ranges from 0 to 1, with a value equal to 0, indicating a high quality mesh (Figure 5.13.F1 and Figure 5.13.F2). The values of the Element Quality, as well as the values of the Skewness, are presented in the (Table 5.5). From the diagnostic values, the mesh produced in both cases is characterized as high quality mesh.

Solid Domains

In (Figure 5.14.B1 and Figure 5.14.B2) the Element Quality of each geometry is presented while in (Figure 5.15.B1 and Figure 5.15.B2) Skewness factor is showed. The maximum and the minimum values of each diagnostic tools are presented in the (Table.5.6).

Results

Table 5.5 Mesh Diagnostic Tools for the fluids domains

Geometry	Diagnostic Tools	Maximum Value	Minimum Value
F1	Element Quality	1	0.99941
	Skewness	0.006074	1.5567×10^{-7}
F2	Element Quality	1	0.99888
	Skewness	0.0057446	1.1818×10^{-6}

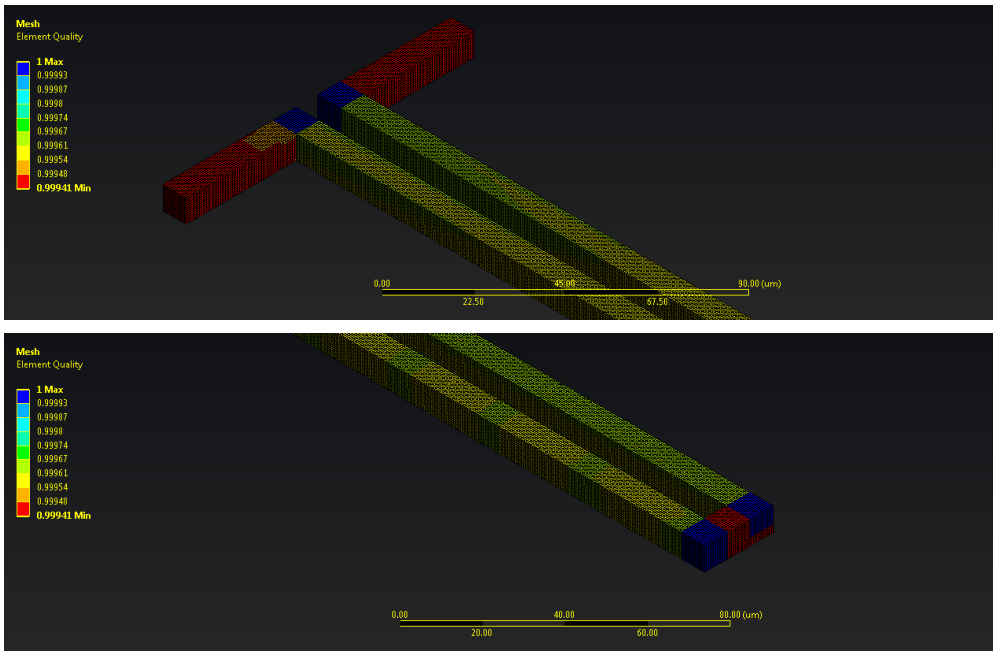

Figure 5.12.F1 The Element Quality values for the F1

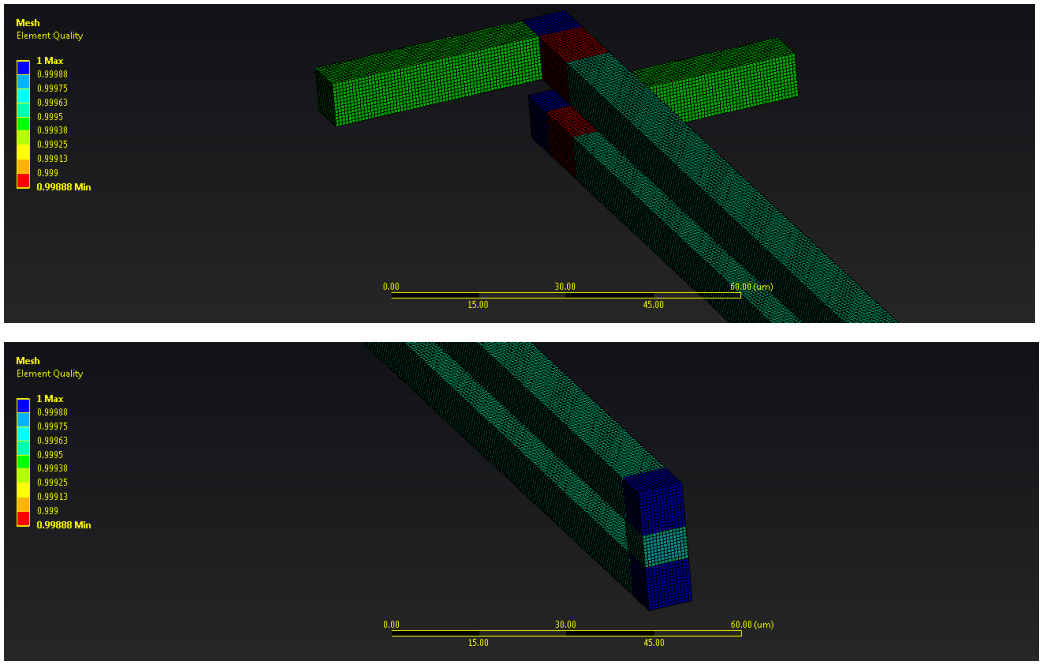

Figure 5.12.F2 The Element Quality values for the F2

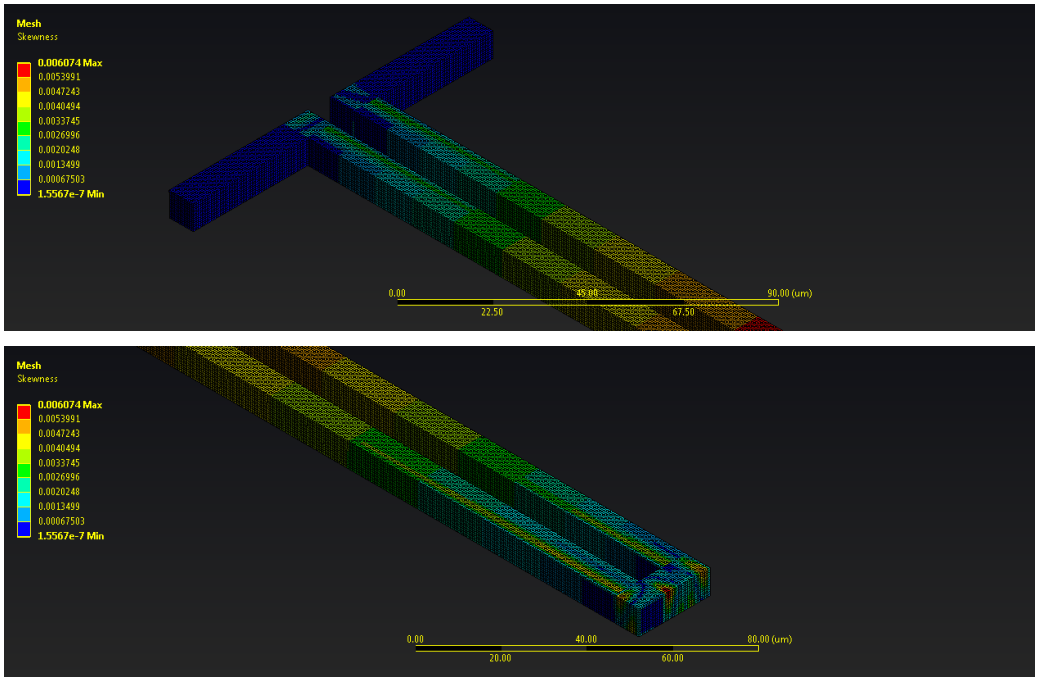

Figure 5.13.F1 The Skewness Quality values for the F1

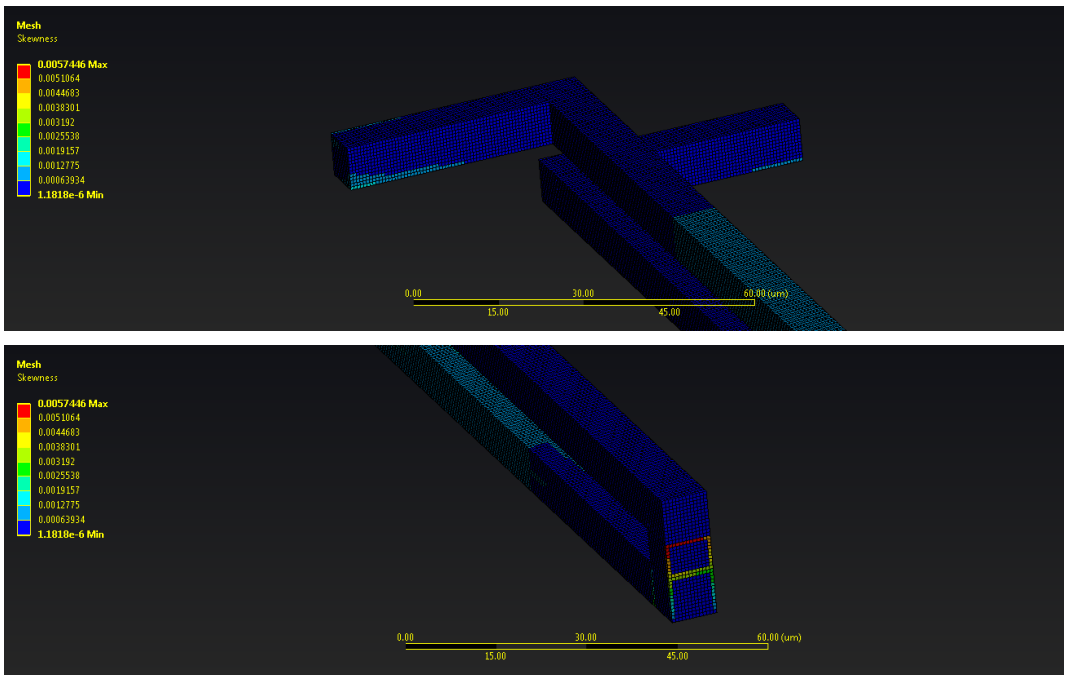

Figure 5.13.F2 The Skewness Quality values for the F2

Table 5.6 Mesh Diagnostic Tools for the biosensors domains

Geometry	Diagnostic Tools	Maximum Value	Minimum Value
B1	Element Quality	0.99997	0.9408
	Skewness	0.21756	1.3057×10^{-10}
B2	Element Quality	1	0.012774
	Skewness	1	1.3065×10^{-10}

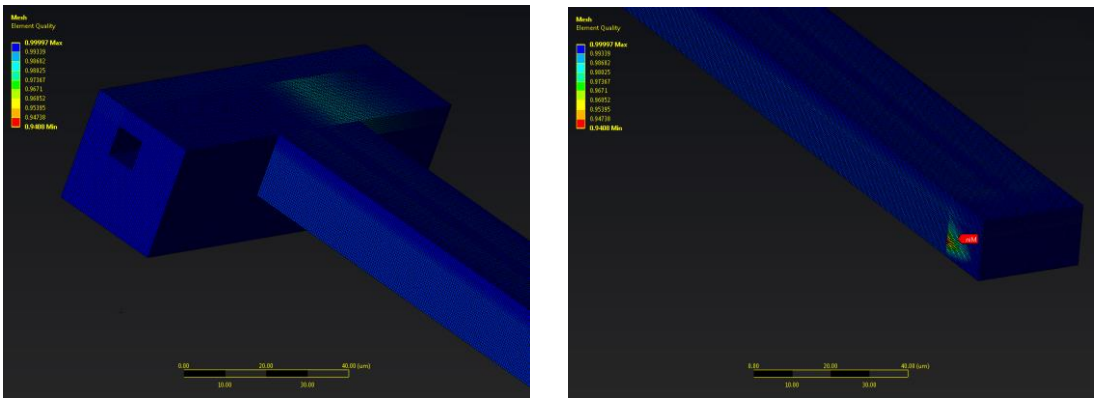

Figure 5.14.B1 The Element Quality values for the B1

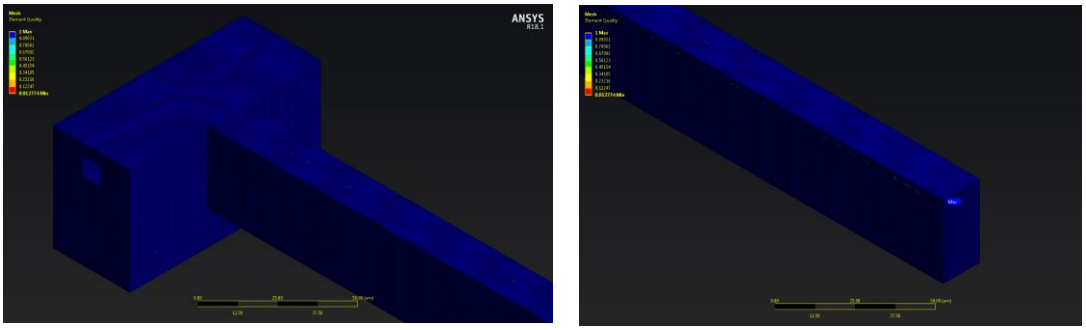

Figure 5.14.B2 The Element Quality values for the B2

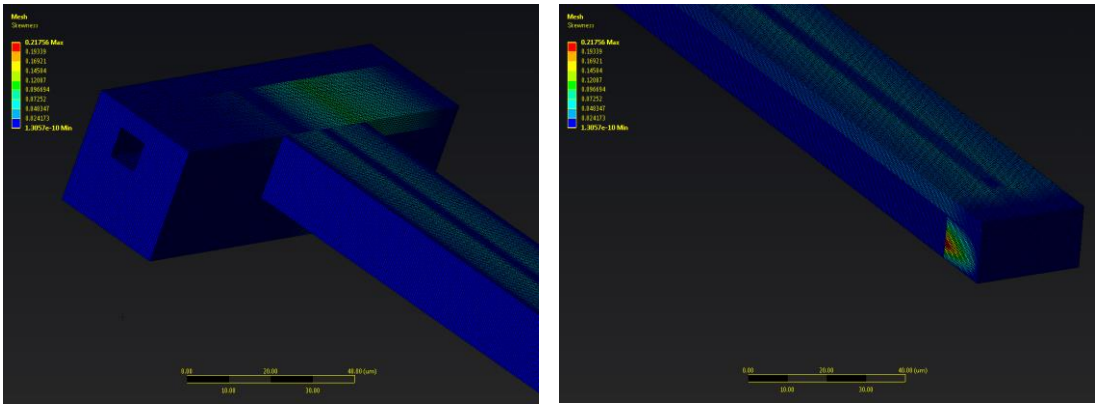

Figure 5.15.B1 The Skewness values for the B1

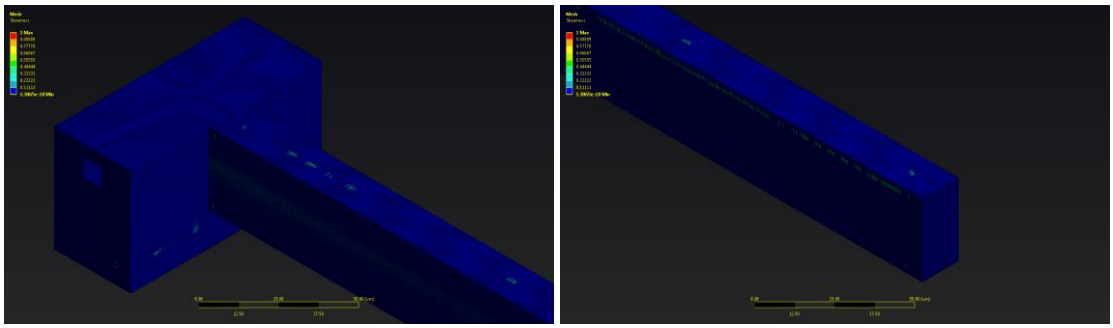

Figure 5.15.B2 The Skewness values for the B2

CHAPTER 6. FINITE ELEMENTS METHOD

6.1 Finite Elements Method

6.1.2 History

During the World War II, two scientists A. Hrennikoff (a Russian-Canadian Structural Engineer) [66] and R. Courant (a German-American mathematician) [67] suggested a powerful computational technique to simulate and provide approximate solutions in a plethora of difficult scientific and engineering problems. Among the creators was a Greek pioneer John Hadjiargyris who extend this technique based on the Courant's work [68]. This technique is known as the "**Finite Element Method**" or FEM and since then has become an essential mathematical tool for modeling and designing complex physical problems. Fluid flows, transfer phenomena, mechanical analysis, electromechanical or electromagnetics, optics and laser physics are few of the typical scientific and engineering examples in which FEM is applied.

6.1.3 Basic Concept

The discretization of a complex geometrical design into smaller finite subdomains that are known as **elements**, is the main idea of the FEM. After the discretization, algebraic partial differential equations are applied on the discrete elements. All the elements are connected to each other by their "common" **nodes**. The elements and the nodes consist the generated **mesh**. Each node determines the coordinate location in which the actions and the degrees of freedom of the physical problem exist. Then, a numerical solution is extrapolated to boundary value problems for partial differential equations and then assembled into larger system of equations that describe the entire problem. As it is expected, the number of the discrete elements improves the accuracy and leads into an exact solution. Also, the shape of the element plays an essential role on either or not the problem reaches a final solution. Ideally, an exact and well accepted solution should be independent from the mesh size and the **convergence curves** of the mass and momentum residuals should be bellow 10^{-6} or at least 10^{-4}. The FEM can be used to solve either steady state or transient problems. For

the **steady state** problems, algebraic equations are used. For **transient** problems, numerical integration using methods such as Euler or the Runge-Kutta method have to be used [69]. The partial differential equations which describe the physical problem are transformed into numerical algebraic equations. A general form of such algebraic equation is presented below:

$$[\boldsymbol{K}]\{\boldsymbol{u}\} = \{\boldsymbol{F}\}\,, \tag{6.1}$$

K, is the stiffness matrix of the material, ***u***, is the nodal displacement vectors and ***F***, is the external loads.

6.1.4 Finite Element Analysis

The Finite Element Analysis or FEA, can be divided into seven steps:

I. Geometry Development

Using a Computer Aided Design (CAD) software, the desired geometry is designed with respect to the real analogous model and then it is imported inside the Finite Element Software (FES). However, simple geometries can be generated inside the FES, too. Once the geometry is designed, the next step is to be discretized into finite smaller subdomains as mentioned above.

II. Material Properties Assignment

In this step, the material's properties have to be defined such as the Bulk and Young Modulus, the Poisson's Ratio, the density, the heat capacitance etc.

III. Mesh Generation

A mesh is a grid that connects all the elements with their common nodes. A mesh can be either automatic or manually generated depending on the geometry's topology. There are two types of cell shapes for 2D problems and four basic three-dimensional elements for 3D problems [70].

Two-Dimensional Shapes: Triangles and Quadrilaterals.

a. The Triangles are the simplest type of mesh, always quick and easy to create.
b. The Quadrilaterals provide better results but they are often excluded from the mesh generator when the geometry has concave areas.

Three-Dimensional Shapes: Tetrahedrons, Pyramids, Triangular Prisms and Hexahedrons.

a. The Tetrahedrons: This type of mesh is the simplest and in most cases it can be generated automatically.
b. The Pyramids: This type of mesh is often used in hybrid meshes when square and triangular shapes coexist.
c. Triangular Prisms: They can solve boundary layer efficiently.
d. Hexahedrons: Are cubes which can provide highly accurate solutions (also known as brick elements).

IV. Physics

After the mesh generation, the physical model needs to be set. Plenty of physical models are available for a Finite Element Analysis such as Electromagnetics, Fluid Dynamics, Structural Mechanics, Thermodynamics, Optics, etc. Additionally, a lot of FESs offer multiphysics analysis for a complete solution in complex problems.

V. Boundary Conditions

In this step, the physical and mathematical problem needs to be specified. Initial Conditions, Boundary Conditions and Loads or Forces (external or internal) have to be set.

VI. Run Analysis

Since all the above have been set, the program tries to solve the equations by taking into account the boundary conditions to calculate the displacements, the strains, the natural frequencies or any other user specified data. During this step, many programs offer the opportunity for the Convergence Graph to be displayed on the monitor helping the user to understand the solution process.

VII. Results

The final step is the post process of the solution, in which the user can export the results and generate plots, pictures and animations. Here, the user can evaluate the results and proceed to another simulation or repeat the same if necessary.

6.1.5 Fluid Structure Interaction

There are a plethora of multi-physics cases in science and in engineering where interactions of different physical or chemical phenomena take place. The Fluid Structure Interaction (FSI) is one of these multi-physics cases where the fluid and the solid domain interact. Due to the difficulty to obtain an exact analytical solution for a FSI problem, analytical or experimental methods have to be used. In principle, there are two FSI approaches: ***monolithic*** and ***partitioned approach*** (Figure 6.1).

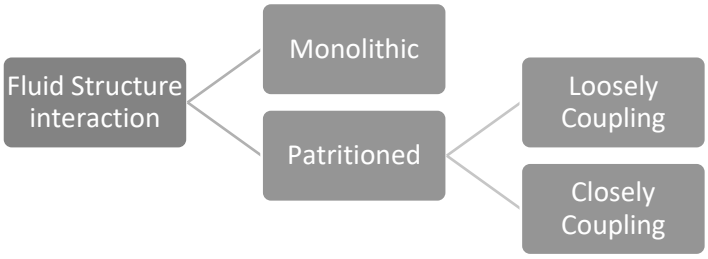

Figure 6.1 FSI classification approach.

Monolithic Approach

When a monolithic approach is used, both the fluid and the structure sub problems are treated as one global problem. In this case, the interaction between the fluid and the structure occurs synchronously. While this approach is more robust than the partitioned approach, it consumes more computational time and lacks software modularity [71, 72].

Partitioned Approach

In this approach, the FSI problem is divided into two separately sub problems, the fluid dynamics and the structural mechanics which are solved individually. In partitioned approach, the loads generated from the CFD are transferred and imported as boundary conditions to the mechanical analysis in their common interface. Thus, the fluid flow does not change while the mechanical analysis takes place [71, 72].

One and two way system coupling

The FSI simulation can be performed either using one or two-way system coupling. The FSI simulation is categorized as *one-way* when the CFD results influence the mechanical analysis and the structural reaction has minor impact to the fluid flow. On

the other hand, the FSI is considered to be *two-way* when the fluid flow affects the structural analysis and the outcome of the mechanical simulation affects the fluid flow.

6.2 Fluid flow

All the tested fluids in this work, can be considered incompressible. The governing equations for these fluids: the equation of balance of mass (continuity equation) and equations of balance of linear momentum are presented.

In order to derive the governing equations for the fluid flow, the control volume approach is adopted. The control volume is a fluid parcel fixed in space, with dimensions $dx, dy\ and\ dz$ (Figure 6.2) and constant volume, inside of which the fluid flows. Using the Cartesian coordinates, the control volume surrounds the point in space, with coordinates $x, y\ and\ z$ (Figure 6.2). The goal of the CFD is to determine the fluid variables, such as pressure and velocity. This approach is called the Eulerian description.

6.2.1 Governing equations of fluid flow

In (Figure 6.2.a) a control volume within a fluid flow domain is presented. In (Figure 6.2.b) an enlarged control volume is showed inside of which the mass fluxes through the elementary surfaces. With ρ, is the fluid density and the v_x, v_y, v_z are the velocity components. Using the mass balance equation within the control volume, the continuity equation is given as:

$$\frac{\partial \rho}{\partial t} + \nabla(\rho \vec{V}) = 0\ or\ \frac{D\rho}{Dt} + \rho\left(\nabla \cdot \vec{V}\right) = 0, \tag{6.2}$$

where, $\frac{D\rho}{Dt} = \frac{\partial \rho}{\partial t} + \left(\frac{\partial \rho}{\partial x_i}\right) v_i$ denotes the material derivative of the fluid density ρ. The material derivative $\frac{D\{*\}}{Dt}$ is used in the Eulerian description for any fluid quantity. The general form of this can be written as:

$$\frac{D\{*\}}{Dt} = \frac{\partial \{*\}}{\partial t} + \nabla\{*\} \cdot \vec{V}\ or\ \frac{D\{*\}}{Dt} = \frac{\partial \{*\}}{\partial t} + \frac{\partial \{*\}}{\partial x_i} v_i, \tag{6.3}$$

where, $\frac{\partial\{*\}}{\partial t}$ is the local derivative at the spatial point (assuming the fluid is steady); and the term $\frac{\partial\{*\}}{\partial x_i} v_i$ refers to the convective part of the material derivative. The convection

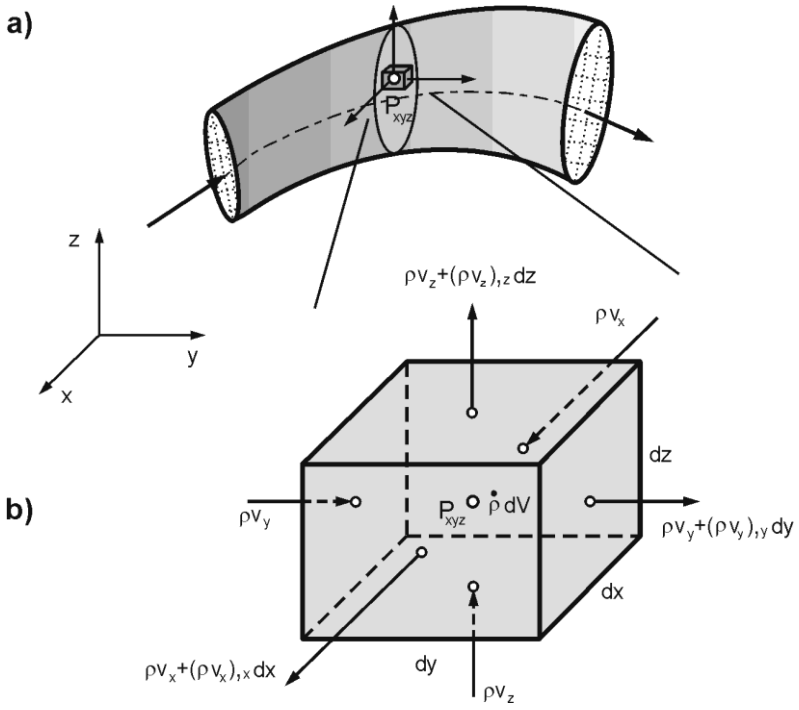

Figure 6.2 a) Control volume within the fluid domain; **b)** Enlarged control volume with mass fluxes through elementary surfaces parallel to stationary coordinate planes, and rate of change of mass within the volume $\dot{\rho}dV$ due to fluid density change.

takes into account the motion of the fluid and in case of incompressible fluid, when $\rho = consant$,

$$\nabla\left(\rho\vec{V}\right) = 0 \; or \; \frac{\partial v_i}{\partial x_i} \equiv \frac{\partial v_x}{\partial x} + \frac{\partial v_y}{\partial y} + \frac{\partial v_z}{\partial z} = 0. \tag{6.4}$$

The above equation shows that the continuity equation for an incompressible fluid exists when the divergence of velocity is equal to zero at each point of the fluid domain.

The acting stresses σ_{ij} on a fluid element can be written as a composition of pressure p and viscous stresses τ_{ij}:

$$\sigma_{ij} = -p\delta_{ij} + \tau_{ij}, \tag{6.5}$$

where, δ_{ij} is the Kronecker delta symbol (δ=1 for $i=j$ & δ =0 for $i \neq j$). As in the solids, it is assumed that the tensile stress is positive. The components of the viscous stress for a Newtonian fluid, are proportional to the strain rates $\dot{e}_{ij}$ defined in (2.1.27),

$$\tau_{ij} = 2\mu\dot{e}_{ij} = \mu\left(v_{i,j} + v_{j,i}\right), \tag{6.6}$$

where, μ is the dynamic viscosity.

The Navier-Stokes equation eq. (5.11) is the governing equation for the fluid flow. However, an analytical solution for this cannot exist since it is a nonlinear partial differential equation, but a few analytical solutions have been found such as Couette flow and Poiseuille Flow (or Hagen – Poiseuille flow). For solving such equations other approaches must be used. Numerical Simulations based on Finite Elements Method are extremely reliable tools to approximate the solution of this problems numerically. To solve a Computational Fluid Dynamics problem we need to determine the three components of the velocity filed $\vec{V} = v_x\hat{\imath} + v_y\hat{\jmath} + v_z\hat{k}$ and the pressure field within the control volume. Thus, four equations are needed. Using conservation principles, the mass and the momentum conservation equations are given by:

- The mass conservation eq. (6.2) is defined as: Rate of the mass change inside the control volume= Inlet Mass Flux – Outgoing Mass Flux and it can be represented analytically in a differential form as:

$$\frac{\partial\rho}{\partial t} + \frac{\partial}{\partial x}(\rho v_x) + \frac{\partial}{\partial y}\left(\rho v_y\right) + \frac{\partial}{\partial z}(\rho v_z) = 0. \tag{6.8}$$

- The momentum conservation of the fluid is derived through Newton's second law of motion $\vec{F} = m\vec{a}$ which leads to N-S eq. (6.7) and can be represented using the stress tensors as:

$$\rho\left(\frac{\partial v_\chi}{\partial t} + v_x\frac{\partial v_\chi}{\partial x} + v_y\frac{\partial v_x}{\partial y} + v_z\frac{\partial v_x}{\partial z}\right) = -\frac{\partial P}{\partial x} - \mu\left(\frac{\partial\tau_{xx}}{\partial x} + \frac{\partial\tau_{xy}}{\partial y} + \frac{\partial\tau_{xz}}{\partial z}\right) + \rho g_x, \tag{6.9}$$

$$\rho\left(\frac{\partial v_y}{\partial t} + v_x\frac{\partial v_y}{\partial x} + v_y\frac{\partial v_y}{\partial y} + v_z\frac{\partial v_y}{\partial z}\right) = -\frac{\partial P}{\partial y} - \mu\left(\frac{\partial\tau_{yx}}{\partial x} + \frac{\partial\tau_{yy}}{\partial y} + \frac{\partial\tau_{yz}}{\partial z}\right) + \rho g_y, \tag{6.10}$$

$$\rho\left(\frac{\partial v_z}{\partial t} + v_x\frac{\partial v_z}{\partial x} + v_y\frac{\partial v_z}{\partial y} + v_z\frac{\partial v_z}{\partial z}\right) = -\frac{\partial P}{\partial z} - \mu\left(\frac{\partial\tau_{zx}}{\partial x} + \frac{\partial\tau_{zy}}{\partial y} + \frac{\partial\tau_{zz}}{\partial z}\right) + \rho g_z. \tag{6.11}$$

In this study, apart from Newtonian fluids, Non-Newtonian fluids are also tested using the Bird-Carreau model:

$$\mu = \mu_\infty + \frac{(\mu_o - \mu_\infty)}{(1+(\lambda\dot{\gamma})^2)^{\frac{1-n}{2}}}, \tag{6.12}$$

where, μ_o: 0,056 (Pa*s), μ_∞: *the value of the Newtonian model*, λ: 3,313 (s), n: 0,3568 and $\dot{\gamma}$ is the shear rate. For a steady state problem as this one, the transient term $\frac{\partial \rho}{\partial t}$ is neglected.

6.2.2 Arbitrary Lagrangian- Eulerian

To describe the FSI analysis, the Arbitrary Lagrangian- Eulerian (ALE) description of the Navier-Stokes equation eq. (6.13) and of the solid domain movement eq. (6.14) can be used [73].

$$\left[M_v\ \widehat{M_v}\right]\left[\frac{\bar{\dot{v}}}{\hat{v}}\right] + \left[K_v \widehat{K_v}\right]\left[\frac{\bar{v}}{\hat{u}}\right] = \overline{R_v} - \overline{F_v}, \tag{6.13}$$

$$M_u \bar{\ddot{u}} + K_u \bar{u} = \overline{R_u} - \overline{F_u}, \tag{6.14}$$

where, M_v and M_u are the mass matrices of the fluid flow and the solid domain respectively, K_v and K_u are the tangent coefficient matrices of both fluid flow and solid domain, $\widehat{M_v}$ and $\widehat{K_v}$ are the mass and coefficient matrices referring to the linearized ALE terms that are coupled with the mesh movement, $\bar{v}$ and $\bar{u}$ are the vectors of the incremental nodal point velocities and displacements respectively, $\hat{\bar{u}}$ is the vector of incremental mesh displacements, $\hat{\bar{v}}$ is the vector of incremental mesh velocities, $\overline{R_v}$ and $\overline{R_u}$ are the vectors of discretized externally applied forces, $\overline{F_v}$ and $\overline{F_u}$ are the vector of knowing terms from the linearization.

In order to perform a FSI simulation the eq. (6.13) and eq. (6.14) have to be coupled in terms of equilibrium and kinematic conditions at the interface [74]. To express the conditions at the fluid-structure interface, eq. (6.15), the superscripts *I*, *F* and *S* are used to denote the fluid-structure interface and the interior fluid and structure degrees of freedom respectively. In our case, no external forces are applied at the interface.

$$\overline{R_u^I} + \overline{R_v^I} = 0, \qquad \overline{u^I} = \hat{\bar{u}}^I, \qquad \dot{\overline{u}}^I = \overline{v^I} = \hat{\bar{v}}^I \ and\ \ddot{\overline{u}}^I = \dot{\overline{v}}^I(t), \tag{6.15}$$

where, $\bar{u}, \bar{\hat{u}}$ and $\bar{\hat{v}}$ are referred to the increments in the nodal displacements, mesh displacements and mesh velocities. The same equations can be satisfied by the total nodal displacements, mesh displacements and mesh velocities.

The movement of the interior mesh nodes, it is described by a function of the of the interface's interior nodes movement. We can assume that the effect of the motion of the mesh is described using the M_v and K_v matrices, while only the interface's degrees of freedom contribute to the mesh motion. After that, the eq. (6.13) can be rewritten as:

$$\begin{bmatrix} M_v^{II} & M_v^{IF} \\ M_v^{FI} & M_v^{FF} \end{bmatrix} \begin{bmatrix} \dot{\overline{v^I}} \\ \dot{\overline{v^F}} \end{bmatrix} + \begin{bmatrix} K_v^{II} + \widehat{M}_v^{II} & M_v^{IF} \\ K_v^{FI} + \widehat{M}_v^{FI} & M_v^{FF} \end{bmatrix} \begin{bmatrix} \overline{v^I} \\ \overline{v^F} \end{bmatrix} + \begin{bmatrix} \widehat{K}_v^{II} & 0 \\ \widehat{K}_v^{FI} & 0 \end{bmatrix} \begin{bmatrix} \overline{u^I} \\ \overline{u^F} \end{bmatrix} = \begin{bmatrix} \overline{R_v^I} \\ \overline{R_v^F} \end{bmatrix} - \begin{bmatrix} \overline{F_v^I} \\ \overline{F_v^F} \end{bmatrix}, \quad (6.16)$$

where, $\overline{u^F}$ indicates the vectors of the internal fluid particle displacements which in this case are not calculated [74]. Combining the eq. (6.14), (6.16) and the first equation from eq. (6.15) the coupled FSI equations are [74]:

$$A\ddot{\overline{U}} + B\dot{\overline{U}} + C\overline{U} = \bar{G} \ , \quad (6.17)$$

where,

$$A = \begin{bmatrix} M_u^{SS} & M_u^{SI} & 0 \\ M_u^{IS} & M_u^{II} + M_v^{II} & M_v^{IF} \\ 0 & M_v^{FI} & M_v^{FF} \end{bmatrix}, \quad (6.18)$$

$$B = \begin{bmatrix} 0 & 0 & 0 \\ 0 & K_v^{II} + \widehat{M}_v^{II} & K_v^{IF} \\ 0 & K_v^{FI} + \widehat{M}_v^{FI} & K_v^{FF} \end{bmatrix}, \quad (6.19)$$

$$C = \begin{bmatrix} K_u^{SS} & K_u^{SI} & 0 \\ K_u^{IS} & K_u^{II} + \widehat{K}_v^{II} & 0 \\ 0 & \widehat{K}_v^{FI} & 0 \end{bmatrix}, \quad (6.20)$$

$$\bar{G} = \begin{bmatrix} \overline{R_u^S} \\ 0 \\ \overline{R_u^F} \end{bmatrix} - \begin{bmatrix} \bar{F}_u^S \\ \bar{F}_u^I + \bar{F}_v^I \\ \bar{F}_v^F \end{bmatrix} \ and \ \ \overline{U} = \begin{bmatrix} \overline{u^S} \\ \overline{u^I} \\ \overline{u^F} \end{bmatrix}. \quad (6.21)$$

To solve the eq. (6.17) it is necessary the time derivatives to be discretized. Thus the coupled finite element eq. (6.17) is given by [74]:

$$\begin{bmatrix} \widetilde{K_u}^{SS} & \widetilde{K_u}^{SI} & 0 \\ \widetilde{K_u}^{IS} & \widetilde{K_u}^{II} + \widetilde{K_v}^{II} & \widetilde{K_v}^{IF} \\ 0 & \widetilde{K_v}^{FI} & \widetilde{K_v}^{FF} \end{bmatrix} \begin{bmatrix} \overline{U}^S \\ \overline{U}^I \\ \overline{U}^F \end{bmatrix} = \begin{bmatrix} \overline{R_u}^S \\ 0 \\ \overline{R_v}^F \end{bmatrix} - \begin{bmatrix} \bar{\bar{F}}_u^S \\ \bar{\bar{F}}_u^I + \bar{\bar{F}}_v^I \\ \bar{\bar{F}}_v^F \end{bmatrix}, \tag{1.29}$$

where, $\widetilde{K}$, indicates the linearized coefficient matrix, $\overline{U}$, is the nodal point displacements/velocities vectors, $\bar{R}$, is the discretized external forces vector, $\tilde{F}$ is the vector that contains the known terms from the linearization and time discretization. The terms $\overline{U}^S, \overline{U}^F$ and $\overline{U}^I$ contain the displacements, the velocities and in general either velocities or displacements (displacements are the most preferable) [74].

CHAPTER 7. NUMERICAL SOLUTION

7.1 Simulations and Results

In this part, the CFD and FSI results will be presented. Starting with the CFD simulations, the Reynolds' Number, R_e, the entrance length, l_e (when the fluid flows inside the bigger channels), the velocity, the pressure drop, the wall shear stress will be calculated for each fluid case and the velocity profile in YZ and YX planes will be determined. After the CFD, the results of the FSI will be presented. The cantilever's deflection along the y-axis, the von Mises equivalent stress and a comparison between one and two way FSI will be presented.

CFD Results

In order to perform any FEM analysis, the Boundary Conditions (BC) of the problem must be set (Figure 7.1). Table 7.1 shows the BC for the CFD simulations. The simulations were performed using laminar flow and no thermal phenomena were included. The gravitational forces were also taken into consideration. For the Convergence Control, the maximum iterations was set 100 for the Newtonian and for the Nom-Newtonian 120. The timescale control was set to Auto and the Length Scale Option to Conservative with timescale factor equal to 1. The Convergence Criteria set to be RMS with Residual Target $1x10^{-10}$ (Figure 7.2). Furthermore, several monitoring points were placed inside the microchannel to keep track of the values of the pressure and velocity, in order to ensure that the variables under study reach a constant number (Figure 7.3).

Table 7.1 CFD Boundary Conditions

Boundary Conditions	Values
Inlet Velocity	0.1 mm/s *(Same at all the inlet's nodes)*
Outlet Pressure	0 Pa *(Same at all the inlet's nodes)*
Wall	No Slip / No penetration *(meaning that the fluid has zero velocity relative to the wall)*

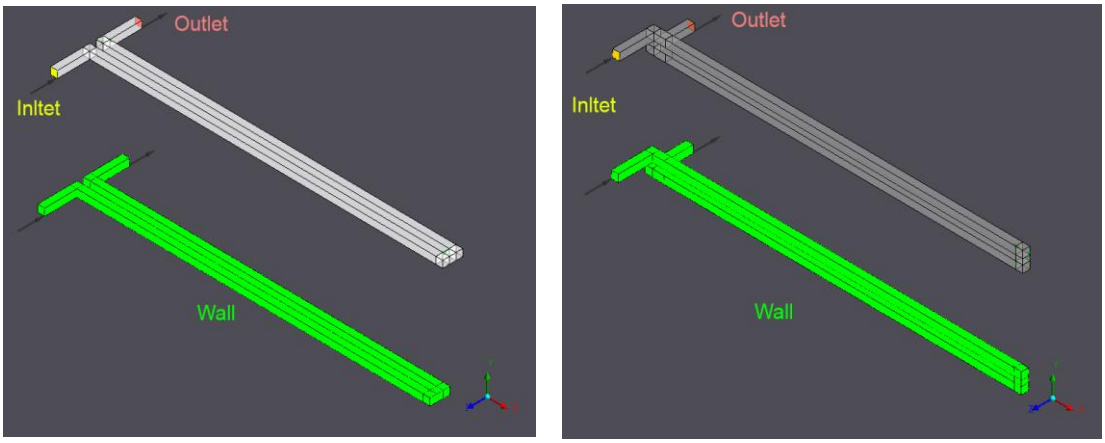

Figure 7.1 The boundary conditions of the (left) F1 channel and (right) F2 channel.

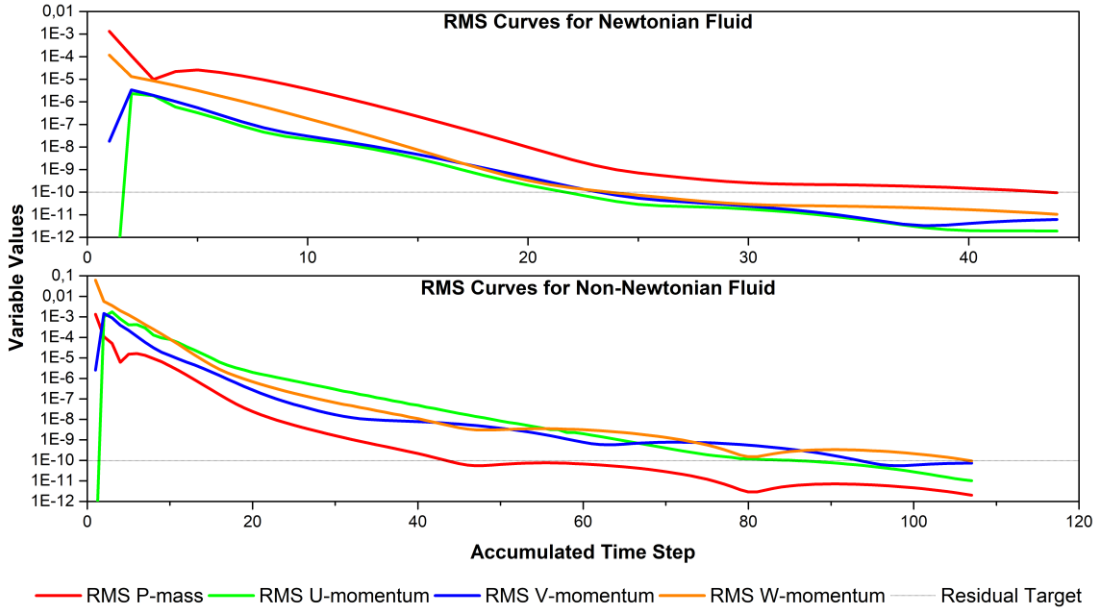

Figure 7.2 The RMS curves reached the Residual Target for a Newtonian (top) and for a Non-Newtonian (bottom) fluid.

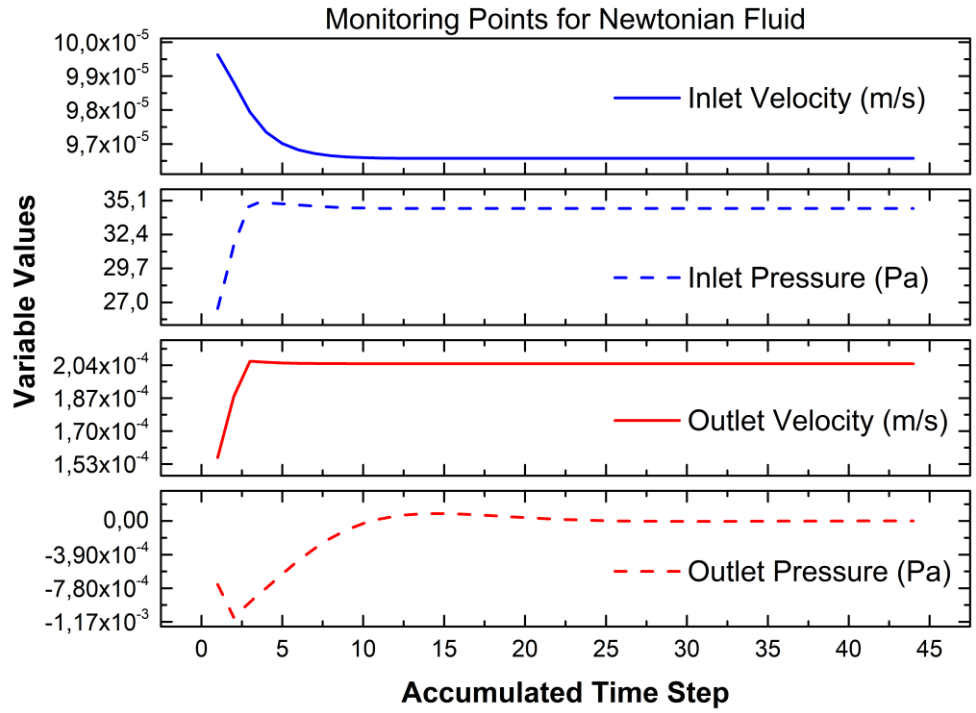

(A)

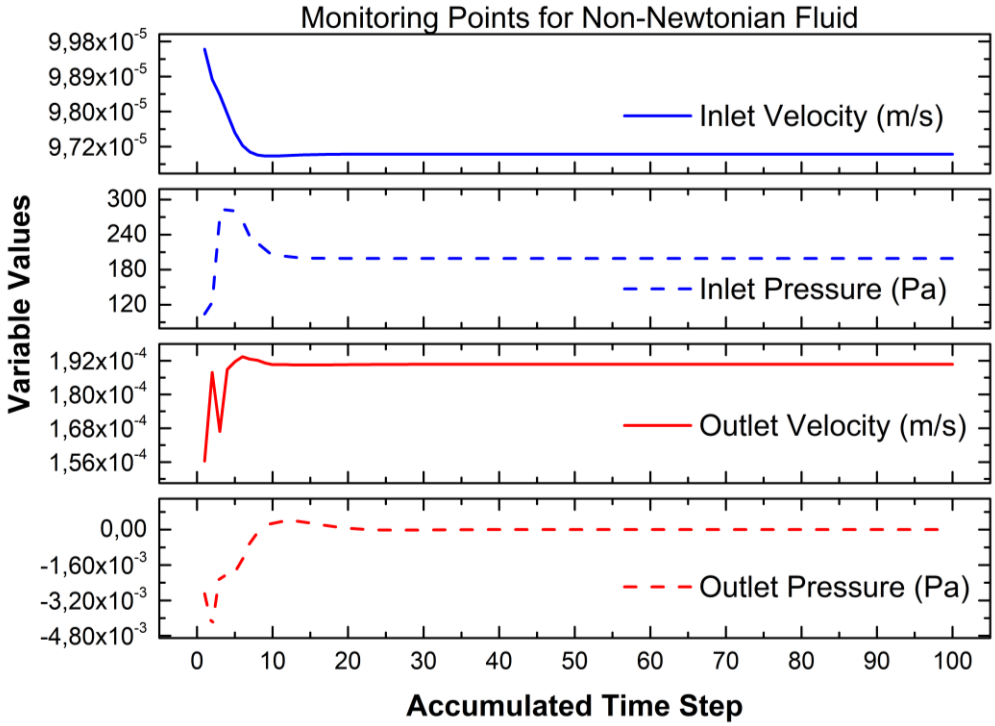

(B)

Figure 7.3 The Pressure and Velocity values monitoring at the inlet and outlet of the microchannel. The variables get a constant value after several iterations. The top picture (A) corresponds to a Newtonian fluid while the bottom picture (B) to a Non-Newtonian fluid

After that, the Reynolds Number, R_e, the entrance length, l_e (when the fluid flows inside the bigger channels), the velocity, the pressure drop, the wall shear stress will be calculated in each fluid case and the velocity profile in YZ and YX planes were determined for the channel F1.

Reynolds Number

The Reynolds Number was calculated using a CEL (CFX Expression Language) to calculate the Reynolds' Number inside the microchannel. Table 7.2 presents the Reynolds Numbers of each fluid.

Table 7.2 Reynolds Number

Fluids	Reynolds Number
Blood*	$2.4\text{x}10^{-4}$ ~ $4.80\text{x}10^{-4}$
Water	$8.96\text{x}10^{-4}$ ~ $1.79\text{x}10^{-3}$
Acetone	$1.98\text{x}10^{-3}$ ~ $3.97\text{x}10^{-3}$
Propanol	$3.35\text{x}10^{-4}$ ~ $6.69\text{x}10^{-4}$
Acetic Acid	$7.30\text{x}10^{-3}$ ~ $1.46\text{x}10^{-3}$
Blood 35%H**	$1.94\text{x}10^{-4}$ ~ $2.45\ \text{x}10^{-4}$
Blood 40%H**	$1.80\text{x}10^{-4}$ ~ $2.29\text{x}10^{-4}$
Blood 48%H**	$1.39\text{x}10^{-4}$ ~ $1.91\text{x}10^{-4}$

The (Figure 7.4) shows how the Reynolds Number varies horizontally in the middle of a YZ plane for a Newtonian and Non-Newtonian fluid.

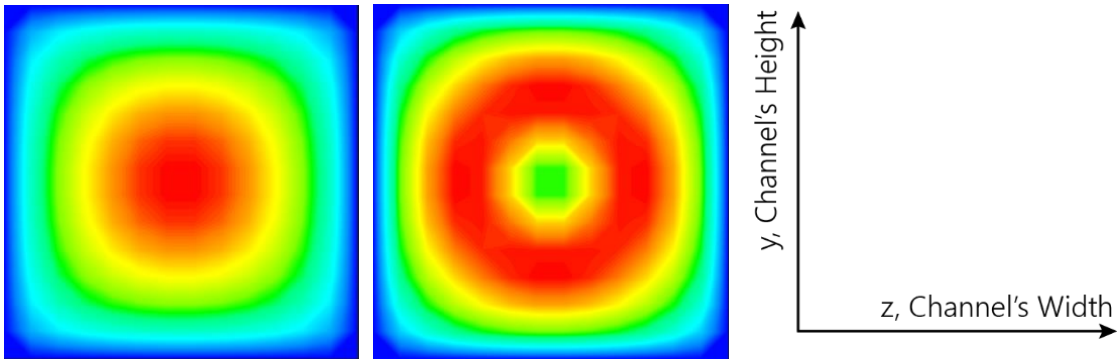

(A) (B)

Figure 7.4 Reynolds' Number variation for a (A) Newtonian and (B) Non-Newtonian fluid across the YZ-plain.

For the Non-Newtonian fluids, the Reynolds Number was calculated using the Bird Carreau model for determining the dynamic viscosity. Due to the non-linearly changes on the share rate, the Reynolds Number changes non-linearly as well. In the graph bellow (Figure 7.5) a comparison between Newtonian and Non-Newtonian variation of the Reynolds Number is presented.

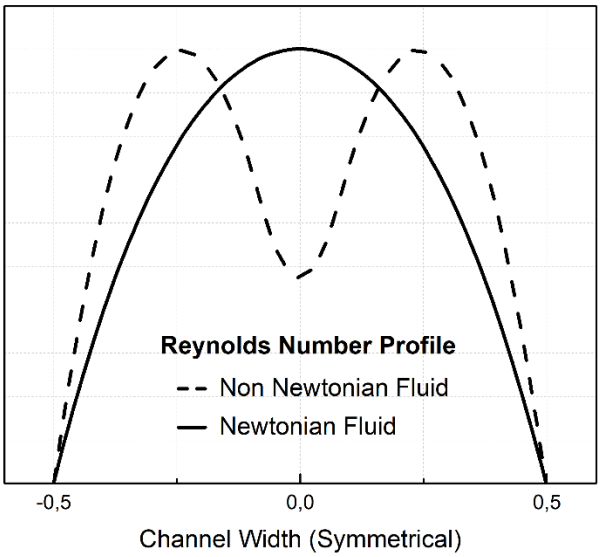

Figure 7.5 Comparison between Newtonian and Non-Newtonian variation of the Reynolds' Number.

Table 7.3 shows the length required for the fluid flow to reach its developed profile. As it was expected the fluid flow is developed approximately after one or two hydraulic diameters, D_h. This means that the velocity along the x-axis reaches a constant value after a specific point (Figure 7.6).

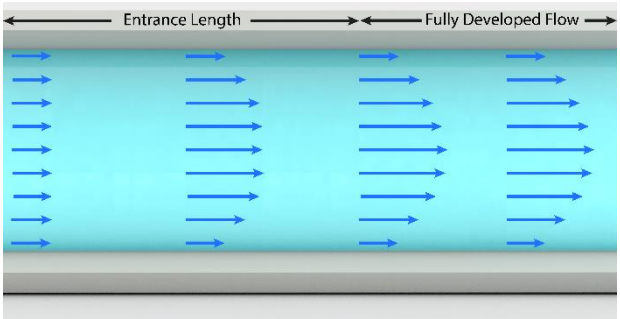

(A)

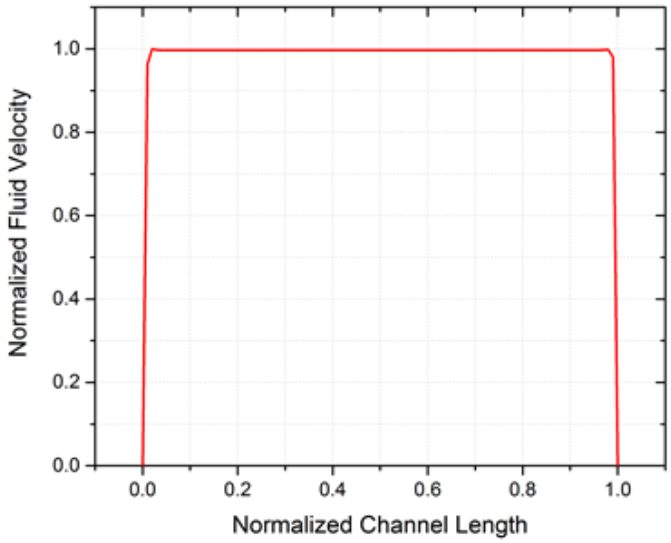

(B)

Figure 7.6 (A) The flow as it becomes fully developed inside a microchannel. (B) Normalized plot for the entrance length. The fluid enters from one side and exits from the other.

Table 7.3 Entrance Length

Fluids	Entrance Length (μm)
Blood*	12.7
Water	32.95
Acetone	21.2
Propanol	12.7
Acetic Acid	12.7
Blood 35%H**	16.9
Blood 40%H**	16.9
Blood 48%H**	21.2

Fluid Flow

The velocity streamlines, the wall pressure and the wall shear stress contours of the fluids used, are quite similar. Although, their wall pressure and wall shear stress numerical values are slightly different. In (Figure 7.7), the aforementioned quantities are presented for the case of the water. Table 7.4 shows the numerical values of the wall pressure and the shear wall among the fluids.

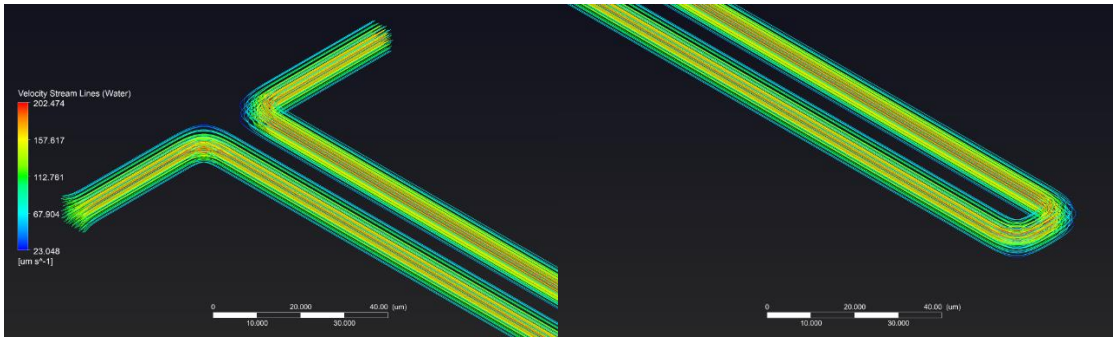

Water Velocity Stream Lines: $23.048 \leq u\ (\frac{\mu m}{s}) \leq 202.474$

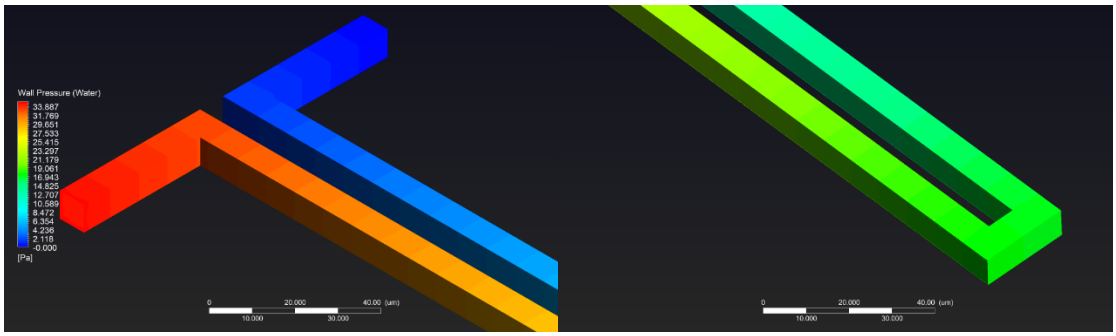

Water Wall Pressure: $0.00 \leq P\ (\text{Pa}) \leq 33.887$

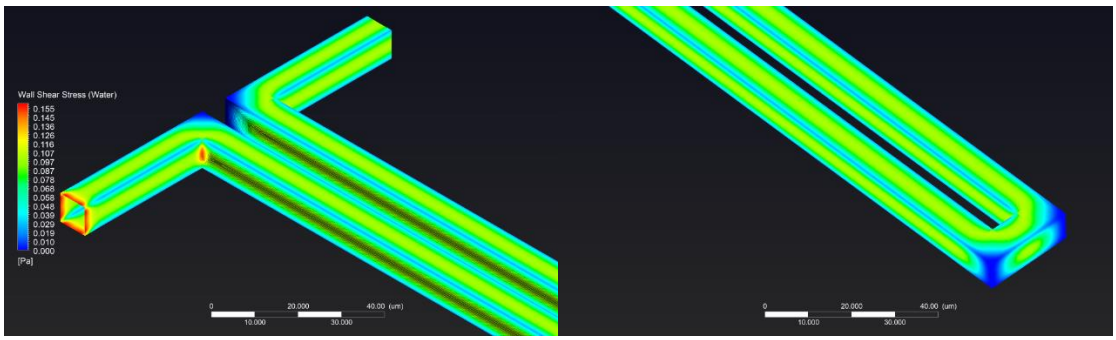

Water Wall Shear Stress Contours: $0.00 \leq \tau_w\ (Pa) \leq 0.155$

Figure 7.7 The velocity streamlines, the wall pressure and the wall shear stress contours of the water.

Table 7.4 The numerical values of the wall pressure and the shear wall among the fluids.

Fluids	Wall Pressure (Pa)	Wall Shear Stress (Pa)
Blood*	0.00 ~ 133.127	0.00 ~ 0.609
Water	0.00 ~ 33.887	0.00 ~ 0.155
Acetone	0.00 ~ 12.001	0.00 ~ 0.550
Propanol	0.00 ~ 73.018	0.00 ~ 0.155
Acetic Acid	0.00 ~ 43.771	0.00 ~ 0.200
Blood 35%H**	0.00 ~ 195.799	0.00 ~ 0.897
Blood 40%H**	0.00 ~ 210.860	0.00 ~ 0.962
Blood 48%H**	0.00 ~ 270.030	0.00 ~ 1.229

Moving forward, the normalized velocity profiles of the fluids alongside the channel's width and height, as well as, the velocity profile contour, are presented in (Figure 7.8). The velocity profiles are referred to a position after the entrance length of the fluids.

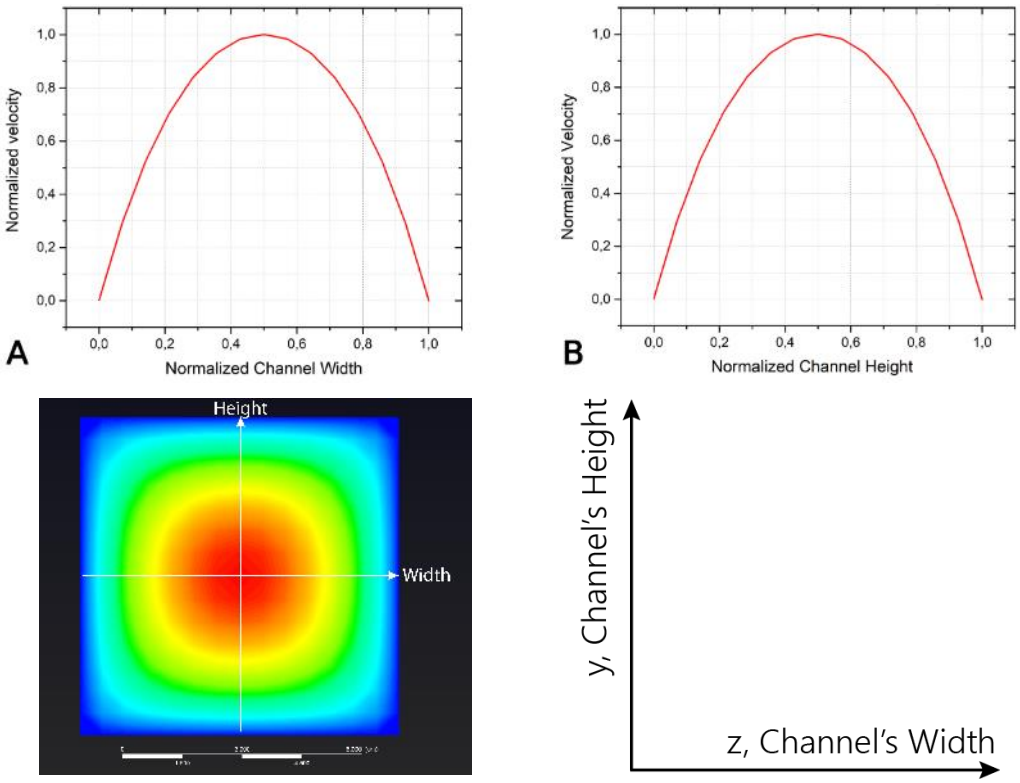

Figure 7.8 (Up) The velocity profiles of the fluids alongside the (A) channel's width and (B) channel's height. The velocity contour (Down).

The velocity profiles seem to have a parabolic profile after the fluids reached their fully developed phase. The difference between the Newtonian and Non-Newtonian fluid velocity profile is shown in (Figure 7.9).

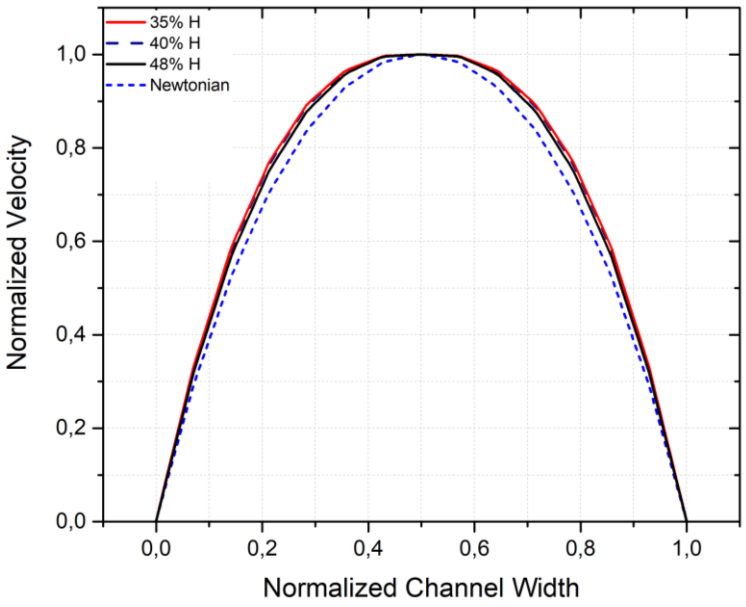

Figure 7.9 The normalized velocity profile of the Newtonian and Non-Newtonian fluids.

Furthermore, the normalized pressure drop inside the microfluidic channel is shown in the (Figure 7.10). The pressure drop values of the different fluids are presented in the Table 7.5.

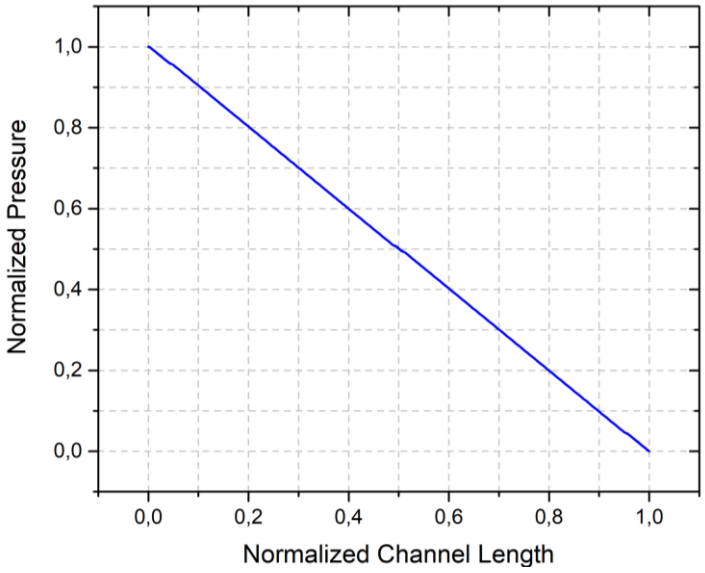

Figure 7.10 The normalized pressure drop inside the microchannel.

Table 7.5 The Pressure Drop values.

Fluids	Pressure Drop (Pa)
Blood*	135.618
Water	34.473
Acetone	12.243
Propanol	74.396
Acetic Acid	44.774
Blood 35%H**	200.212
Blood 40%H**	215.239
Blood 48%H**	276.132

The pressure drop of the Newtonian fluids is presented in (Figure 7.11), while the pressure drop for the Non-Newtonian fluids is shown in (Figure 7.12). The pressure drop increases proportionally to the dynamic viscosity.

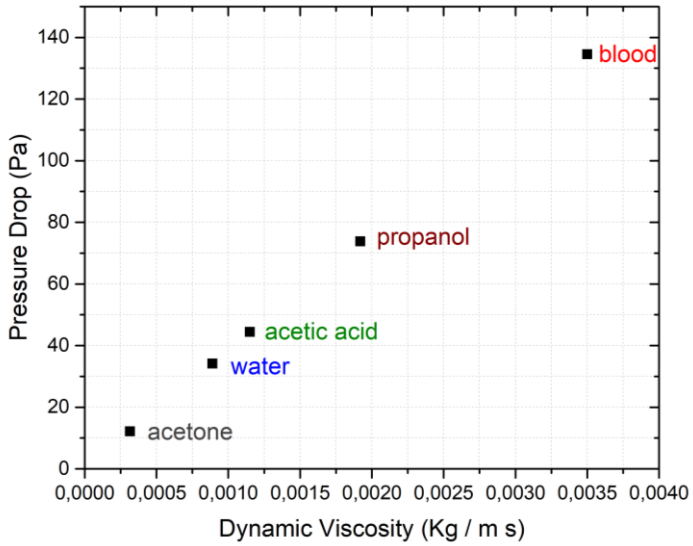

Figure 7.11 The pressure drop of the Newtonian Fluids.

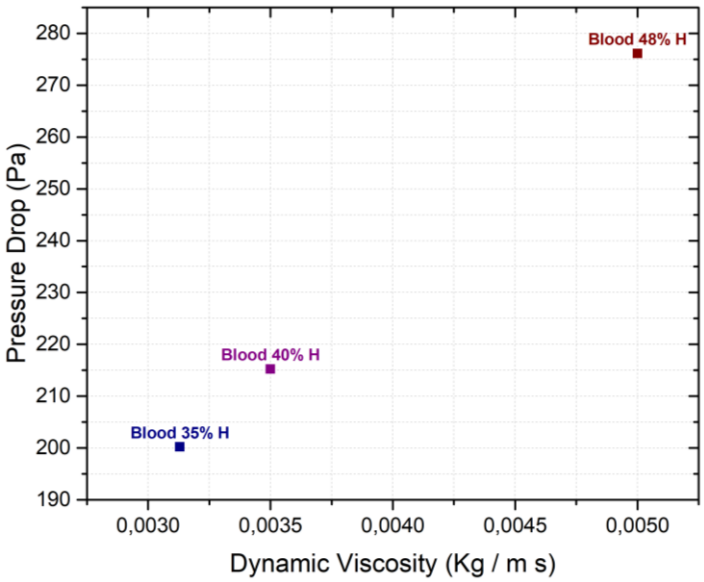

Figure 7.12 The pressure drop of the Non-Newtonian Fluids.

The F2 channel

The F2 channel was tested using water as the main fluid. The velocity streamlines, the pressure drop and the wall shear contours are presented in (Figure 7.13). The entrance length of the fluid is 17.13 μm, (Figure 7.14). The velocity profiles at the middle of the upper longer channel (YX plane) and at the middle of the nozzle (ZX plane), are presented in (Figure 7.15). The velocity profiles have a parabolic shape. The velocity value at the nozzle is slightly higher in comparison to the one in the upper longer channel. Finally, the Pressure Drop alongside the microchannel was found to be 34.144 Pa. Quite similar to the F1 case.

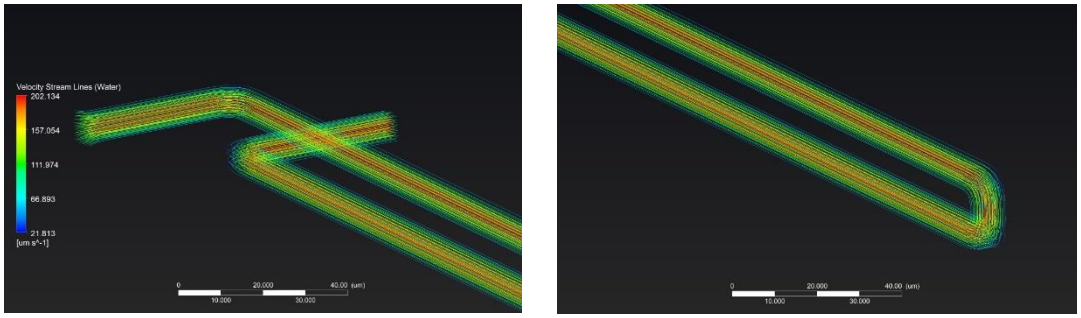

Water Stream Lines: $21.813 \leq u\ (\frac{\mu m}{s}) \leq 202.134$

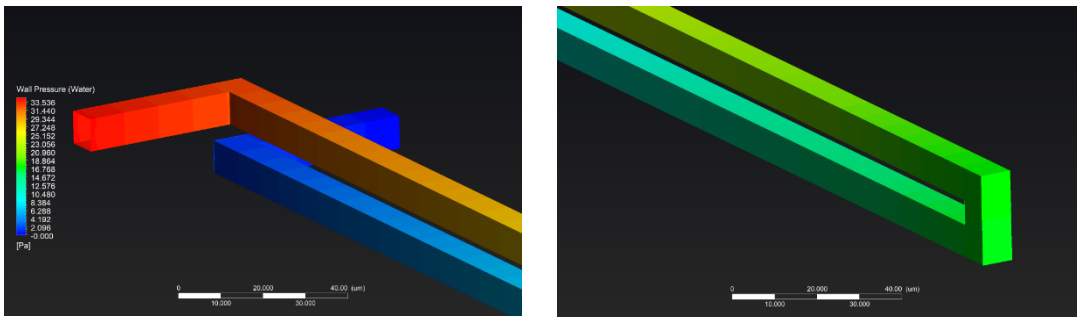

Water Wall Pressure: $0.00 \leq P\ (\text{Pa}) \leq 33.536$

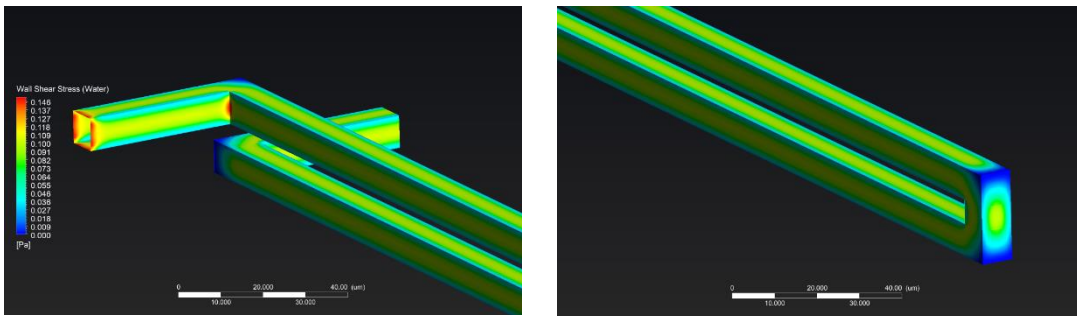

Water Wall Shear Stress Contours: $0 \leq \tau_w\ (Pa) \leq 0.146$

Figure 7.13 The velocity streamlines, the wall pressure and the wall shear stress contours of the water for the F2 geometry.

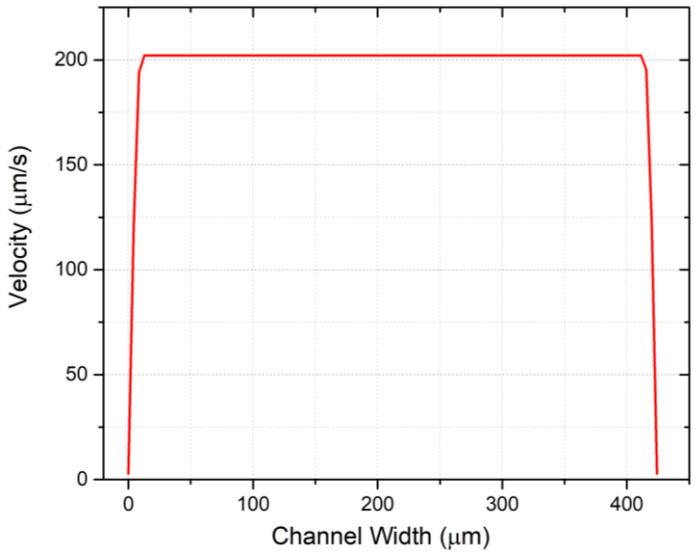

Figure 7.14 The entrance length of the fluid in the F2 geometry at the upper long channel. The fluid enters the channel (from the right side) and exits after 420 μm (left side).

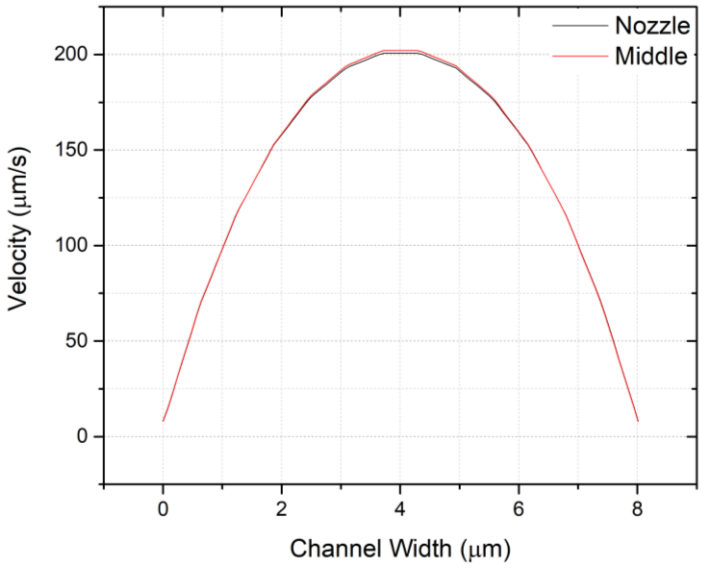

Figure 7.15 The velocity profiles at the middle of the upper longer channel and at the nozzle.

The velocity contours of the F2 geometry are shown in (Figure 7.16) while, the velocity contours at the nozzle region are shown in (Figure 7.17)

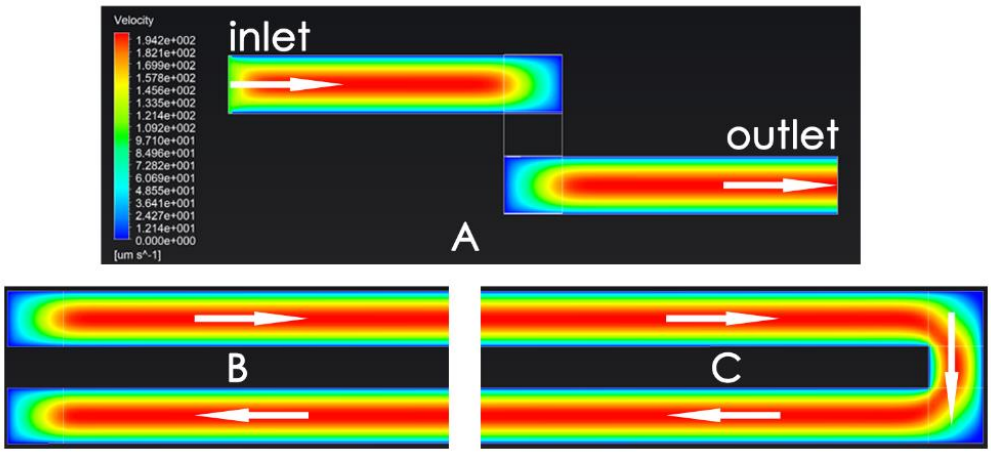

Figure 7.16 The velocity contour alongside the microchannel (A) front view (B) side view.

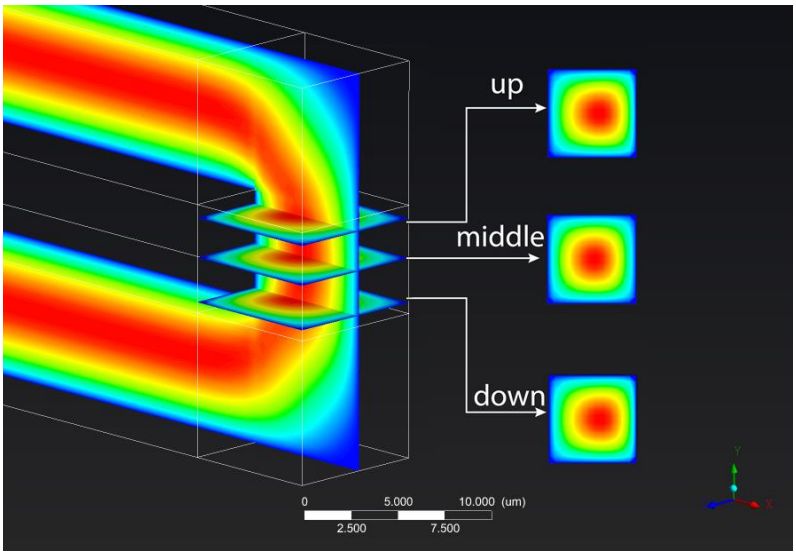

Figure 7.17 Velocity contours alongside the YX plane and ZX plane at the nozzle region.

FSI Results

After the CFD simulations, the generated loads from each fluid flow case were transferred to the Mechanical Analysis in order to perform the FSI. One and two way FSI simulations were compared. As mentioned above, two biosensor geometries were tested. Biosensor B1 and Biosensor B2 were used in order to examine which biosensor would give the maximum tip deflection. Both biosensor geometries were tested as if they were fabricated with PDMS. After the geometry evaluation, PMMA was tested as

an alternative material. Moreover, three different lengths for the microcantilever were simulated to test their maximum deflection. Moving forward, the tip's maximum deflection and the von Mises equivalent stress were calculated. A correlation between the fluids' velocity, the fluids' dynamic viscosity and the maximum deflection of the microcantilever's tip were performed. Last but not least, the FSI results were used to predict the maximum tip deflection for a fluid. Then, the predicted value was compared to the FEM result.

One and two way FSI comparison

As mentioned above, when the CFD results influence the mechanical analysis (and vice versa) but the structural reaction has minor impact on the fluid flow, then the FSI simulation is categorized as *one-way*. On the other hand, when the fluid flow affects the structural analysis and the outcome of the mechanical simulation affects the fluid flow, then the FSI is considered to be *two-way* (Figure 7.18).

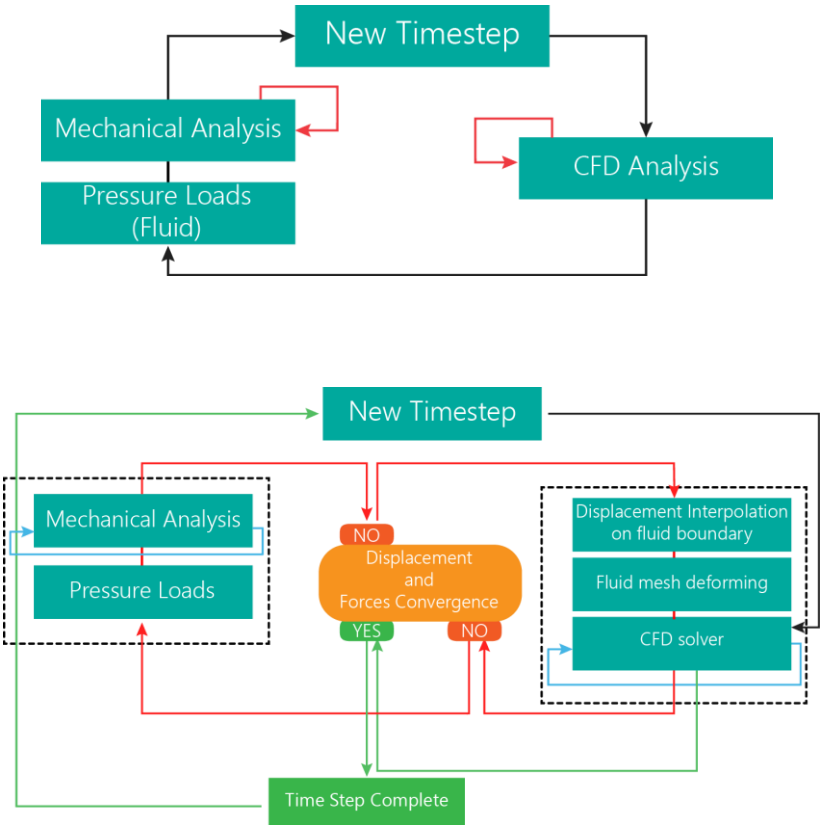

Figure 7.18 (Above) One way and (Bellow) Two Way FSI.

Due to the geometries' complexity, only the B1 biosensor design was tested. To compare the FSI results, the B1 biosensor was simplified. Because the two way FSI simulation is extremely time and computationally memory consuming, the geometry simplification was mandatory. For simplification purposes, only the cantilever tip was taken into account. The final geometry is shown in (Figure 7.19). The mesh options are remained constant as before.

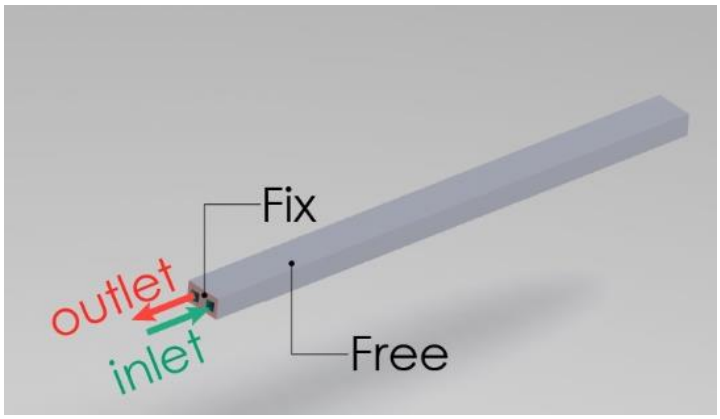

Figure 7.19 The simplified B1 geometry for the one and two way FSI analysis.

The boundary conditions for the fluid domain were set as following: Inlet: 0,1 mm/s, Outlet: 0 Pa and Wall: no slip / no penetration. For the solid domain, the back free end of the tip was set as fixed, while the rest of the geometry was left to be free to move up and down. The earth's gravity was also taken into account. The results of the one and the two way FSI are presented in (Figure 7.20).

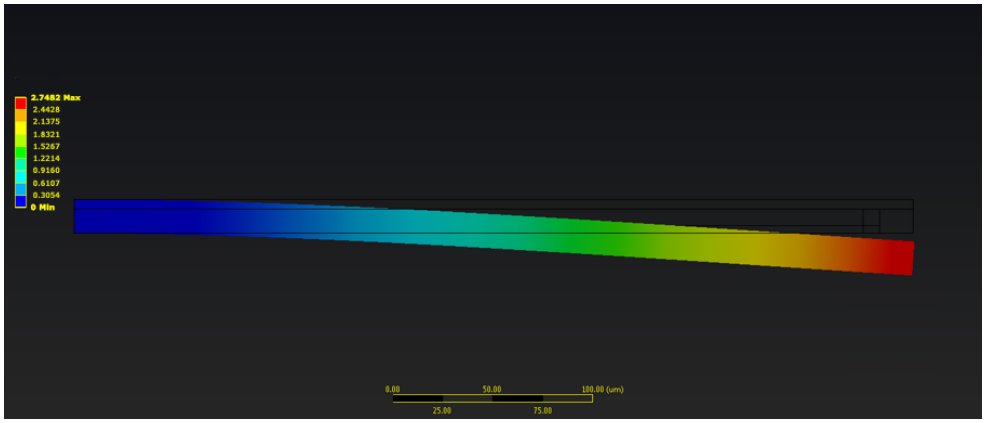

(A)

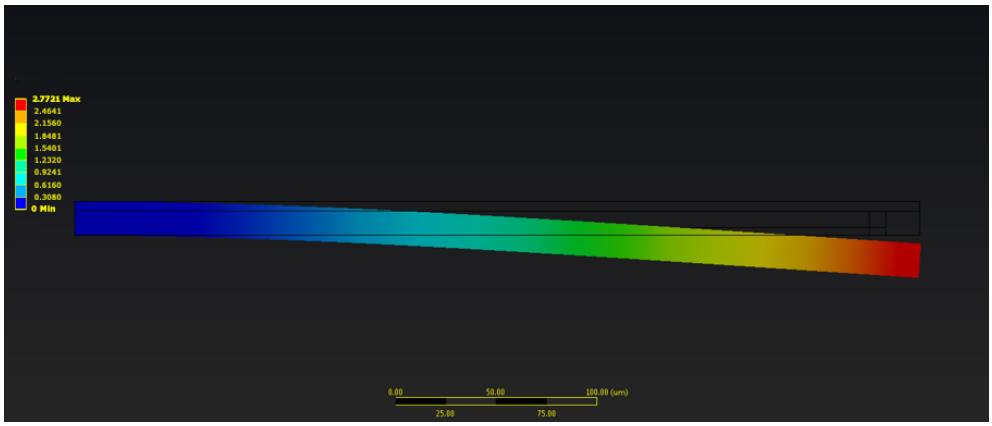

(B)

Figure 7.20 Maximum tip deflection by employing (A) One and (B) Two way FSI analysis. The undeformed structure is shown with the black outline.

The maximum tip deflection from the one and the two way FSI analysis are quite close, 2.7482 and 2.7721 μm, respectively. Thus, for time and computationally memory consumption, the one way FSI simulation was used over the two way.

Geometry test

Two geometries have been designed B1 (Rectangular) and B2 (Nozzle). The boundary conditions of the fluid and the solid domain remain the same as above. The geometry that can be deflected the most has better detection sensitivity. As it is shown in (Figure 7.21), the geometry B1 deflects the most, 5.53402 μm and thus it is the most sensitive design while the B2 geometry bends only 0.93493μm. The fluid enters the channel with 0.1 mm/s.

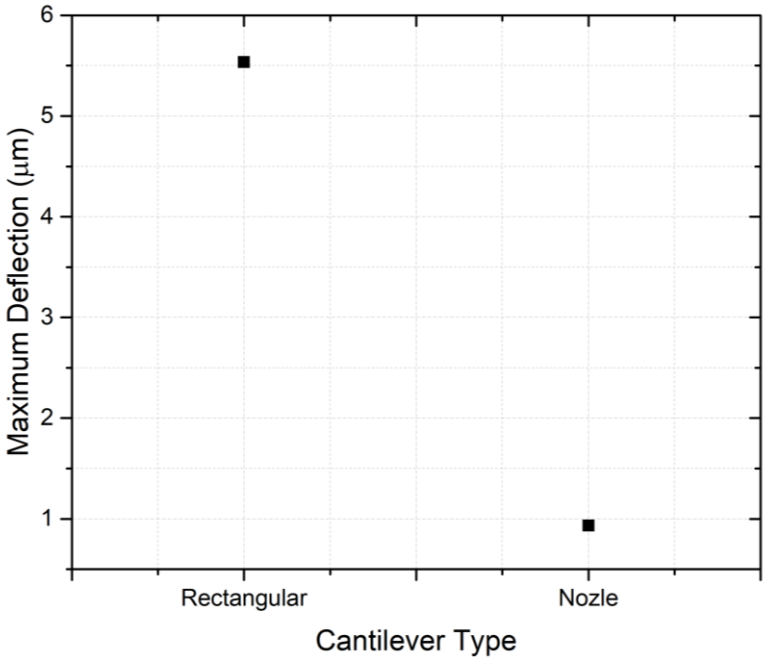

Figure 7.21 The maximum deflection between the two tested geometries.

Material Test

Since the most sensitive design for the biosensor, was found to be the B1 geometry, PMMA was selected as an alternative material for the biosensor's fabrication. The maximum tip deflection for both materials (PDMS and PMMA) is presented in (Figure 7.22). PDMS was found to be the best option with a deflection value of 5.3385 μm against the PMMA which deflects 0.00122 μm.

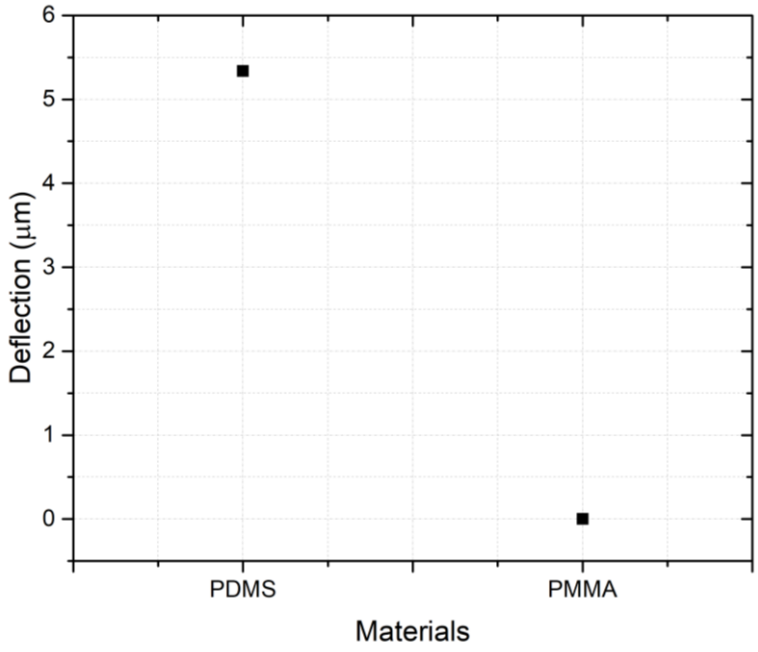

Figure 7.22 Maximum tip deflection for the PDMS and PMMA

Length Test

Three different lengths for the biosensor's tip were designed, 280, 420 and 630μm, while the remaining dimensions were kept the same (thickness 17μm and width 30μm). Moreover, the meshing properties were the same in all cases and the mesh statistics of each biosensor are presented in (Table 7.6). The fluid flow remains the same. As the length of the tip increases, the biosensor becomes more sensitive. The drawbacks are that we cannot fabricate as long tip as we want without jeopardizing the sustainability of the structure. Moreover, a bigger geometry requires more nodes and more computational power to employ FEM. Thus, the geometry with the 420μm tip length, was chosen (Figure 7.23)

Table 7.6 Meshing properties for the three biosensor cases

Cases	Tip Length (μm)	Nodes Number	Elements Number	Deflection (μm)
1	280	1051474	966972	0.68032
2	420	1533645	1336553	5.53402
3	630	1992314	6499618	13.85034

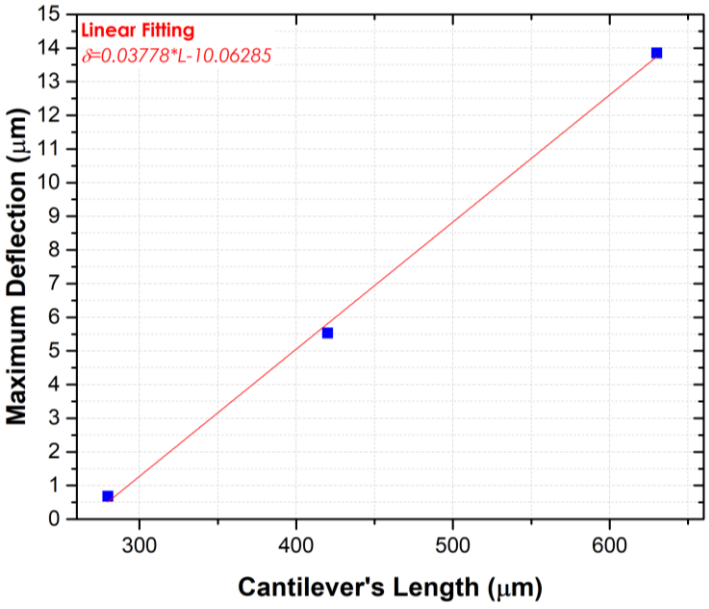

Figure 7.23 Maximum deflection Vs the cantilever's length

The maximum deflection of the cantilever tip increases linearly as the length of the tip increases. Eq. (7.1) shows the linear relationship between the deflection, δ and the length, L of the tip.

$$\delta = 0.03778 \cdot L - 10.06285 \,. \tag{7.1}$$

Deflection Vs fluid velocity and fluid viscosity

In order to prove that the biosensor responses differently when different fluid velocities are applied, we tested the deflection of the microcantilever using different velocity values. Firstly, a velocity value of 0 mm/s was applied. That means that the fluid enters the microchannel and remains there without moving. Secondly, 0.1 mm/s was set as initial value and finally 1 mm/s was chosen to complete the test. As it was expected the microcantilever deflects more when the fluid velocity increases and follows a linear behavior (Figure 7.24). The deflection values in each case are shown in the (Table 7.7). The eq. (7.2) shows the linear relationship between the fluid's initial velocity, u_{fluid} and the tip's deflection.

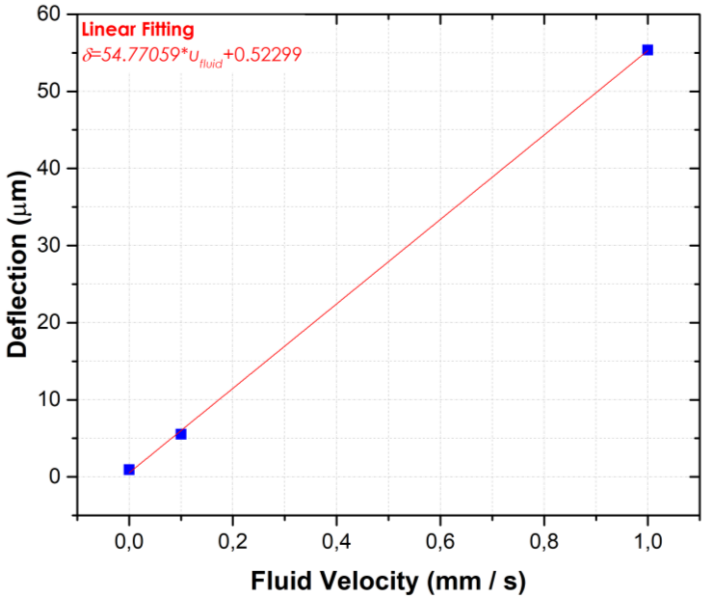

Figure 7.24 Deflection of the microcantilever's tip due to the different fluid velocities.

$$\delta = 54.77059 \cdot u_{fluid} + 0.52299 \,. \tag{7.2}$$

Table 7.7 Maximum tip deflection using different fluid velocities.

Cases	Velocity (mm/s)	Deflection (μm)
1	0	0.94243
2	0.1	5.53402
3	1	55.34019

Figure 7.25 shows the deflection of the tip using different fluids. The relationship between the fluids' dynamic viscosity and the biosensor's tip deflection, is linear and increases proportionally. We tested four materials (acetone, water, acetic acid, propanol and blood) to evaluate the aforementioned behavior of the microcantilever. Two different velocities were tested, 0.1 and 1 mm/s, and as before, the deflection of the fluids increase proportionally to the constant velocity by ten times. Table 7.8 shows the deflection values of each fluid in 0.1 and 1 mm/s initial velocity.

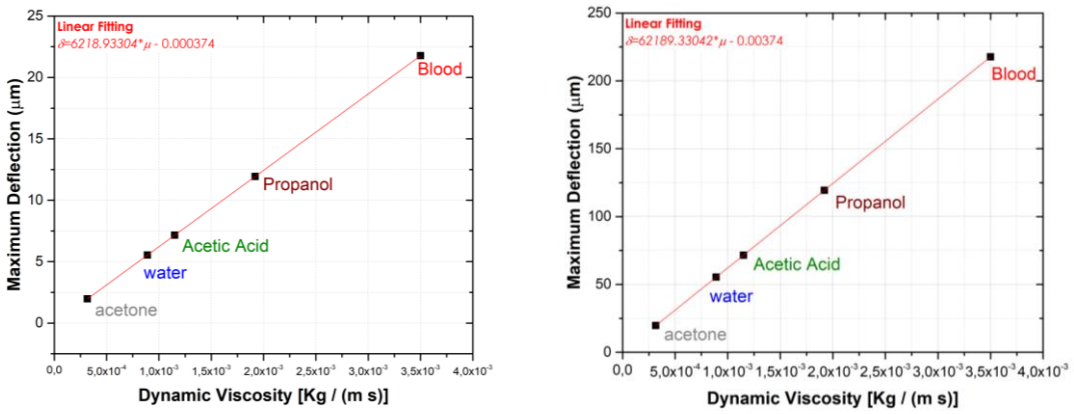

Figure 7.25 The maximum deflection of the fluids using (Left) 0.1 mm/s and (Right) 1 mm/s fluid velocity.

Eq. (7.3) describes the deflection of the microcantilever when the fluid velocity is 0.1 mm/s. On the other hand, the eq. (7.4) describes the deflection when the velocity of the fluid is 1 mm/s.

$$\delta = 6218.93304 \cdot \mu + 0.000374\,, \tag{7.3}$$

$$\delta = 62189.33042 \cdot \mu + 0.00374\,, \tag{7.4}$$

where, μ is the dynamic viscosity.

Table 7.8 Maximum tip deflection using different fluids and velocities.

Fluids	0.1 mm/s	1 mm/s
	Deflection (μm)	
Acetone	1.96513	19.6513
Water	5.53402	55.3402
Acetic Acid	7.15157	71.5157
Propanol	11.93984	119.3984
Blood*	21.76601	217.6601

However, this method can be extended to the Non-Newtonian fluids as they follow the same linear distribution. (Figure 7.26) shows the tip's deflection of the blood as a Non-Newtonian fluid when the fluid velocity is 0.1 mm/s.

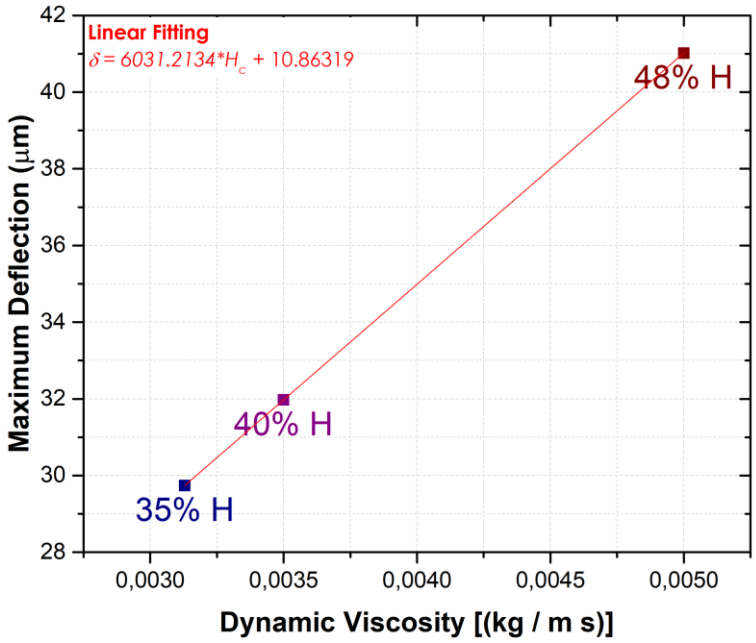

Figure 7.26 Maximum tip's deflection of a Non-Newtonian fluids with 0.1 inlet velocity.

The deflection of the tip for a Non-Newtonian fluid, due to the Hematocrit changes, H_c, is given from the eq. (7.5)

$$\delta = 6031.2134 \cdot H_c + 10.86319 \, . \tag{7.5}$$

In (Figure 7.27) the maximum tip's deflections of the Newtonian and Non-Newtonian fluids are presented. Both fluid cases follow a linear distribution.

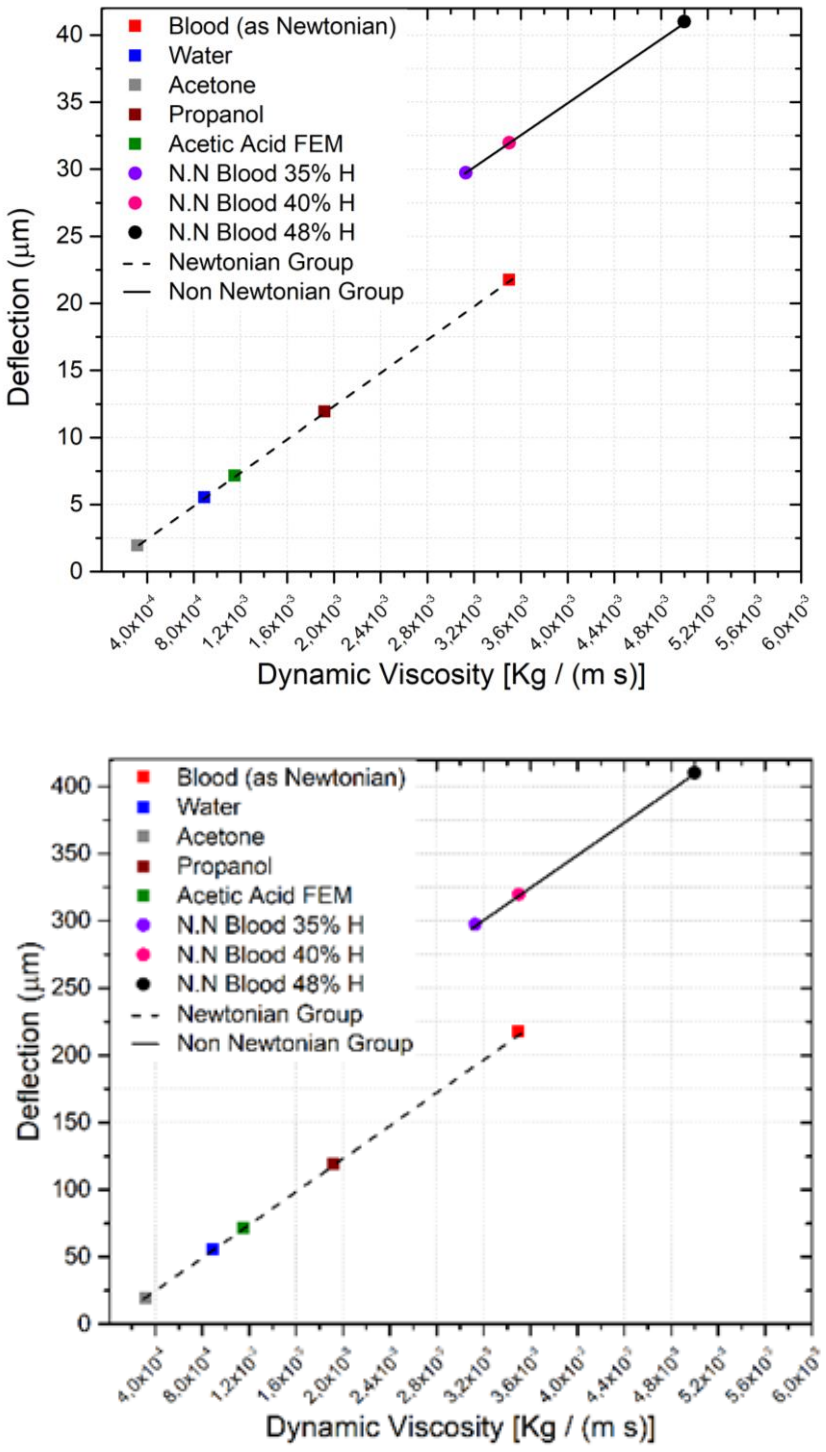

Figure 7.27 Maximum tip's deflection of Newtonian and Non-Newtonian fluids. (top) 0.1 mm/s (bottom) 1 mm/s.

Deflection and von Mises stress

The deflection of the biosensor's tip as well as the von Mises stress were calculated on the surface of the microcantilever's tip by creating a path between two middle points as the (Figure 7.28) shows.

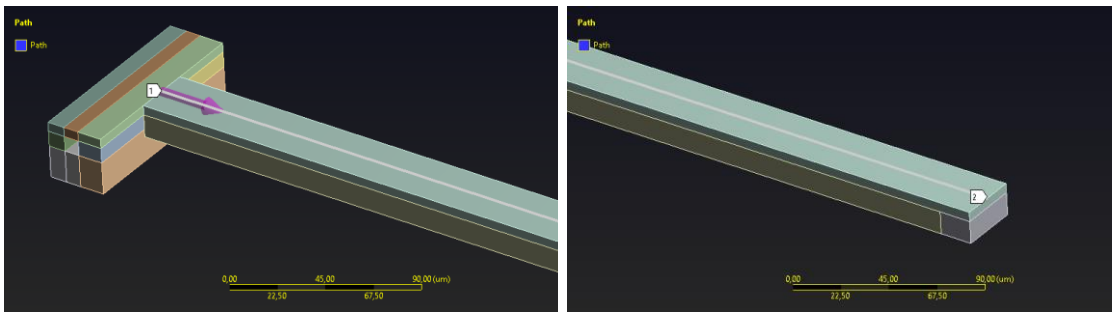

Figure 7.28 The path applied alongside the surface of tip.

The von Mises stress or equivalent von Mises stress, was used to predict the yielding of the microcantilever. The tensile or fracture strength of PDMS is 2.24 MPa [47], the estimated maximum von Mises stress is found to be 2669.2 Pa, thus 0.0026692 MPa. The low von Mises predicted values indicate a safe structure. The microcantilever bends downwards and thus the maximum deflection occurs at the very end point of the tip. Due to the downward bending of the tip, the maximum von Mises stress, appears on the opposite direction (Figure 7.29). In (Figure 7.30) the deflection and von Mises stress curves are presented.

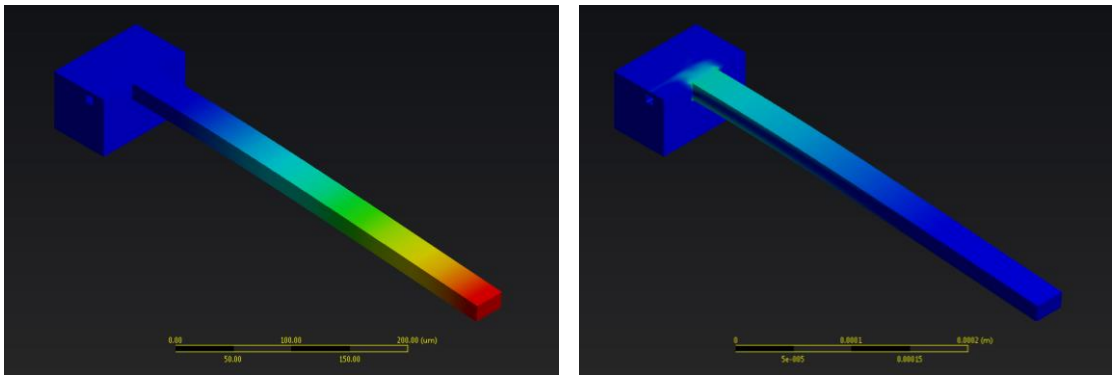

Figure 7.29 (Left) The Deflection and (Right) the von Mises stress 3D contour images.

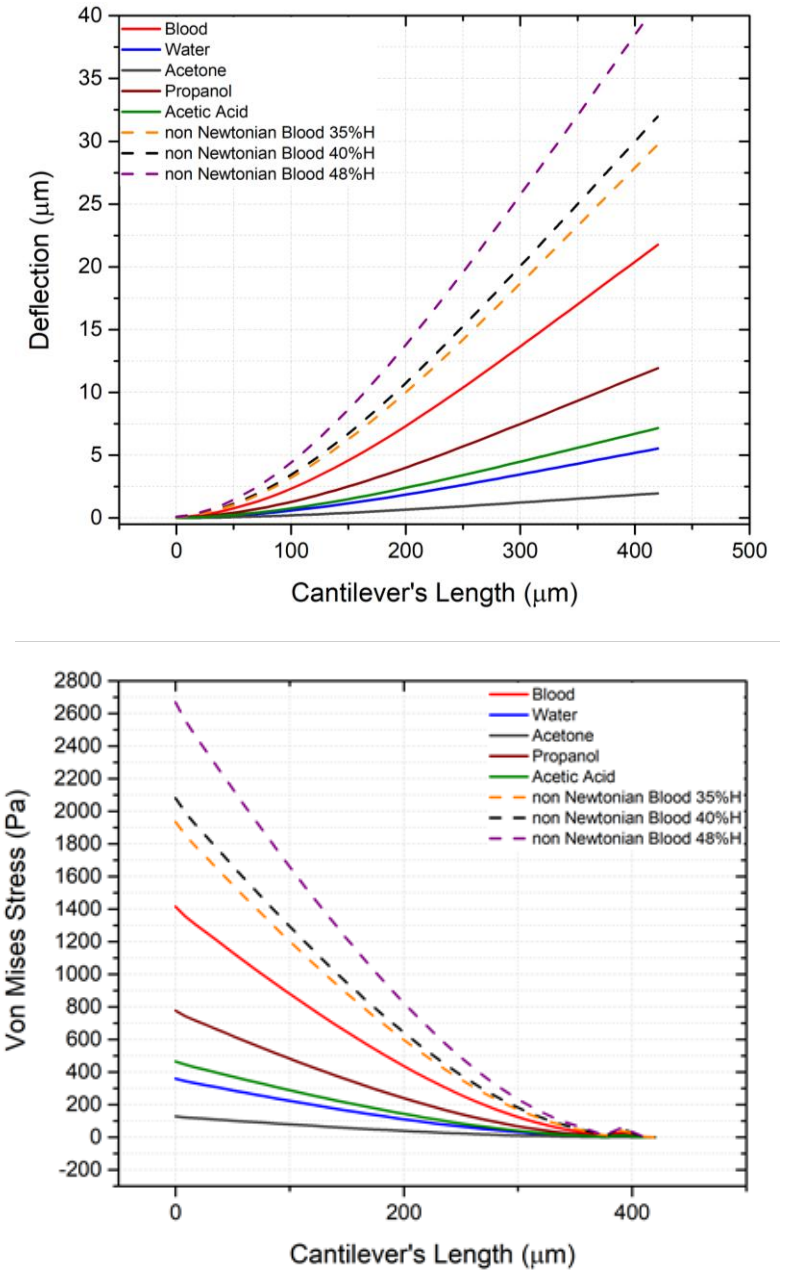

Figure 7.30 (Top) The Deflection and (Bottom) the von Mises stress curves.

CHAPTER 8. DISCUSSION, RESULTS & FUTURE WORK

DISCUSSION

A suspended microcantilever is a mechanical biosensor with a cavity that creates a microchannel. A fluid can flow into this microfluidic channel and the microcantilever's tip can bend downwards. The sensitivity of the microcantilever depends on the deflection of the tip. In this work, two biosensor types were designed and thus two microfluidic cases were taken into account.

Newtonian and Non-Newtonian fluids were tested. For each fluid domain, the Reynolds' Number, the Entrance Length, the Velocity Profile, the Pressure Drop alongside the microchannel and the Pressure drop versus the Dynamic Viscosity were calculated.

For the biosensor simulations, the pressure loads from the CFD simulations were transferred into the Mechanical analysis and a comparison between the one and the two way FSI was performed. For time and computational memory gaining, the FSI simulations performed using the one way approximation. The biosensor B1 was found to be the most sensitive. Furthermore, the materials tested for the fabrication of the biosensor, were PDMS and PMMA. The simulations showed that the PDMS was the best option. In addition, three different B1 biosensor types were designed with different tip lengths. The sensitivity of the biosensor depends on the length of the tip. However, the biosensor with the 420 μm was preferred for time and computational memory purposes. Moreover, in order to prove that the fluid velocity changes the sensitivity of the biosensor, three different velocity values were tested. After the aforementioned simulations, the designed biosensor was used to predict the deflection of the cantilever using a Newtonian and Non-Newtonian fluid. The Dynamic viscosity of a fluid due to the Cantilevers deflection, can also be predicted.

Last but not least, the deflection and the von Mises stress were plotted. The deflection and the von Mises stress contours were presented and a comparison between the tensile strength and the von Mises stress was performed.

RESULTS

In this study, an innovated FEM analysis for a 3D suspended microfluidics took place. The innovation of the study lies on the use of very small square cross section microfluidics channels (<10μm), very thin microcantilever's tip and on the complete study of the cantilever's deflection, using different fluids with different dynamic viscosities. Furthermore, the linear relationship between the length of the cantilever's tip, the dynamic viscosity, the fluid velocity and the microcantilever's deflection for both Newtonian and Non-Newtonian fluids were presented. While the majority of the studies are dealing with Newtonian fluids, in this work, by applying the Bird Carreau model, the blood is simulated as a Non-Newtonian fluid. Using this setup and a low inlet velocity (0.1 or 1 mm/s) a sensitive biosensor is introduced.

The proposed biosensor, B1, provides higher sensitivity in comparison to previous works. Packirisamy et al. 2018 [11] using a similar biosensor geometry as the B2, calculated the microcantilever's tip deflection versus the Dynamic viscosity. They designed a microcantilever with length, width and thickness of 6000x1000x600 μm, respectively, with a 2D suspended microfluidics channel of 200x100μm and applied a constant inlet velocity of 30 mm/s. Figure 8.1 shows the difference between our results, (where the initial fluid flow is 1 mm/s) and the work of Packirisamy et al [11].

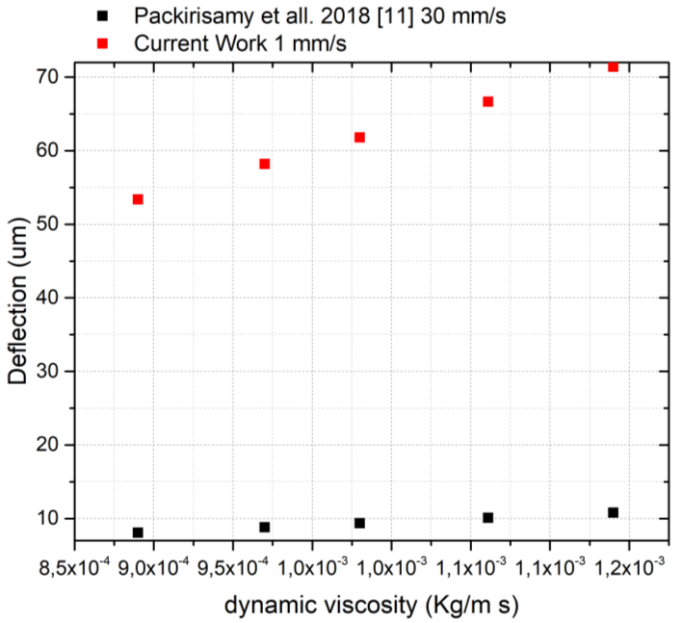

Figure 8.1 A comparison study between the current work and Packirisamy et al [11].

The current proposed biosensor shows promising results since it predicts with high accuracy the microcantilever's tip deflection for both Newtonian and Non-Newtonian fluids and their viscosities. Using this biosensor, one can employ either quantitative or qualitative measurements to predict if a fluid is classified as Newtonian or Non- Newtonian. Furthermore, it offers high sensitivity and accuracy, while its small size is crucial for LoC and PoC devices.

FUTURE WORK

In this work, a suspended microcantilever biosensor was studied intensively and shows promising results. As future work, the biosensor could be used to determine biomarkers, by measuring the deflection of the tip. It can measure cells' weight and it could function as a quick hematocrit analyzer in a PoC device using a piezoelectric element on the surface of the tip.

References

[1] Sader, J. E., Burg, T. P., & Manalis, S. R. (2010). Energy dissipation in microfluidic beam resonators. Journal of Fluid Mechanics, 650, 215-250.

[2] Burg, T. P., Godin, M., Knudsen, S. M., Shen, W., Carlson, G., Foster, J. S., ... & Manalis, S. R. (2007). Weighing of biomolecules, single cells and single nanoparticles in fluid. nature, 446(7139), 1066.

[3] Boisen, A., Dohn, S., Keller, S. S., Schmid, S., & Tenje, M. (2011). Cantilever-like micromechanical sensors. Reports on Progress in Physics, 74(3), 036101.

[4] Faegh, S., Jalili, N., & Sridhar, S. (2013). A self-sensing piezoelectric microcantilever biosensor for detection of ultrasmall adsorbed masses: Theory and experiments. Sensors, 13(5), 6089-6108.

[5] Faegh, S., Jalili, N., Yavuzcetin, O., Nagesha, D., Kumar, R., & Sridhar, S. (2013). A cost-effective self-sensing biosensor for detection of biological species at ultralow concentrations. Journal of Applied Physics, 113(22), 224905.

[6] Nezhad, A. S., Ghanbari, M., Agudelo, C. G., Packirisamy, M., Bhat, R. B., & Geitmann, A. (2013). PDMS microcantilever-based flow sensor integration for lab-on-a-chip. IEEE Sensors journal, 13(2), 601-609.

[7] Zhang, W. M., Yan, H., Jiang, H. M., Hu, K. M., Peng, Z. K., & Meng, G. (2016). Dynamics of suspended microchannel resonators conveying opposite internal fluid flow: Stability, frequency shift and energy dissipation. Journal of Sound and Vibration, 368, 103-120.

[8] Marzban, M., Packirisamy, M., & Dargahi, J. (2017). 3D Suspended Polymeric Microfluidics (SPMF3) with Flow Orthogonal to Bending (FOB) for Fluid Analysis through Kinematic Viscosity. Applied Sciences, 7(10), 1048.

[9] Zakeri, Manizhe, and Seyed Mahmoud Seyedi Sahebari. "Modeling and simulation of a suspended microchannel resonator nano-sensor." Microsystem Technologies (2017): 1-14.

[10] Lee, C. Y., Tsai, C. H., Chen, L. W., Fu, L. M., & Chen, Y. C. (2006). Elastic–plastic modeling of heat-treated bimorph micro-cantilevers. Microsystem Technologies, 12(10-11), 979-986.

[11] Marzban, M., Packirisamy, M., & Dargahi, J. (2018). Parametric study on fluid structure interaction of a 3D suspended polymeric microfluidics (SPMF 3). Microsystem Technologies, 1-11.

[12] Turner, A., Karube, I., & Wilson, G. S. (1987). Biosensors: fundamentals and applications. Oxford university press.

[13] LOWE, C. R., & GOLDFINCH, M. J. (1983). Novel electrochemical sensors for clinical analysis.

[14] Clark Jr, L. C. (1956). Monitor and control of blood and tissue oxygen tensions. ASAIO Journal, 2(1), 41-48.

[15] Meng, E. (2011). Biomedical microsystems. CRC Press.

[16] Bhalla, N., Jolly, P., Formisano, N., & Estrela, P. (2016). Introduction to biosensors. Essays in biochemistry, 60(1), 1-8.

[17] Saitakis, M., & Gizeli, E. (2012). Acoustic sensors as a biophysical tool for probing cell attachment and cell/surface interactions. Cellular and Molecular Life Sciences, 69(3), 357-371.

[18] White, R. M., & Voltmer, F. W. (1965). Direct piezoelectric coupling to surface elastic waves. Applied physics letters, 7(12), 314-316.

[19] Länge, K., Rapp, B. E., & Rapp, M. (2008). Surface acoustic wave biosensors: a review. Analytical and bioanalytical chemistry, 391(5), 1509-1519.

[20] Cullen, D. C., Karube, I., Lowe, C. R., & Weetall, H. H. (2007). Handbook of biosensors and biochips (Vol. 1500, No. 1). R. S. Marks (Ed.). Chichester, UK:: John Wiley & Sons.

[21] Jung, L. S., Nelson, K. E., Campbell, C. T., Stayton, P. S., Yee, S. S., Pérez-Luna, V., & López, G. P. (1999). Surface plasmon resonance measurement of binding and dissociation of wild-type and mutant streptavidin on mixed biotin-containing alkylthiolate monolayers. Sensors and Actuators B: Chemical, 54(1-2), 137-144.

[22] Baraket, A., Lee, M., Zine, N., Yaakoubi, N., Bausells, J., & Errachid, A. (2016). A flexible electrochemical micro lab-on-chip: application to the detection of interleukin-10. Microchimica Acta, 183(7), 2155-2162.

[23] Christodoulides, N., Mohanty, S., Miller, C. S., Langub, M. C., Floriano, P. N., Dharshan, P., ... & Fox, P. C. (2005). Application of microchip assay system for the measurement of C-reactive protein in human saliva. Lab on a Chip, 5(3), 261-269.

[24] Lee, W. B., Chen, Y. H., Lin, H. I., Shiesh, S. C., & Lee, G. B. (2011). An integrated microfluidic system for fast, automatic detection of C-reactive protein. Sensors and Actuators B: Chemical, 157(2), 710-721.

[25] Salvo, P., Calisi, N., Melai, B., Cortigiani, B., Mannini, M., Caneschi, A., ... & Scataglini, I. (2017). Temperature and pH sensors based on graphenic materials. Biosensors and Bioelectronics, 91, 870-877.

[26] Callister, W. D., & Rethwisch, D. G. (2011). Materials science and engineering (Vol. 5, pp. 344-348). NY: John Wiley & Sons.

[27] Rosengren, Å. (2004). Cell-protein-material interactions on bioceramics and model surfaces (Doctoral dissertation, Acta Universitatis Upsaliensis).

[28] Madou, M. J. (2002). Fundamentals of microfabrication: the science of miniaturization. CRC press.

[29] Folch, A. (2016). Introduction to bioMEMS. CRC Press.

[30] Von Philipsborn, A. C., Lang, S., Bernard, A., Loeschinger, J., David, C., Lehnert, D.,... & Bonhoeffer, F. (2006). Microcontact printing of axon guidance molecules for generation of graded patterns. Nature protocols, 1(3), 1322.

[31] Barbara Lopez and Dr. Matthias Pleil, SCME-NM.ORG, Southwest Center for Microsystems Education, "http://scme-nm.org/index.php?option=com_docman&view=docman&Itemid=226"

[32] Meng, E. (2011). Biomedical microsystems. CRC Press.

[33] Accoto, C., Qualtieri, A., Pisanello, F., Ricciardi, C., Pirri, C. F., De Vittorio, M., & Rizzi, F. (2015). Two-photon polymerization lithography and laser doppler vibrometry of a SU-8-based suspended microchannel resonator. Journal of Microelectromechanical Systems, 24(4), 1038-1042.

[34] Sugioka, K., Xu, J., Wu, D., Hanada, Y., Wang, Z., Cheng, Y., & Midorikawa, K. (2014). Femtosecond laser 3D micromachining: a powerful tool for the fabrication of microfluidic, optofluidic, and electrofluidic devices based on glass. Lab on a Chip, 14(18), 3447-3458.

[35] Haider, R., Marmiroli, B., Gavalas, I., Wolf, M., Matteucci, M., Taboryski, R., ... & Amenitsch, H. (2018). Laser ablation and injection moulding as techniques for producing micro channels compatible with Small Angle X-Ray Scattering. Microelectronic Engineering, 195, 7-12.

[36] Albrecht, T. R., Akamine, S., Carver, T. E., & Quate, C. F. (1990). Microfabrication of cantilever styli for the atomic force microscope. Journal of Vacuum Science & Technology A: Vacuum, Surfaces, and Films, 8(4), 3386-3396.

[37] Wolter, O., Bayer, T., & Greschner, J. (1991). Micromachined silicon sensors for scanning force microscopy. Journal of Vacuum Science & Technology B: Microelectronics and Nanometer Structures Processing, Measurement, and Phenomena, 9(2), 1353-1357.

[38] Zhang, G., Li, C., Wu, S., & Zhang, Q. (2018). Label-free aptamer-based detection of microcystin-LR using a microcantilever array biosensor. Sensors and Actuators B: Chemical, 260, 42-47.

[39] Schön, P. (2016). Imaging and force probing RNA by atomic force microscopy. Methods, 103, 25-33.

[40] Berger, R., Delamarche, E., Lang, H. P., Gerber, C., Gimzewski, J. K., Meyer, E., & Güntherodt, H. J. (1997). Surface stress in the self-assembly of alkanethiols on gold. Science, 276(5321), 2021-2024.

[41] Lang, H. P., Berger, R., Battiston, F., Ramseyer, J. P., Meyer, E., Andreoli, C., ... & Scandella, L. (1998). A chemical sensor based on a micromechanical cantilever array for the identification of gases and vapors. Applied Physics A: Materials Science & Processing, 66, S61-S64.

[42] Fritz, J., Baller, M. K., Lang, H. P., Rothuizen, H., Vettiger, P., Meyer, E., ... & Gimzewski, J. K. (2000). Translating biomolecular recognition into nanomechanics. Science, 288(5464), 316-318.

[43] Boisen, A., Thaysen, J., Jensenius, H., & Hansen, O. (2000). Environmental sensors based on micromachined cantilevers with integrated read-out. Ultramicroscopy, 82(1-4), 11-16.

[44] Wu, G., Datar, R. H., Hansen, K. M., Thundat, T., Cote, R. J., & Majumdar, A. (2001). Bioassay of prostate-specific antigen (PSA) using microcantilevers. Nature biotechnology, 19(9), 856.

[45] Berger, R., Gerber, C., Gimzewski, J. K., Meyer, E., & Güntherodt, H. J. (1996). Thermal analysis using a micromechanical calorimeter. Applied Physics Letters, 69(1), 40-42.

[46] Feng, X. L., He, R., Yang, P., & Roukes, M. L. (2007). Very high frequency silicon nanowire electromechanical resonators. Nano Letters, 7(7), 1953-1959.

[47] Ekinci, K. L., Huang, X. M. H., & Roukes, M. L. (2004). Ultrasensitive nanoelectromechanical mass detection. Applied Physics Letters, 84(22), 4469-4471.

[48] Yang, Y. T., Callegari, C., Feng, X. L., Ekinci, K. L., & Roukes, M. L. (2006). Zeptogram-scale nanomechanical mass sensing. Nano letters, 6(4), 583-586.

[49] Young, W. C., & Budnyas, R. G. (2017). Roark's formulas for stress and strain. McGraw-Hill.

[50]Cleland, A. N. (2003). Foundations of Nanomechanics: From Solid-State Theory to Device Applications (Advanced Texts in Physics).

[51] Timoshenko, S. P., & Woinowsky-Krieger, S. (1959). Theory of plates and shells. McGraw-hill.

[52] Schmid, S. (2009). Electrostatically actuated all-polymer microbeam resonators: Characterization and application (Vol. 6). ETH Zurich.

[53] Dohn, S., Sandberg, R., Svendsen, W., & Boisen, A. (2005). Enhanced functionality of cantilever based mass sensors using higher modes. Applied Physics Letters, 86(23), 233501.

[54] Lee, D., Kim, S., Jung, N., Thundat, T., & Jeon, S. (2009). Effects of gold patterning on the bending profile and frequency response of a microcantilever. Journal of Applied Physics, 106(2), 024310.

[55] Dohn, S. A., Svendsen, W., Boisen, A., & Hansen, O. (2007). Mass and position determination of attached particles on cantilever based mass sensors. Review of Scientific Instruments, 78(10), 103303.

[56] Dohn, S., Schmid, S., Amiot, F., & Boisen, A. (2010). Position and mass determination of multiple particles using cantilever based mass sensors. Applied Physics Letters, 97(4), 044103.

[57] Stoney, G. G. (1909). The tension of metallic films deposited by electrolysis. Proc. R. Soc. Lond. A, 82(553), 172-175.

[58] Jaccodine, R. J., & Schlegel, W. A. (1966). Measurement of strains at Si-SiO2 interface. Journal of Applied Physics, 37(6), 2429-2434.

[59] Godin, M., Tabard-Cossa, V., Grütter, P., & Williams, P. (2001). Quantitative surface stress measurements using a microcantilever. Applied Physics Letters, 79(4), 551-553.

[60] Burg, T. P., & Manalis, S. R. (2003). Suspended microchannel resonators for biomolecular detection. Applied Physics Letters, 83(13), 2698-2700.

[61] Burg, T. P., Godin, M., Knudsen, S. M., Shen, W., Carlson, G., Foster, J. S., ... & Manalis, S. R. (2007). Weighing of biomolecules, single cells and single nanoparticles in fluid. nature, 446(7139), 1066.

[62] Lee, J., Chunara, R., Shen, W., Payer, K., Babcock, K., Burg, T. P., & Manalis, S. R. (2011). Sspended microchannel resonators with piezoresistive sensors. Lab on a Chip, 11(4), 645-651.

[63] Patel, A. R., Lau, D., & Liu, J. (2012). Quantification and characterization of micrometer and submicrometer subvisible particles in protein therapeutics by use of a suspended microchannel resonator. Analytical chemistry, 84(15), 6833-6840.

[64] Lee, I., Park, K., & Lee, J. (2012). Note: Precision viscosity measurement using suspended microchannel resonators. Review of Scientific Instruments, 83(11), 116106.

[65] Olcum, S., Cermak, N., Wasserman, S. C., & Manalis, S. R. (2015). High-speed multiple-mode mass-sensing resolves dynamic nanoscale mass distributions. Nature communications, 6, 7070.

[66] Hrennikoff, Alexander. "Solution of problems of elasticity by the framework method." Journal of applied mechanics 8.4 (1941): 169-175.

*[67] Courant, R. (1943). "Variational methods for the solution of problems of equilibrium and vibrations". Bulletin of the American Mathematical Society. **49**: 1–23*

[68] Kardestuncer, H. "Dedication to Professor John H. Argyris: A man who unifies engineering and mathematics with elegance." North-Holland Mathematics Studies. Vol. 94. North-Holland, 1984. v-vii.

[69] Clement Kleinstreuer, "Microfluidics and Nanofluidics, Theory and Seleceted Applications", WILEY, 2014

[70] P.L. George, "Automatic Mesh Generation, Application to Finite Element Methods", WILEY, 1991

[71] Richter, T. (2010). Numerical methods for fluid-structure interaction problems. Institute for Applied Mathematics, University of Heidelberg, Germany.

[72] Hou, G., Wang, J., & Layton, A. (2012). Numerical methods for fluid-structure interaction—a review. Communications in Computational Physics, 12(2), 337-377.

[73] Belostosky, A. M., Akimov, P. A., Kaytukov, T. B., Afanasyeva, I. N., Usmanov, A. R., Scherbina, S. V., & Vershinin, V. V. (2014). About finite element analysis of fluid–structure interaction problems. Procedia Engineering, 91, 37-42.

[74] Rugonyi, S., & Bathe, K. J. (2001). On finite element analysis of fluid flows fully coupled with structural interactions. CMES- Computer Modeling in Engineering and Sciences, 2(2), 195-212.